
Validation of ocean mass variability derived from the Gravity Recovery and Climate Experiment

Studies utilizing *in-situ* observations and results from a
Finite Element Sea ice – Ocean Model

Dissertation zur Erlangung des Doktorgrades der
Naturwissenschaften
- Dr. rer. nat. -

vorgelegt von Carmen Böning
am Fachbereich Physik der



25. Juni 2009

1. Gutachter: Prof. Dr. D. Olbers
2. Gutachter: Prof. Dr. P. Lemke

Abstract

The Gravity Recovery and Climate Experiment (GRACE) provides estimates of the Earth's time-variable and static gravity field with an unprecedented accuracy. As fluctuations of the gravity field on sub-annual time scales are mainly induced by mass redistribution on the Earth's surface, GRACE is potentially able to monitor oceanic mass variability and redistribution. Current gravity data products, however, suffer from aliasing effects due to insufficient accuracy of background models. This study compares different filter mechanisms and develops a new filtering approach which uses information on ocean circulation patterns derived from model simulations with the Finite Element Sea – Ice Ocean Model (FESOM).

To obtain a realistic representation of the ocean mass budget on interannual time scales in the FESOM model, the computation of sea surface height is extended in order to consider the effect of surface freshwater fluxes and internal mixing. The river runoff forcing is modified to balance the net evaporation on long time scales. For validation, we utilize *in-situ* ocean bottom pressure (OBP) data from a global bottom pressure data base. For the correction of tides, variations derived from the tidal model (FES2004), also used as a background model in the GRACE data processing, are subtracted from the *in-situ* data.

In general, the validation of GRACE-derived anomalies against *in-situ* time series indicates a good agreement between the two data sets. Especially, for the high latitude arrays GRACE captures a considerable part of the observed oceanic variability. Largest errors in the GRACE data are found in the tropical Atlantic, where the GRACE-derived OBP data from all data centers feature spurious variability which probably goes back to tidal aliasing and/or the large hydrological cycle over the Orinoco/Amazon river basin.

Filtering the GRACE data with the new pattern-based approach improves the correlations between GRACE and *in-situ* OBP anomalies compared to conventional isotropic Gauss filtering. Focussing on the ocean domain, the filter reduces land leakage effects and introduces valuable information on the ocean circulation to the GRACE data, which helps to reduce errors and to identify geophysical signals in the gravity field solutions.

As a first application, the improved GRACE data sets are utilized to study the relation between oceanic transport variability and cross-flow gradients of OBP anomalies. Maps of correlations between the Southern Annular Mode (which is the dominant mode of atmospheric variability in the Southern Ocean) and GRACE OBP anomalies reveal a circumpolar band of highly negative correlation around Antarctica closely following f/H contours. Although this spatial structure is already found for data filtered with an isotropic Gauss filter, correlations are further enhanced when using the new filter approach. Based on these results, this study supports previous findings indicating that SAM affects ACC transport variability at least on a month-to-month time scale.

Contents

1	Introduction	9
2	Model Description	13
2.1	The Finite Element Method	13
2.2	The Finite Element Ocean Model (FEOM)	15
2.2.1	Model basics	15
2.2.2	Model equations	15
2.2.3	Parameterization of subgrid-scale processes	17
2.3	Finite Element Sea-Ice Model	18
2.3.1	Model basics	18
2.3.2	Model equations	19
2.4	Initialisation and atmospheric forcing	21
2.5	Configuration	21
3	Ocean mass budget	23
3.1	Ocean bottom pressure	23
3.2	Sea surface height variability	24
3.2.1	Boussinesq approximation	26
3.2.2	Implementation of sea level	27
3.3	Global surface freshwater flux budget	29
3.3.1	Net precipitation and runoff	30
3.3.2	Surface freshwater budget in FESOM	30
4	<i>In-situ</i> OBP and FESOM Validation	35
4.1	The Ocean Bottom Pressure Database	35
4.2	Tidal variability	37
4.2.1	Correction for tides	41
4.2.2	Summary	46
4.3	Validation of FESOM	49
4.3.1	Conclusions	57

5	Validation of GRACE OBP	59
5.1	GRACE gravity field solutions	60
5.1.1	Data collection and processing	60
5.1.2	GRACE products	61
5.1.3	Deriving OBP from GRACE solutions	62
5.1.4	Correction for geocenter motion	63
5.1.5	Detection of OBP signals in GRACE solutions	65
5.2	A new filter algorithm for GRACE data	67
5.2.1	Coherence patterns of OBP variability	67
5.2.2	Improvement of GRACE solutions due to pattern filtering	69
5.3	De-striped GRACE solutions	73
5.4	Global and regional validation	76
5.4.1	Regional validation	76
5.4.2	Basin and global scale	80
5.5	Conclusions	85
6	Ocean mass variability	87
6.1	OBP-estimated transport variability	89
6.2	Estimates of ACC transport variability	90
6.2.1	Regional comparison	92
6.2.2	Transport variability in the ACC array	94
6.3	SAM and ACC transport fluctuations	97
6.3.1	SAM index, sea level pressure patterns and wind anomalies	97
6.3.2	Connection between SAM and ACC transport	98
6.4	Discussion	104
7	Conclusions and Outlook	107
A	The <i>in-situ</i> OBP data base	115
B	Auxiliary material	117
	List of Acronyms	123
	Acknowledgments	139

Chapter 1

Introduction

Observations of changes in sea surface elevation and oceanic currents are traditionally obtained from devices installed in coastal areas (e.g. tide gauges) or moored on the sea floor (e.g. moorings equipped with current meters). However, evaluating global sea level changes and ocean mass redistribution on the basis of these data is obviously impaired by the limited number of *in-situ* observational sites.

A new approach emerged in the late 20th century with the onset of satellite based remote sensing. First satellite observations of sea surface height, i.e. the deviation of the sea surface from the Earth's reference ellipsoid, have been conducted in the 1970s (Geos C and Seasat) using radar altimetry. This technique allows for a global view on the oceanic sea surface. Large scale phenomena like El Niño which is characterized by events of unusually warm waters that form along the coast of Equador and Peru are better understood using results from satellite-based oceanic observations of the sea surface.

Today, satellites are used for the investigation of many oceanographic and oceanography-related topics. When it comes to sea level rise and the change of ocean currents, new questions arise. Satellite altimetry gives an estimate of the total amount and the regional distribution of the increase in sea level. Currently, the total global average sea level rise is estimated to be 3.1 mm yr^{-1} (IPCC (2007)). But how large are the contributions from steric and eustatic sea level change? Does the warming or the mass gain due to ice sheet melting affect the sea level most? How do the water mass properties and transport develop in time? How can we determine the inter-basin exchange of water masses?

Gravity missions, which provide estimates of the Earth's static and time-variable gravity field, can help to answer these questions. The Gravity Recovery And Climate Experiment (GRACE), launched in 2002, is the first mission

utilizing two satellites following each other on the same orbital track. A microwave based interconnection between the two Low Earth Orbiters (LEOs) provides a measurement of the separation distance. The distance between the satellites increases when they approach a positive mass anomaly then decreases when both satellites are located above the anomaly and then again increases when they move away. Using this information and precise orbit determination GRACE provides estimates of the time-variable gravity field.

Variations in the gravity field on a monthly time scale as provided by GRACE are assumed to originate mainly from hydrological signals while fluctuations in the Earth's interior appear on significantly longer time scales. Thus, the major contributions to gravity anomalies on sub-annual to annual time scales are found to be the large hydrological cycles over river basins (Schmidt et al. (2006), Nooner et al. (2008)). Also snow accumulation (Frapart et al. (2006)) and ice sheet melting (Velicogna and Wahr (2006)) at high latitudes leads to large signals which are measured by GRACE.

Over the ocean signals are much smaller since any flux of water into the ocean is quickly redistributed. Therefore, the variations are much more difficult to detect in the satellite data.

Temporal changes in the geopotential over the ocean are directly related to fluctuations in atmosphere and ocean mass distribution, as modulations in the gravity field on short time scales are mainly produced by near-surface mass redistributions. Thus, the gravity field anomalies over the ocean derived from GRACE solutions can be interpreted as anomalies of ocean bottom pressure (OBP), i.e. the changes in pressure exerted by the atmosphere and ocean mass on the ocean floor.

Forming novel data sets, the GRACE gravity field solutions require a thorough validation. Especially, validation of OBP data derived from GRACE gravity fields constitutes a challenging task: the *in-situ* data base of OBP is sparse. Ocean models, on the other hand, may reproduce OBP variability to some extent, but are bound to contain errors. First validation studies against *in-situ* data have been performed using data in the tropical Atlantic (Kanzow et al. (2005)) and in the Kerguelen region in the Southern Indian Ocean (Rietbroek et al. (2006)). The results from the tropical Atlantic indicate a large disagreement between GRACE-derived OBP and *in-situ* data, whereas Rietbroek et al. (2006) found a rather good agreement between GRACE-derived and *in-situ* OBP anomalies.

On basin and global scales, early GRACE data releases have been compared to results from ocean models. Ponte et al. (2007) found a good agreement between ECCO (Estimating the Circulation and Climate of the Ocean) ocean model simulations and the global annual cycle found in the GRACE data. A study of Zlotnicki et al. (2006) focusses on the validation of GRACE

data from the period 2002-2005 in the Southern Ocean and already detects relations between large scale GRACE-derived OBP anomalies, ECCO and POCM (Parallel Ocean Climate Model) simulations, and wind observations as provided by the QuikSCAT satellite mission at least for semi-annual and annual periods.

Thus, the problem of validation of GRACE solutions is far from being complete. The main goal of this thesis is to contribute to this task by a systematic study exploiting new GRACE solutions, newly available OBP data and ocean modeling.

Most of the previous studies focus on regional comparisons due to the given *in-situ* data base, or rely on model results only. By contrast, this thesis comprises a global validation of GRACE data over the ocean based on the newest data releases from the three official processing centers GFZ (Geoforschungszentrum Potsdam), CSR (Center for Space Research), and JPL (Jet Propulsion Laboratory) against *in-situ* OBP data as well as results from ocean model simulations.

At first, in Chapter 2, the Finite Element Sea ice – Ocean Model (FESOM; Timmermann et al. (2009)), utilized in this study, is introduced. We discuss the equations solved by the ocean and sea-ice components and outline approximations and parametrizations that are used. In addition to this, a short introduction into the principles of finite element modeling is provided.

Chapter 3 then focusses on the computation of OBP in the FESOM model. Common simplifications of the model equations, like the Boussinesq approximation, and the surface forcing which is not designed to close the mass budget, result in an unrealistic description of ocean mass and OBP variability. Therefore, a correction of the surface forcing and a compensation of the Boussinesq approximation, both aiming at a realistic description of the mass budget, were implemented in the model. We discuss the implementation of these corrections and illustrate the influence on the simulated global ocean mass budget.

Chapter 4 constitutes a detailed description of the *in-situ* data used for this study. Measurements from various bottom pressure recorder arrays have been collected in a global database at the Alfred Wegener Institute for Polar and Marine Research (Macrander et al. (2009)). In order to remove tidal variability from the *in-situ* data, we utilize a state-of-the-art tidal model, which was also used for the de-aliasing of the GRACE gravity fields. Thus, consistency with the GRACE data is ensured when using this model. However, model induced errors, especially in the short-period, like semi-diurnal and diurnal, tides, are found to affect the GRACE solutions (Seo et al. (2008)). To evaluate the extent of the influence of potentially erroneous corrections on the GRACE retrievals, we compare time series of *in-situ* OBP corrected with

empirically determined and simulated tides in a bottom pressure recorder (BPR) array in the South Atlantic. The corrected *in-situ* data are used to assess the ability of the modified FESOM to capture real oceanic variability. In addition to a general global validation, we focussed on two exemplary BPR arrays in order to evaluate daily and monthly FESOM OBP variability compared to the observed *in-situ* OBP variability.

Chapter 5 comprises a comprehensive validation study of the GRACE data over the ocean. First, the GRACE mission, data acquisition and processing are described in general. We discuss common issues in the general geophysical interpretation of the current GRACE data products and suggested solutions to overcome these issues by additional post-processing. A decent filtering has to be applied to the GRACE gravity solutions in order to reduce errors. One additional strategy for post-processing and deriving geophysical signals from GRACE data over the ocean is developed in the frame of this thesis and presented in this chapter. The post-processed GRACE data derived from the recent GRACE Releases of the three official processing centers are then validated against the *in-situ* and simulated OBP.

In Chapter 6 we use OBP derived from GRACE, *in-situ* and FESOM to investigate the relationship between OBP and the circulation in the Southern Ocean. On the base of recent studies on the transport and transport variability of the Antarctic Circumpolar Current (ACC) (Hughes et al. (2003), Meredith et al. (2004), Cunningham et al. (2003), Olbers et al. (2004)), we discuss the ability of GRACE to observe the ACC transport variability. Results from FESOM and *in-situ* OBP data in the ACC are used to assess the quality of GRACE data in this respect. In particular, we focus on the relation between the atmospheric mode of variability in the Southern Hemisphere, the Southern Annular Mode (SAM), and the oceanic transport variability. We use model simulations to relate OBP variability to variations of SAM and compare the results to connections found in the GRACE data.

A discussion of results and an outlook to future work in Chapter 7 closes the thesis.

Chapter 2

Model Description

The Finite-Element Sea ice–Ocean Model (FESOM; Timmermann et al. (2009)) consists of the hydrostatic primitive-equation Finite-Element Ocean Model (FEOM), which has grown up from an earlier version described by Danilov et al. (2004), and a newly developed finite-element sea-ice model (Danilov and Yakovlev (2003)).

2.1 The Finite Element Method

The finite-element method (FEM) offers an approach enabling the usage of unstructured grids for ocean modeling purposes. In general, FEM is used to solve systems of partial differential equations on complex geometries. The idea is to discretize the spatial domain and define basis functions giving a representation of the prognostic variables on the grid. Common discretizations are triangles in a 2D and tetrahedra or prisms in a 3D domain. Using these triangular based structures provides suitable representation of features on various spatial scales.

The idea of using unstructured grids for modeling ocean dynamics is attractive due to the high complexity of the ocean geometry. Fine topographic features like narrow straits, steep continental slopes, islands, etc. are of crucial importance and may control the circulation on large spatial scales while they can hardly be resolved with an affordable homogeneous spatial resolution as frequently used by the Finite Difference Method (FDM).

The computational mesh used for FESOM is composed of tetrahedra. It is based on an unstructured surface triangular grid. Vertical discretization for this model version is on z-levels with grid nodes aligned underneath each surface grid node. In order to avoid a stepwise bottom and to approximate bathymetry in a smooth way with realistic depths, nodes of bottom elements

are allowed to deviate from z-levels.

The model uses linear basis functions for horizontal velocity \vec{u} , tracer variables, and surface elevation, leading to a continuous linear representation of model variables (so-called P_1 - P_1 discretization, with P standing for 'polynomial', and the subscript for its order). Basis functions φ_j are equal to 1 at node j and linearly go to 0 at the neighboring nodes. They are zero outside the cluster of neighboring elements. Using these basis functions, any field a is expressed as $a = \sum a_j \varphi_j$, where a_j are the nodal values, located on the corners of the tetrahedra.

To illustrate the finite element method, consider the example of a typical differential equation the example of a twodimensional conservation equation for a scalar ψ , such as salt content or ice concentration:

$$\frac{\partial \psi}{\partial t} + \nabla \cdot (\psi \vec{u}) = S \quad (2.1)$$

with the velocity field \vec{u} and a source S .

Following the standard FE method, equation (2.1) is projected on an appropriate set of test functions \tilde{m} depending on the spatial discretization.

$$\int_{\Omega} \tilde{m} \left(\frac{\partial \psi}{\partial t} + \nabla \cdot (\psi \vec{u}) \right) d\Omega = \int_{\Omega} \tilde{m} S d\Omega \quad (2.2)$$

with Ω denoting the surface to be integrated over. Making use of partial integration, Green's formula and assuming that the boundary is impermeable we arrive at

$$\int_{\Omega} \left(\tilde{m} \frac{\partial \psi}{\partial t} - \nabla \tilde{m} \cdot \vec{u} \psi \right) d\Omega = \int_{\Omega} \tilde{m} S d\Omega. \quad (2.3)$$

The problem (2.3) (and (2.1)) has to be completed with initial conditions $\psi = \psi_0$ at $t = 0$ and, in the general case, by boundary conditions on the part of the boundary, where the velocity is directed inside the domain.

For discretization, the scalar field is expanded into the series

$$\psi = \sum_{j=1}^N \psi_j \varphi_j, \quad (2.4)$$

where N is the total number of (surface) nodes, $\psi_j(t)$ are the nodal values, and $\varphi_j(x, y)$ are the basis functions. Requiring \tilde{m} to be any of $\varphi_i(x, y)$, $1 \leq i \leq N$, we obtain the Galerkin system of equations for nodal values ψ_j

$$M_{ij} \frac{\partial \psi_j}{\partial t} + A_{ij} \psi_j = R_i, \quad (2.5)$$

where

$$M_{ij} = \int_{\Omega} \varphi_i \varphi_j d\Omega, \quad A_{ij} = \int_{\Omega} \nabla \varphi_i \vec{u} \varphi_j d\Omega, \quad R_i = \int_{\Omega} \varphi_i \varphi_j S_j d\Omega. \quad (2.6)$$

The mass matrix M_{ij} is not diagonal, but has a limited bandwidth (the number of entries is given by the number of neighbors). Although it is time-invariant, iterative solvers are required to invert it at every time step, simply because its inverse would not fit into computer memory.

Discretizing $\partial\psi_j/\partial t \approx (\psi_j^{n+1} - \psi_j^n)/\Delta t$, where n marks time steps and Δt is the time step duration, the matrix problem can be rewritten as

$$S_{ij} \psi_j^{n+1} = R_i^n + M_{ij} \psi_j^n / \Delta t. \quad (2.7)$$

The matrix

$$S_{ij} = M_{ij} / \Delta t + A_{ij} \quad (2.8)$$

is the stiffness matrix of the problem.

The solution of the given problem is then obtained by solving the linear system of equations (2.7), with ψ_j^0 be determined by the initial condition.

2.2 The Finite Element Ocean Model (FEOM)

2.2.1 Model basics

The Finite-Element Ocean Model (FEOM) is based on the work of Danilov et al. (2004), in which the model was introduced as a Finite-Element model of the North Atlantic (FENA). It is a hydrostatic ocean circulation model which solves the primitive equations in a spherical geometry.

2.2.2 Model equations

The dynamical part of the model solves the momentum evolution equation under the integral continuity constraint:

$$\frac{\partial \vec{u}}{\partial t} + f(\vec{k} \times \vec{u}) + g \nabla \eta - \nabla \cdot A_l \nabla \vec{u} - \frac{\partial}{\partial z} A_v \frac{\partial}{\partial z} \vec{u} = -\frac{1}{\rho_0} \nabla p - \vec{F}_u, \quad (2.9)$$

$$\frac{\partial \eta}{\partial t} + \nabla \cdot \int_{-H}^{\eta} \vec{u} dz = 0, \quad (2.10)$$

$$p = p_a + \int_z^0 g \rho dz, \quad (2.11)$$

where $(\vec{u}, w) \equiv (u, v, w)$ is the velocity vector, ρ_0, ρ are the mean sea water density and the deviations from that mean respectively, η is the sea surface elevation, p is the pressure anomaly computed from the level $z = 0$, p_a is the atmospheric pressure, f is the Coriolis parameter, A_l, A_v are the lateral and vertical viscosity coefficients, \vec{k} is the vertical unit vector, and g is the gravitational acceleration. A horizontal operator ∇ is implied. The term $\vec{F}_u = -(\vec{u}\nabla + w\partial_z)\vec{u}$ represents non-linear advection in the momentum equation. The computation of surface elevation will be modified for an improved implementation of the mass budget and will be described in chapter 3.

The equations are solved in a domain Ω limited by four physically different types of boundaries $\partial\Omega = \bigcup_{i=1}^4 \Gamma_i$, where $\Gamma_1 = \{z|z = 0\}$ stands for the ocean surface, $\Gamma_2 = \{z|z = -H(\lambda, \phi)\}$ is the bottom of the ocean, Γ_3 represents the lateral vertical rigid walls of the domain. Here λ, ϕ are the longitude and latitude respectively. The set of boundary conditions used with the dynamical part of the model includes the condition of momentum flux continuity at the ocean surface, the bottom-drag condition on the bottom, no-slip boundary conditions on the vertical walls and the open-boundary condition:

$$A_v \frac{\partial \vec{u}}{\partial z} = \vec{\tau}, \text{ on } \Gamma_1, \quad (2.12)$$

$$A_v \frac{\partial \vec{u}}{\partial z} + A_l((\nabla H) \cdot \nabla)\vec{u} = C_g \vec{u}|\vec{u}|, \text{ on } \Gamma_2, \quad (2.13)$$

$$\vec{u} = 0 \text{ on } \Gamma_3, \quad (2.14)$$

where $\vec{\tau}$ is the vector of tangent wind stresses, and $C_g = 0.0025$ the friction coefficient.

The vertical velocity is integrated from the ocean surface with the kinematic boundary condition:

$$w = \frac{\partial \eta}{\partial t} \text{ on } \Gamma_1. \quad (2.15)$$

It also obeys the second boundary condition at the bottom:

$$w = -\nabla H \cdot \vec{u} \text{ on } \Gamma_2. \quad (2.16)$$

These two boundary conditions are not independent; they are linked via eqn. (2.10).

Since we use the hydrostatic approximation, w is diagnosed from the continuity equation written in the Boussinesq approximation:

$$\frac{\partial w}{\partial z} = -\nabla \cdot \vec{u}. \quad (2.17)$$

In the thermodynamical part we solve the tracer evolution equations for the potential temperature Θ and the salinity S of sea water, and compute density via the equation of state:

$$\frac{\partial C}{\partial t} + \nabla \cdot (\vec{u}C) + \frac{\partial}{\partial z}(wC) - \nabla \cdot K_l \nabla C - \frac{\partial}{\partial z} K_v \frac{\partial}{\partial z} C = 0, \quad (2.18)$$

$$\rho = \rho(\Theta, S, p). \quad (2.19)$$

where C can be Θ or S or any passive tracer, and K_l and K_v are lateral and vertical diffusivities, respectively.

The tracers satisfy the following boundary conditions on the surface and solid boundaries:

$$K_v \frac{\partial C}{\partial z} = -q \text{ or } C = C_0 \text{ on } \Gamma_1, \quad \left(\nabla C, \frac{\partial C}{\partial z} \right) \cdot \vec{n}_3 = 0 \text{ on } \Gamma_2 \cup \Gamma_3, \quad (2.20)$$

where q and C_0 are the surface fluxes and surfaces values of Θ and S , \vec{n}_3 is the 3D unit vector normal to the respective surface. Equations (2.18) and (2.19) represent a basic implementation. The FESOM code also supports Redi (1982) rotated diffusivities and the Gent and McWilliams (1990) parameterization.

In contrast to the early version of the model described in Danilov et al. (2004) in FESOM the pressure projection method is used to solve momentum and continuity equations which results in a different numerical core and a greatly improved CPU efficiency. To enable the computation of *in-situ* density as a function of potential temperature Θ , the equation of state is used in the form that has been proposed by Jackett and McDougall (1995).

The finite element method is utilized to discretize the equations. The model is formulated on grids which are based on unstructured triangles at the surface but are vertically aligned and use tetrahedral elements in the volume. Pressure modes provoked by using a linear representation for the elevation and horizontal velocity are removed by the particular implementation of the pressure projection method. For the tracer equations, we use the stabilization described in Danilov et al. (2004).

2.2.3 Parameterization of subgrid-scale processes

Both, the lateral and vertical components of the viscous and diffusive terms in the equations of motion and conservation of heat and salt are calculated by using harmonical operators.

Lateral mixing. To parameterize the effects of sub-grid scale processes on the tracer distribution, we employ a tracer mixing along neutral density surfaces according to the rotational approach by Redi (1982). The Gent and McWilliams (1990) (GM) (see also Gent et al. (1995)) scheme provides the advective flux arising from an eddy-induced bolus velocity.

Lateral viscosity A_l^i and diffusivity K_l^i for both schemes are linear functions of the element area Δ^i

$$A_l^i = 10^{-5} s^{-1} \Delta^i, \quad (2.21)$$

$$K_l^i = 0.04 \cdot A_l^i \quad (2.22)$$

and thus adjust to a varying horizontal resolution. To avoid numerical instability in situations with very steep surfaces of neutral density, which occur, e.g., within the mixed layer, lateral diffusivity in the GM parameterization is tapered according to the scheme of Griffies (2004).

Vertical mixing. In the vertical direction, a modified version of the Pacanowski and Philander (1981) scheme ensures that vertical mixing of temperature and salinity is continuously increased for a weakening stratification. We use it with a maximum diffusivity of $0.01 \text{ m}^2/\text{s}$, which is also applied in case of a statically unstable stratification (i.e. negative Richardson number). To avoid unrealistically shallow mixed layers in summer, an additional horizontal diffusivity of $0.01 \text{ m}^2/\text{s}$ over a depth defined by the Monin-Obukhov-length is applied (Timmermann and Beckmann (2004)). For vertical mixing of momentum, a constant viscosity of $2 \cdot 10^{-3} \text{ m}^2/\text{s}$ is applied.

2.3 Finite Element Sea-Ice Model

2.3.1 Model basics

The FESOM sea-ice component is a dynamic-thermodynamic sea-ice model with the Parkinson and Washington (1979) thermodynamics and the Hunke and Dukowicz (1997) elastic-viscous-plastic (EVP) rheology. The model includes a prognostic snow layer (Owens and Lemke (1990)) accounting for the effect of snow-ice conversion due to flooding (Leppäranta (1983); Fischer (1995)). Heat storage in the ice and the snow is neglected, so that linear temperature profiles in both layers are assumed (so-called zero-layer approach of Semtner Jr. (1976)). The equations for sea-ice dynamics are discretized on

an unstructured triangular grid. The sea-ice grid is identical to the ocean surface grid.

2.3.2 Model equations

To describe the temporal evolution of the ice pack the model uses five prognostic variables:

- h , defined as the mean sea ice thickness i.e. the ice volume per unit area
- h_s , the mean snow thickness, i.e. the snow volume per unit area
- A , the dimensionless sea ice concentration
- $\vec{u} = (u, v)$, the ice (and snow) drift velocity

The dynamical part of the sea-ice model solves the velocity equation

$$m \left(\frac{\partial}{\partial t} + f(\vec{k} \times) \right) \vec{u} = A (\vec{\tau}_{ai} - c_{d,io} \rho_o (\vec{u} - \vec{u}_w) |\vec{u} - \vec{u}_w|) + \vec{F} - mg \nabla \eta. \quad (2.23)$$

Here m is the ice plus snow mass per unit area, $\vec{\tau}_{ai}$ is the wind stress, $c_{d,io}$ the ice-ocean drag coefficient, ρ_o the density of sea water; \vec{u}_w denotes the ocean surface velocity; η is the sea surface elevation, g the acceleration due to gravity and $\vec{F} = \nabla \sigma$ is the contribution from stresses within the ice. Scaling of surface stresses $\vec{\tau}_{ai}$ and $\vec{\tau}_{io}$ ($\vec{\tau}_{io} = c_{d,io} \rho_o (\vec{u} - \vec{u}_w) |\vec{u} - \vec{u}_w|$) with ice concentration A follows the suggestion of Connolley et al. (2004). The implementation of the EVP rheology follows the CICE model documentation (Hunke and Lipscomb (2001)) and uses an 'internal' time step of 60 s. The stress tensor is expressed in the standard way following EVP (Hunke and Dukowicz (1997)) rheology. Sea surface tilt force is computed using the dynamic elevation (sea surface height η) from the ocean model.

The temporal evolution of the three prognostic variables h_s , h , and A , is described by the following balance equations

$$\frac{\partial h}{\partial t} + \nabla \cdot (\vec{u}h) = S_h \quad (2.24)$$

$$\frac{\partial h_s}{\partial t} + \nabla \cdot (\vec{u}h_s) = S_s \quad (2.25)$$

$$\frac{\partial A}{\partial t} + \nabla \cdot (\vec{u}A) = S_A \quad (2.26)$$

where the first term on the left-hand side describes the local, temporal change and the second the effect of advection. The source terms on the right-hand side represent the thermodynamic changes, which are derived from the surface energy budget of Parkinson and Washington (1979).

The thermodynamic sea-ice growth rate S_h is calculated as an area weighted mean over the sea-ice covered and open water part of the grid cell. It consists of the contributions from growth rates at the atmosphere-ice interface (only melt and occasionally snow-ice conversion), at the sea ice base, and in the open water part of the grid cell.

The change in sea ice concentration S_A associated with thermodynamic sea ice growth is calculated using the empirical relationships following Hibler III (1979).

The source term S_s for snow (Owens and Lemke (1990)) includes accumulation from net precipitation and the surface melting (in case of a positive surface heat budget it is assumed that the snow cover will melt entirely before melting of the sea ice surface starts). Since snow ice formation due to flooding produces a significant part of the ice volume in the Southern Ocean (Eicken et al. (1994)), this effect is parameterized following Leppäranta (1983). When enough snow accumulates on the sea ice to submerge the snow-ice interface, calculated by using Archimedes' principle, water is assumed to enter the normally porous snow layer, so that this part of the snow is converted to ice.

Except for the inclusion of EVP rheology and the modification following Connolley et al. (2004), model equations and parameters (e.g., ice strength parameter $P^* = 20000 \text{ Nm}^{-2}$, lead closing parameter $h_0 = 1.0 \text{ m}$) are identical to the sea-ice component of the BRIOS model (Timmermann et al. (2002)).

Sea ice transport is computed using a backward Euler implicit advection scheme (see description in Danilov et al. (2004), except for differences that are due to the divergent form of sea-ice tracer equations). It conserves the total tracer quantity and has low dispersion. However, it is not strictly monotonic so that Laplacian diffusion with a diffusivity of $4000 \text{ m}^2/\text{s}$ is necessary to control the smoothness of the solution. We do not use stabilization in this version of the sea-ice model.

Coupling between ice and ocean is very similar to the BRIOS model (Timmermann et al. (2002)) and uses a flux-averaging method for heat, fresh water and momentum.

2.4 Initialisation and atmospheric forcing

Initial temperature and salinity have been derived from the World Ocean Atlas (WOA01) January mean dataset. *In-situ* temperature has been converted to potential temperature. In regions with an initial sea surface temperature below -1°C , we prescribe an initial sea ice thickness of 1 m, snow thickness of 0.1 m, and ice concentration of 0.9, which yields a sea-ice distribution that (at least for the Antarctic) is close to observed ice concentrations for January.

Atmospheric forcing fields for the simulations presented here have been obtained from the NCEP/NCAR reanalysis (Kalnay et al. (1996)) for the period 1958-2007. They consist of daily datasets for 10 m-wind, 2 m-temperature, specific humidity, total cloudiness and net precipitation, where the latter has been derived from the total precipitation and the reanalysis latent heat flux. A quadratic bulk formula with drag coefficients of $1.0 \cdot 10^{-3}$ and $1.32 \cdot 10^{-3}$ is used to compute the surface wind stress over open water and sea ice, respectively. Surface fluxes of sensible and latent heat follow empirical parameterizations of Parkinson and Washington (1979). Shortwave radiation is computed using the empirical formula of Zillman (1972) with the cloud correction of Laevastu (1960). Longwave radiation is parameterized as a function of 2-m temperature according to König-Langlo and Augstein (1994). No restoring is applied.

2.5 Configuration

For the study presented here, the model has been configured on a coarse-scale grid in a global domain (Timmermann et al. (2009)). It features a horizontal resolution of 1.5° ; in the vertical, 26 z-levels are used. In order to avoid a stepwise representation of bottom topography and to approximate bathymetry in a smooth way with realistic depths, nodes of bottom elements are allowed to deviate from z-levels, which is akin to the shaved-cells approach in z-coordinate finite-difference models. A total of 334070 grid nodes (of which 19643 are surface nodes) is used. Integrations start on Jan 1st, 1958 and use a 2 h time step.

Chapter 3

Ocean mass budget in the Finite Element Sea Ice Ocean Model

Ocean bottom pressure is computed as the pressure exerted on the sea floor by the overlying water starting from the atmospheric pressure. Anomalies of ocean bottom pressure are therefore equivalent to changes in ocean (or atmospheric mass). These changes can have different sources of origin: either ocean mass redistribution due to circulation anomalies, or net gain and loss of mass due to precipitation and evaporation, river runoff or land ice melting. To achieve a realistic representation of ocean bottom pressure, i.e. ocean mass, in ocean model simulations, a careful implementation of mass variation terms is essential. This task is further complicated by the fact that FESOM, like many other general ocean circulation models, relies on the Boussinesq approximation, so that it respects volume, and not the mass balance in its original formulation.

In this chapter, the newly implemented FESOM mass budget and the computation of ocean bottom pressure anomaly terms are discussed.

3.1 Computation of ocean bottom pressure

In general, the ocean bottom pressure p_b consists of two parts: the atmospheric pressure p_{at} and the hydrostatic pressure of the water column. The latter is split into two parts, the first being the integral from ocean bottom to the reference sea surface which is a surface of constant gravity potential, and the second the integral between this reference level ($z = 0$) and the actual sea surface η . Thus, p_b is computed as follows:

$$p_b = \int_{-H}^0 \rho \cdot g dz + \int_0^{\eta} \rho_0 \cdot g dz + p_{at}, \quad (3.1)$$

where H is the ocean depth, ρ_0 the reference density (1027 kg/m^3), ρ the density as a function of temperature, salinity and depth (pressure), and g the acceleration due to gravity (9.80665 m/s).

The *atmospheric pressure* part is considered to be the pressure at sea surface level, i.e. the pressure exerted by the atmospheric mass. This variable has to be provided as a time-varying boundary condition and is now part of the atmospheric forcing. Consistent with the other forcing we use the sea level pressure (SLP) data provided by the NCEP/NCAR reanalysis. The data is given on a daily basis for the entire time span of the model run, 1958-2007.

To compute the first part of the *hydrostatic pressure* (the integral from depth $z = -H$ to the reference sea surface $z = 0$) the full equation of state is taken for the density ρ as a function of temperature, salinity and pressure. Given that the model is required to compute *in-situ* density ρ from the potential temperature θ , we use the dedicated (empirical) relation of Jackett and McDougall (1995).

For the second part, the interval $z = 0$ to $z = \eta$, a constant reference density ρ_0 is used. This part represents ocean bottom pressure anomalies induced by *sea surface height variations*. In turn, the surface height variations are coming from several types of sources which include the variation in the ocean horizontal transport, direct mass sources and sinks, and also changes caused by steric expansion or contraction of the fluid column. In order to study the mass balances these sources should be consistently taken into account in the equation for sea surface height. Since it is seldom the case with existing OGCM we consider this question in more detail in the next section.

3.2 Sea surface height variability

Many ocean general circulation models (OGCMs), in particular those working in rigid lid approximation, only aim at a realistic representation of the circulation but not of the ocean mass budget. Sea surface height variations in these models are assumed to depend only on variations of the horizontal transport.

Recent OGCMs are, as a rule, taking the mass sources into account and adjust the volume of the upper model layer accordingly. However, their focus is the implementation of the salt, and not mass balances. The main issue

here is that small imbalances in separate mass sources generally have a small impact on the ocean circulation, but may strongly affect the ocean mass tendencies. We discuss this question in section 3.3

FESOM implements a *free surface* which means that the sea surface elevation can vary in time. It brings about some numerical advantages, the most important being the ability to incorporate mass sources and sinks. In the standard FESOM model (Timmermann et al. (2009)), variations in the sea level are determined solely by the dynamics (divergence of vertically integrated transport). Since we aim at a correct representation of the mass budget, FESOM was augmented so that it takes into account direct sources.

Direct mass contributions to be considered in this study are

Precipitation (rain and snow) and evaporation. *Precipitation* induces a change in the surface water density, changes the volume and add to the total mass of the water column. In turn, *evaporation* leads to a change in the density in the opposite direction and a mass and volume loss.

River runoff. *River runoff*, i.e. the water inflow from rivers into the ocean, also contributes to the ocean mass by adding fresh water to the ocean, similar to precipitation.

A more indirect contribution forms the **Sea ice**. Melting/freezing of sea ice is a source/sink of fresh water for the ocean. Thus, it changes the ocean density. Since this has no immediate effect on the ocean mass, the ocean bottom pressure remains unaffected. However, advection of sea ice is different from the advection of sea water, which can lead to a redistribution of mass.

Another significant source of sea level variability (apart from the transport divergence) is

Steric expansion/contraction. The sea level (which represents ocean volume) not only varies because of mass gain or loss, but also due to steric expansion or contraction, i.e. a change in the ocean density for example induced by surface heating or cooling. The water expands and contracts with rising and falling temperature, and so does the sea level.

The models formulated in the Boussinesq approximation are missing this effect. The way around this problem was suggested by Greatbatch (1994) who has shown how to modify the computations of elevation in a Boussinesq model. The Greatbatch correction is now a part of FESOM.

In this study we consider the contributions from precipitation, evaporation and surface runoff, ensure a realistic conversion of sea ice to equivalent sea level and take into account the changes due to steric expansion and contraction. The details of the implementation into the model are described in the following sections.

It should be mentioned that there are other processes that may affect the

sea level variability directly or indirectly, which are not taken into account in our study. In particular, they include

Ice sheet melting. Meltwater from ice sheets like the Greenland or Antarctic ice sheet contributes to the ocean mass and leads to an increase of sea level. At the same time the "solid" earth adjusts to the ice mass loss by an upward movement. This *glacial isostatic adjustment* (GIA), which is a reaction to post and present mass loading changes of the solid Earth, might lead to a local equilibrium between sea level rise and the land movement in certain locations, but in general the effects cannot be expected to balance each other exactly. At present the global sea level sinks at a rate of 0.3 mm/a due to GIA (Douglas and Peltier (2002)). At the same time, the mass loss of the ice sheet causes a decrease in *self-gravitational attraction*.

Crustal movement. Another factor that can influence the sea surface height is the *crustal movement*. The solid Earth, although it is called "solid", is flexible and undergoes fluctuations. So a drop of the ocean floor will also have an impact on the local surface elevation. This can indirectly influence the ocean mass distribution.

3.2.1 Introduction to the Boussinesq approximation

The Boussinesq approximation is a widely used simplification that builds on the fact that density variations in the ocean are small. As applied to the momentum and continuity equations it can be briefly formulated as follows: replace density with a reference density everywhere except when it is multiplied with the acceleration due to gravity. The computational effort is strongly reduced in the Boussinesq approximation as it filters out the sound waves. A derivation of the Boussinesq approximation can be found in many textbooks (see, for example, Vallis (2006), Atmospheric and oceanic fluid dynamics). The main implication for the analysis in this work stems from the fact that it leads to a modification of the *continuity equation*, which describes the conservation of mass in the ocean.

Instead of the true continuity equation,

$$\frac{\partial \rho}{\partial t} + \nabla \cdot (\rho \mathbf{v}) = 0, \quad (3.2)$$

the models formulated in the Boussinesq approximation work with the continuity equation in the form

$$\nabla \cdot \mathbf{v} = 0, \quad (3.3)$$

which expresses the volume conservation (fluid incompressibility). The omitted term, $\rho^{-1} D\rho/Dt$, describes local expansions or contractions caused by

density changes which are needed to recover a consistent mass balance. However, it has a limited effect on the flow dynamics provided that

- velocities must be small compared to the speed of sound which ensures that dynamics affect the density only slightly.
- the phase speed of waves or disturbances must be small compared with the speed of sound c .
- the vertical scale of the motion must be small compared with c^2/g where g is gravity.

These assumptions generally hold for oceanic flows, which ensures that oceanic flows can be treated as being incompressible.

3.2.2 Contribution of fresh water fluxes and steric changes to sea level

Changes in surface elevation are given by the integration of the continuity equation considering any surface mass flux S :

$$\frac{\partial \eta}{\partial t} + \nabla \cdot \int_{-H}^{\eta} \vec{u} dz + \int_{-H}^{\eta} \frac{1}{\rho} \frac{D\rho}{Dt} dz = S, \quad (3.4)$$

The third term on the left hand side is omitted in the Boussinesq approximation, and the original FESOM (Timmermann et al. (2009)), like other models based on this approximation, only considers a displacement of the sea level $\frac{\partial \eta}{\partial t}$ by horizontal transport:

$$\frac{\partial \eta}{\partial t} + \left(\frac{\partial U}{\partial x} + \frac{\partial V}{\partial y} \right) = 0, \quad (3.5)$$

where U and V are the vertically integrated velocities (transports) in x and y direction respectively. Steric effects, i.e. the expansion/contraction of sea water for example due to heating/cooling, and changes of the ocean volume due to surface freshwater fluxes are neglected.

In order to obtain a more realistic representation of ocean mass variability, we considered the contributions from:

- steric sea surface height changes
- contributions from precipitation, evaporation and land surface runoff

- fresh water fluxes between the ocean and the sea ice part of the model

The term "steric" comprises changes of the water column thickness due to changes in density. Together with variations in dynamic topography and freshwater inflow steric changes determine sea level anomalies. With regard to global sea level rise, steric effects are dominated by expansion due to temperature rise ("thermosteric effect"), locally the effect of salinity variation ("halosteric effect") is not negligible. Neither of those effects is considered in Eq. 3.5 which is the consequence of incompressibility equation (and the Boussinesq approximation).

However, in the model heating causes a change in density which is directly related to a change in the hydrostatic pressure in the water column below. If the sea surface height is not corrected for the thermal expansion, this would lead to an unrealistic decrease in the total bottom pressure. It can be compensated if one re-considers the term $-\frac{1}{\rho} \frac{D\rho}{Dt}$, which captures changes in sea level due to density variations, but has been omitted from the continuity equation due to the Boussinesq approximation. Since Eq. 3.5 is obtained by vertically integrating the continuity equation, the steric effects can be recovered by adding

$$-\int_{-H}^{\eta} \frac{1}{\rho} \frac{D\rho}{Dt} dz$$

to the right hand side of Eq. 3.5. This term varies over horizontal coordinates and thus would affect the dynamics. However, as explained by Greatbatch (1994), such effects can safely be neglected. What is important for the global mass balance is the area-averaged globally uniform correction due to this term. In this case adding such a correction only re-defines the elevation without any significant effect on the dynamics. In practical implementation, the full density derivative is computed by the known fields from the preceding time steps. Vertical integration and horizontal averaging is straightforward.

Fresh water fluxes, due to precipitation, evaporation or runoff, induce changes in density as well as in mass. In the standard FESOM, the freshwater fluxes are only taken into account in computations of *virtual salt flux*; freshwater input leads to a freshening, freshwater extraction to a salt enrichment. In reality however, freshwater input (for example due to rain) also induces an increase of the total water mass. When only the freshening is taken into account and the sea surface height stays constant, total mass (i.e. globally integrated ocean bottom pressure) in the model decreases although water is added to the ocean. Therefore, in order to capture oceanic mass variations in a realistic way, the density variations have to be compensated by adequate changes of sea surface elevation.

Nearly the same is true for the contributions from ice and snow. Melting and freezing of sea ice are treated as freshwater fluxes into and out of the ocean, respectively. As described above, this is realised by a virtual salt flux which must be corrected by the additional contribution to the sea surface height. Furthermore, snow and ice mass are included in the total ocean mass. This is done by transferring the snow/ice volume to an equivalent water column height using the density ratio of ρ_{ice}/ρ_W and ρ_{snow}/ρ_W , where $\rho_{ice} = 910 \text{ kg/m}^3$ and $\rho_{snow} = 290 \text{ kg/m}^3$. It is tempting to assume that the total mass of ice and water cannot change, so that the mass exchange between ice and ocean can be ignored for the computation of total ocean mass. However, sea ice (and snow) moves with a drift speed different from the ocean currents, so that the advection of sea ice must be taken into account for the determination of the correct position where the ice mass adds to the total mass. Snow volume on the other hand contributes to ocean bottom pressure during the time from accumulation to melting so that a mechanism for the treatment of ice and snow mass is required anyway.

In total we arrive at a prognostic equation for sea surface height considering freshwater contributions and steric effects which reads:

$$\frac{\partial \eta}{\partial t} + \nabla \cdot \int_{-H}^{\eta} \vec{u} dz = - \int_{-H}^{\eta} \frac{1}{\rho} \frac{D\rho}{Dt} dz + (P - E) + R + F + \frac{DM}{Dt}, \quad (3.6)$$

where H is the depth, P the precipitation, E the evaporation, R the surface runoff and F the net water flux due to melting/freezing of ice and snow and M the volume of ice and snow in equivalent water column height.

3.3 Global surface freshwater flux budget

Given that the freshwater flux due to freezing and melting of sea ice is zero in the long-term global mean, the only relevant contributors to the ocean surface fresh water flux are the net precipitation (i.e. precipitation minus evaporation) and the runoff from land (i.e. river runoff and melt water from continental ice sheets). In this section we discuss the way those two quantities add to the oceanic mass budget and how their contributions are considered in the ocean model.

3.3.1 Contributions from net precipitation and runoff to ocean mass

Evaporation, precipitation and land surface runoff are part of the Earth's *hydrological cycle*, which describes the continuous movement of water on, above, and below the surface of the Earth. Water in all three states, i.e. liquid, vapor and ice, is considered. Except for a very small exchange with the interplanetary space, the total water balance of Earth is closed. Thus, this mechanism is correctly called a "cycle".

The main driving force of the hydrologic cycle is the sun. Solar radiation heats the ocean surface. Water is evaporated and carried to the upper atmosphere by rising air. Cooler temperatures at higher levels cause the water vapor to condense to clouds, which move with the air currents. Accumulation of cloud particles leads to precipitation.

Part of the precipitation drops back into the ocean, but some of the evaporated water is carried to the continents where it feeds the land hydrology. Therefore, the net precipitation over the ocean is negative in the long-term global mean. On land, there are various possibilities for the precipitation to contribute to the land hydrology. Precipitation can be snow falling on ice sheets, ice caps, or glaciers, where it can remain many years. Rain will seep into the soil and add to the ground water or feed plants. Another part directly returns to the ocean by runoff. Natural and man made storage on land and its change cause a delay in the hydrologic cycle, which results in a global sea level with an annual amplitude of about 10 mm (Chen et al. (2001)).

River discharge and runoff in general is estimated to be more than 1 Sv, i.e. $10^6 \text{ m}^3/\text{s}$ in the global integral. If we compare this value to the total amount of net precipitation over the ocean which is approximately -1 Sv , we see that the runoff balances the water loss due to the excess evaporation of the ocean.

3.3.2 Surface freshwater budget in the Finite Element Sea Ice–Ocean Model

As described in section 3.2, contributions from precipitation, evaporation and runoff are considered in the computation of the sea surface height. The numbers for these quantities are derived from data sets provided by weather forecasting centers.

Precipitation and evaporation for the global FESOM used here are derived from the NCEP/NCAR reanalysis data. While precipitation is directly

provided by the data center, evaporation E is calculated from the latent heat flux Q_l as follows:

$$E = \frac{Q_l}{\rho_W \cdot l_{evap}} \quad (3.7)$$

where $\rho_W = 1000 \text{ kg/m}^3$ is the water density and $l_{evap} = 2.5 \cdot 10^6 \text{ J/kg}$ is the latent heat of evaporation.

Within the FESOM implementation the daily data from NCEP reanalysis for the latent heat flux and the total precipitation which are given on a regular $1.75^\circ \times 1.75^\circ$ are interpolated to the finite element grid. The total precipitation is combined with the evaporation computed from the the latent heat flux according to equation 3.7 which leads to a representation of the net precipitation (in [m/s]).

Since runoff is not provided by the NCEP reanalysis it is derived from the Hydrological Discharge Model (HDM) (Walter (2007)) which was forced with atmospheric forcing data from the European Centre for Medium-Range Weather Forecasts (ECMWF). The runoff is derived from daily data and given in volume inflow [m³/s]. The data is provided on a $1^\circ \times 1^\circ$ rectangular global grid.

In order to use the HDM river runoff for the FESOM forcing, one has to take care for an appropriate mapping of the river runoff contributions to the finite element grid. Obviously, river runoff is located at the coasts. Therefore, for each point of the HDM grid where the flux is non-zero we determined the closest node at the FESOM coast. Runoff data are then interpreted as a volume flux [m³/s] for each point of the HDM grid. The corresponding coastal nodes of the FESOM grid are representative for an area given by the surrounding grid triangles.

Dividing the volume fluxes by this "cluster area", the volume transport from the HDM can then be converted to a surface freshwater flux [m/s] in a way that conserves the volume flux.

Neither of the data centers providing atmospheric reanalysis data claims that their flux data represent the global long-term mean correctly. It is therefore not surprising to find that for the existing data sets net precipitation over the ocean is not exactly balanced by runoff. A quantification of the effect of uncorrected fields on the global fresh water balance is given by a comparison of the global averaged net precipitation and river runoff and the sum of both (Fig. 3.1). If we apply a 5-year low pass filter on $P - E + R$, a global signal of up to 0.5 Sv remains.

In a 50 year simulation with FESOM, this leads to unrealistically large fluctuations in the global mean ocean mass (Fig. 3.2). The calculated mass

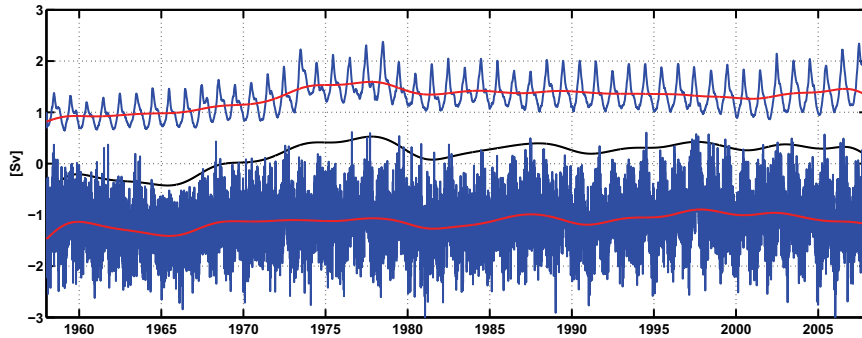


Figure 3.1: Time series of globally averaged runoff (upper blue curve) and precipitation-evaporation (lower blue curve), the 5-year low pass filtered time series of both (red), and their sum (black).

shows an increasing trend over the last 30 years of the simulation (approximately 3 cm/yr increase in equivalent water column height).

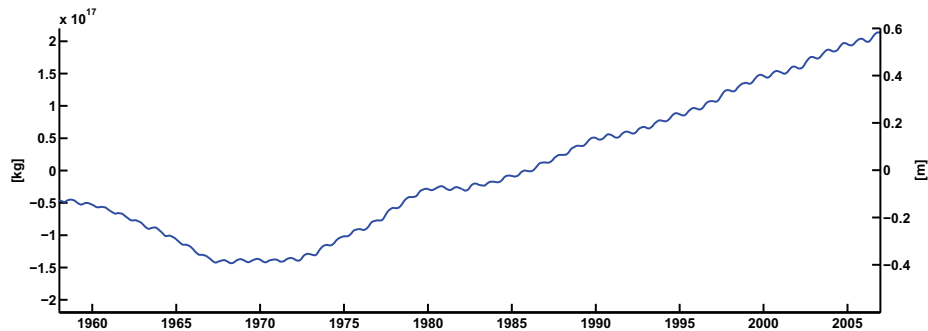


Figure 3.2: Time series of global mean ocean mass anomalies without adjustment of runoff.

To overcome this deficiency, we developed a surface freshwater flux fitter which assumes net precipitation and runoff to be globally balanced on time scales of more than 5 years.¹ We decided to adjust one quantity, the river runoff, in order to meet the assumption (Fig. 3.3).

¹Note that this is an assumption only. In reality, precipitation contributing as snow to the land hydrology may be bound for a longer period than 5 years. Also, contributions from melt water are not taken into account. The model is not meant to reproduce trends in the global ocean mass.

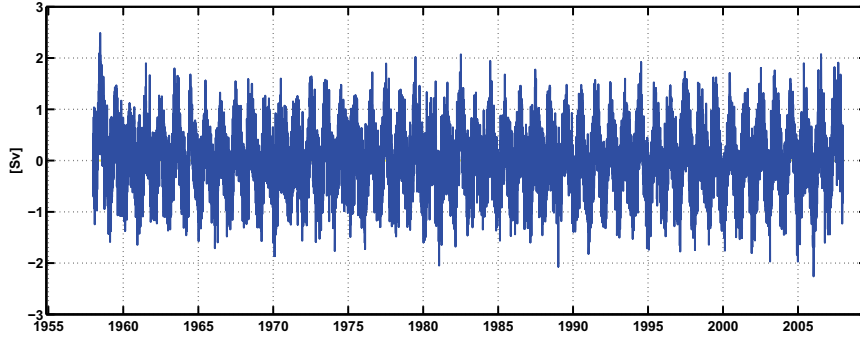


Figure 3.3: Time series of globally averaged adjusted runoff plus net precipitation.

In the first step of the filter algorithm, a 5-year low pass filter is applied to the daily time series of globally averaged net precipitation $P_{net} = P - E$ and runoff R , then introduce a time-dependent scaling factor α and assume that for each time t the filtered net precipitation \tilde{P}_{net} and the filtered runoff \tilde{R} are balanced:

$$\tilde{P}_{net}(t) + \alpha(t)\tilde{R}(t) = 0, \quad (3.8)$$

From this we compute the scaling factor²:

$$\alpha(t) = -\frac{\tilde{P}_{net}(t)}{\tilde{R}(t)}. \quad (3.9)$$

In the last step, the daily runoff fields interpolated on the FESOM grid as described above, are multiplied with α :

$$R(\vec{x}, t) = \alpha(t)\hat{R}(\vec{x}, t), \quad (3.10)$$

(where \hat{R} is the original daily data set derived from the HDM) and applied as part of the surface boundary conditions.

The achievements of the correction can clearly be seen in the global mean ocean mass calculated from a 50 year simulation where the runoff correction has been applied (Fig. 3.4). The unrealistic trend in the model data has vanished. A small increasing trend remains over the first years of the model run. However, after the spin-up period the global mean ocean mass shows an

² α typically varies slowly with time, e.g. for the year 2004 α increases from 0.76 to 0.8.

almost constant annual cycle at a mean annual amplitude of approximately $3 \cdot 10^{15}$ kg (8 mm equivalent water column height).

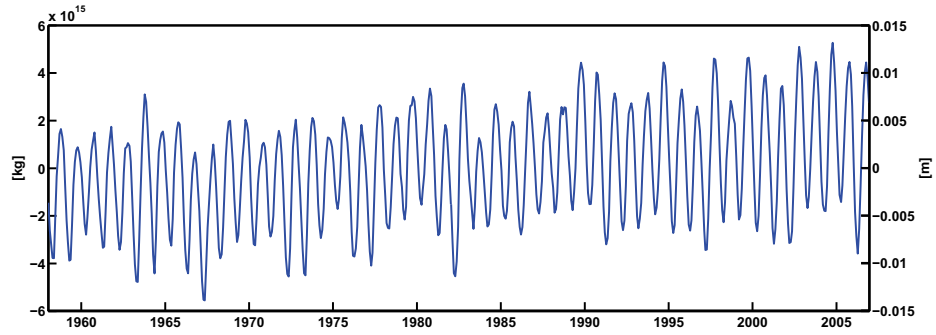


Figure 3.4: Time series of global mean ocean mass anomalies with adjustment of runoff.

Chapter 4

Evaluation of *in-situ* ocean bottom pressure and validation of FESOM

The ability of FESOM (and later on of GRACE) to globally provide bottom pressure related oceanic mass transport changes may be validated against *in-situ* observations of ocean bottom pressure. However, *in-situ* bottom pressure data give a localized representation of the prevailing mass redistribution. These point observations are influenced by local effects and small scale variability, which a model at horizontal resolution of 1.5° or satellite measurements will not reproduce. Nevertheless, depending on the region's bottom topography, on longer time scales the *in-situ* OBP records may be expected to reflect larger spatial scale phenomena. In particular a comparison of *in-situ* OBP data and modeled (and eventually GRACE-derived) OBP data on different spatial and temporal scales will allow a comprehensive error assessment of model (and GRACE) solutions.

4.1 The Ocean Bottom Pressure Database

In the framework of the BMBF project "Improved GRACE Level-1 and Level-2 Products and their Validation by Ocean Bottom Pressure", all available OBP data concurrent with the GRACE operation period 2002 - present were entered into the AWI's database of *in-situ* OBP (Macrander et al. (2009)). Contributing projects, collaborating institutes and responsible researchers are listed in Table A.1 in the appendix. At present, the database¹

¹Data available on request: andreas.macrander@awi.de.

contains time series from 85 deployments at 38 different locations of predominantly 1 year duration.

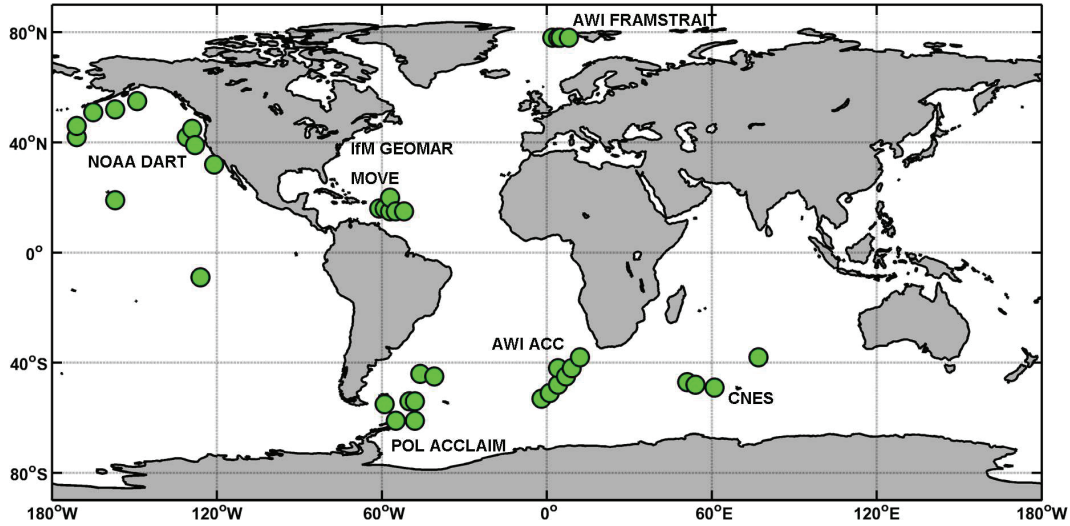


Figure 4.1: Positions of the BPRs.

All data were quality controlled. Outliers, pre-deployment values and pressure jumps were removed. A common problem of pressure sensors is their long-term drift, with larger drift rates during the first weeks to months of the deployment and smaller drift rates later on. The nonlinear drift characteristic prohibits a linear interpolation between pre- and post-deployment calibrations (if these are available at all). Therefore, sensor drift was eliminated by an empirical exponential-linear least square fit (Fig. 4.2). Thus, the *in-situ* data can not be used to evaluate annual to interannual OBP trends. On seasonal and shorter timescales, however, the accuracy of *in-situ* measurements is much better. E.g., pressure sensors from Paroscientific that are widely used, achieve a resolution of 0.001 dbar, with an absolute accuracy of 0.01 % of the full pressure range (University of Rhode Island (2006)).

Sampling rates of the raw data lie between 15 seconds (DART tsunami early warning system) to 1 hour for some other instruments. For high-resolution time series, temporal spacing was downsampled to 30 minutes using a 6th order polynomial fit windowed on 6 hours of data, thus eliminating noise and covering small data gaps while retaining tidal variability.

An essential part of making the *in-situ* data available for a comparison to FESOM and GRACE-derived data is the correction for tides of the pressure measurements. This correction is necessary in order to separate the OBP variability of interest from the variability introduced by tidal motion. In the frame of this study tidal variability was derived from a global tidal

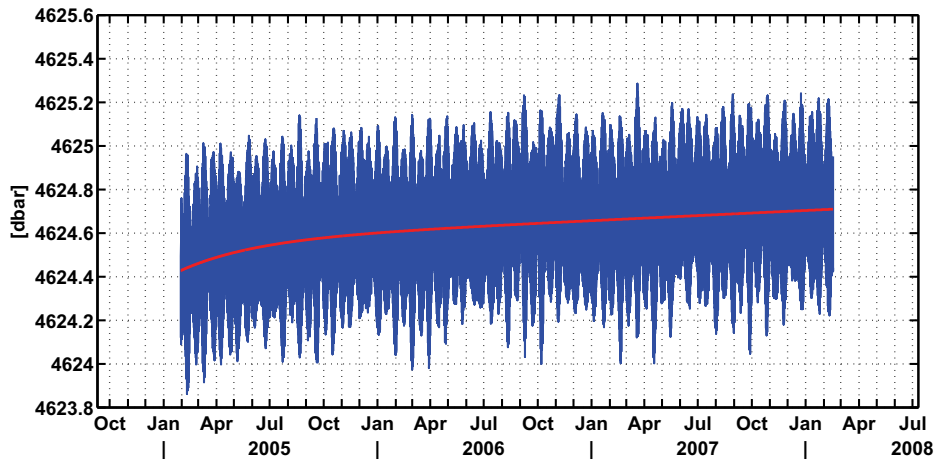


Figure 4.2: Time series of *in-situ* OBP at 47° S, 4° E. Blue line indicates the original time series, red line the drift correction.

chart (FES2004) and subtracted from the BPR measurements in order to obtain consistency between the *in-situ* and GRACE data, which are de-aliased utilizing the FES2004.

The impact of a tidal correction on the time series (e.g. amount of reduction of amplitudes) is analyzed in an additional comparison between empirically derived tides and tides from the FES2004 tidal chart.

4.2 Tidal variability in ocean bottom pressure data

The temporal signal of OBP measured by a bottom pressure recorder is dominated by tides. The tidal variability reaches amplitudes of approximately 1 m water column height (Fig. 4.3) which is large compared to the expected signal of up to 10 cm for meso-scale variability. Thus, for an investigation of non-tidal ocean mass variability and hence the validation of FESOM and GRACE a tidal correction of OBP measurements is required.

The term "tides" denotes the mass movement on a planet due to gravitational attraction of extra-planetary celestial bodies. Tides on Earth fall into three categories: solid Earth, oceanic and atmospheric tides. The driving force of tides on Earth is the small change in gravity due to motion of the moon and sun relative to Earth. These small variations in gravity arise from two separate mechanisms.

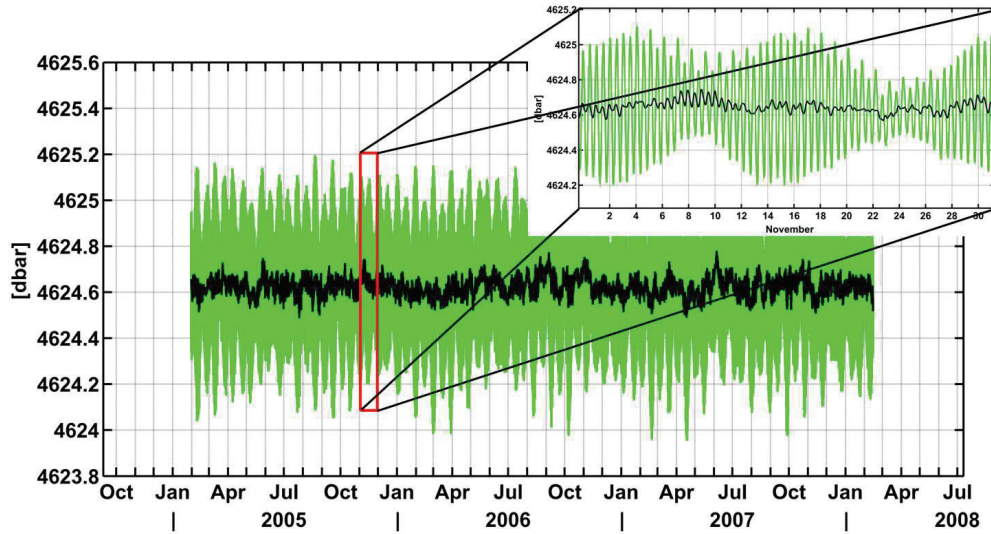


Figure 4.3: Time series of *in-situ* OBP at 47°S , 4°E . Green line indicates the drift corrected time series and the black line the tide- and drift-corrected time series.

1. Moon and Earth rotate about the center of mass of the Earth-moon-system. This gives rise to a centripetal acceleration at Earth's surface that drives water away from the center of mass and toward the side of Earth opposite moon.
2. At the same time, mutual gravitational attraction of mass on Earth and the moon causes water to be attracted toward the moon.

As the moon rotates about the Earth and the Earth-moon-system rotates about the sun in elliptic orbits, several mechanisms on different time scales cause a change in the tidal potential. The period of the lunar tidal potential can be separated into three terms with periods near 14 days, 24 hours, and 12 hours. Similarly the solar potential has periods near 180 days, 24 hours, and 12 hours. Thus, there are three distinct groups of tidal frequencies: twice-daily, daily, and long period (Tab. 4.1).

By using those frequencies, Doodson (1922) expanded the tidal potential in a Fourier series. In total Doodson derived 399 tidal contributions. The tidal constituents with largest amplitudes are the following (Table 4.2):

Frequency	($^{\circ}$ /hour)	Period	Source
f1	14.49205211	1 lunar day	Local mean lunar time
f2	0.54901653	1 month	Moon's mean longitude
f3	0.04106864	1 year	Sun's mean longitude
f4	0.00464184	8.847 years	Longitude of Moon's perigee
f5	-0.00220641	18.613 years	Longitude of Moon's ascending node
f6	0.00000196	20,940 years	Longitude of sun's perigee

Table 4.1: Fundamental Tidal Frequencies

Tidal Species	Name	Equilibrium Amplitude (m)	Period (h)
Semidiurnal			
Principal lunar	M_2	0.242334	12.4206
Principal solar	S_2	0.112841	12.0000
Lunar elliptic	N_2	0.046398	12.6584
Lunisolar	K_2	0.030704	11.9673
Diurnal			
Lunisolar	K_1	0.141565	23.9344
Principal lunar	O_1	0.100514	25.8194
Principal solar	P_1	0.046843	24.0659
Elliptic lunar	Q_1	0.019256	26.8684
Long Period			
Fortnightly	Mf	0.041742	327.85
Monthly	Mm	0.022026	661.31
Semiannual	Ssa	0.019446	4383.05

Table 4.2: Equilibrium amplitude and period of the main tidal constituents.

Although the theoretical principles of tidal processes are well understood, tidal prediction still constitutes a challenging task. The Earth's complex geometry induces changes in the tidal signal which are difficult to evaluate. Tide gauge measurements complemented since the 1990s by satellite altimetry help to enhance our knowledge about tides in the ocean. Assimilation of these measurements into hydrodynamic tidal models leads to global tidal charts, which are utilized for tidal prediction.

For the prediction of tides from *in-situ* observations two methods are commonly used: the *harmonic method* and the *response method*.

Both methods are based on the interpretation of tide gauge measurements. Tide gauges measure the rise and fall of the water column by de-

termining the pressure exerted on the gauge.² Analyzing the received data gives an approximation of the tidal constituents over the corresponding period. This approximation allows for a prediction of future tidal evolution in the respective region.

The *harmonic method* utilizes the knowledge that the measured signal is a superposition of the harmonic realizations of the tidal constituents. As the harmonics of each constituent can be represented by a sine with its own period and phase, the signal can be easily decomposed in the contributions from the main constituents. The so-derived functions are then re-merged to give a prediction of the tidal signal.

The *response method* developed by Munk and Cartwright (1966), calculates the relationship between the observed tide at a given location and the tidal potential. The relationship is the spectral admittance³ between the major tidal constituents and the tidal potential at each station. The admittance is assumed to be a slowly varying function of frequency so that the admittance of the major constituents can be used for determining the response at nearby frequencies. Future tides are calculated by multiplying the tidal potential by the admittance function.

Commonly, long data sets (of more than 18.6 years to resolve the modulation of the lunar tides) are required to determine accurate estimates of tides via the harmonic method, whereas data sets of only a few months are needed to obtain an estimate via the response method. The harmonic method is the traditional method and is widely used to determine tidal constituents from tide gauge data. However, for short data sets, like data from satellite altimetry or BPRs, the response method forms a capable alternative for tidal prediction. Here, we use the response method implemented in the IES⁴ Processing Tool (Kennelly et al. (2007)) to derive tidal variability from the *in-situ* measurements.

For the tidal correction of the GRACE data a third method of tidal prediction is used by the three processing centers: tidal modeling. Since the correction of the GRACE measurements requires a global representation of the tidal potential, a global tidal chart (here the FES2004 (Lyard et al. (2006))) derived from model simulations is utilized. The FES2004 is computed by a

²In this respect an ocean bottom pressure measurement is similar to a tide gauge measurement.

³The admittance is $Z(f) = G(f)/H(f)$. $G(f)$ and $H(f)$ are the Fourier transforms of the potential and the tide gauge data, and f is frequency.

⁴IES refers to the name of the measuring device, the Inverted Echo Sounder. The tool is designed to process IES data, but in newer versions also includes the processing software for the pressure data as provided by a PIES (Pressure sensor equipped Inverted Echo Sounder).

global finite element tide model, the CEFMO model. Data from satellite altimetry (TOPEX/POSEIDON and ERS) and tide gauges are assimilated via the variational assimilation code CADOR. The model gives a global description of the amplitude and phase of the principal tidal constituents, i.e. the short-period M_2 , S_2 , K_2 , N_2 , $2N_2$, O_1 , P_1 , K_1 , Q_1 , the fortnightly M_f and Mtm , $Msqm$, with periods around 7 and 9 days respectively, the monthly Mm , and non-linear M_4 .

Errors in the tidal chart lead to spurious signals in the GRACE solutions which alias to low frequencies and thus affect the monthly gravity field solutions. As computed by Ray et al. (2003), errors in short period K_1 , K_2 , S_1 , S_2 , and P_1 constituents are aliased by GRACE to periods of 7.48 years, 3.74 years, 322 days, 161 days, and 171 days, respectively. Findings of Seo et al. (2008) estimate the M_2 aliasing period to be around 140 days⁵. Hence, monthly solutions of the time variable gravity field are affected by errors in the high frequency constituents derived from tidal models. A comparison of the FES2004-derived tides with tides directly derived from OBP measurements gives an idea of how accurate especially the short-period tides are estimated by the model.

4.2.1 Correction for tides

To demonstrate the difference between a tidal correction using the tide model FES2004 versus a correction based on the response method, an analysis of tides in the AWI PIES (Pressure sensor equipped Inverted Echo Sounder) array in the South Atlantic has been performed. This array was set up in 2002 in the Atlantic sector south-west of Africa to monitor the influence of variations of the Antarctic Circumpolar Current in the Atlantic sector on water mass modifications in the Weddell Sea in the framework of the WECCON project (Weddell Sea Convection Control). The devices have been deployed along the TOPEX/POSEIDON track 133 covering the main branches of the Antarctic Circumpolar Current (ACC) south of Africa.

OBP data from 5 positions in the array equally spaced along the track (Fig. 4.4) are used. Measurements are sampled at a sampling rate of 2 samples/hr. Each device has been deployed for a 2-3 year period. Deployments have started in 2002, with ANT-7 and ANT-11, and are continued in 2005 with re-deployment of ANT-7, ANT-11 and complemented with ANT-3, ANT-5, ANT-537, ANT-9, and ANT-13.⁶. Thus, in total two time series

⁵Theory would give a period of 13.5 days at an approximate sampling rate of 12 hours. However, due to the monthly sampling of this period, the actual period was estimated to be around 140 days.

⁶Measurements at ANT-3 contain gaps in time series and cannot be taken into account

at ANT-7 (2002-2005 and 2005-2008), one at ANT-11 (2002-2005)⁷ and one at each of the other positions (2005-2008) are available for the tidal analysis.

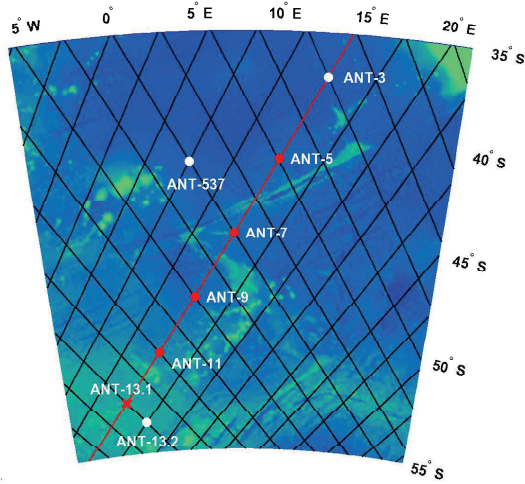


Figure 4.4: Map of locations of the BPRs used for the analysis of the tidal correction. Black lines indicate TOPEX/POSEIDON tracks, the red line track no. 133.

As we already saw from Fig. 4.3, the temporal signal of a BPR measurement is dominated by variations due to tides. A spectral analysis of the time series at the 5 locations in the BPR array gives a closer insight into the contribution of tides to the OBP signal (Fig. 4.5, left panel) on short time scales. The semi-diurnal and diurnal tides are highly pronounced in the energy spectrum at frequencies of 1 cycle/day and 2 cycles/day respectively. Energy of the diurnal tides apparently increases from North to South, whereas energy of the semi-diurnal tides decreases.

A similar north-south behavior can be detected in the tidal spectrum derived from the FES2004 (Fig. 4.5, right panel). Tides in the North of the array show a higher semi-diurnal and lower diurnal variability than in the South.

This indicates that amplitudes of the respective tidal constituents feature a north-south gradient. Plots of the amplitudes of the main semi-diurnal (M_2 , S_2 (Fig. 4.6)) and diurnal (K_1 , O_1 (Fig. 4.7)) constituents derived from the tidal chart FES2004 confirm this. The amplitude of the semi-diurnal

for a tidal analysis.

⁷The PIES deployed in 2005 was lost during recovery in 2008.

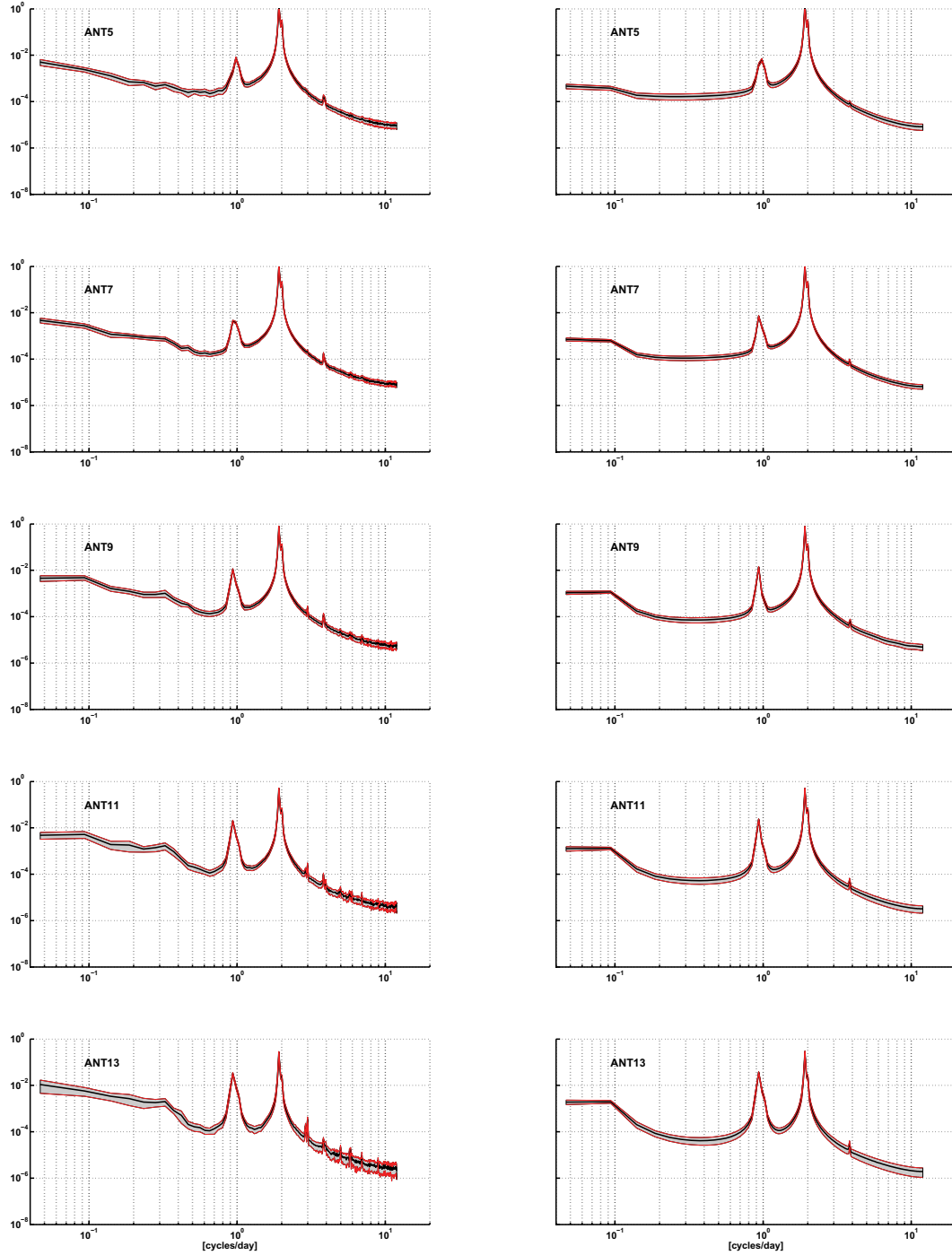


Figure 4.5: Power spectrum of OBP measurements (left panel) and FES2004 tides (right panel).

constituents is higher in the North and lower in the South. The opposite holds for the amplitude of the diurnal constituents: the signal features lower amplitudes in the North, whereas higher amplitudes occur in the South of the array.

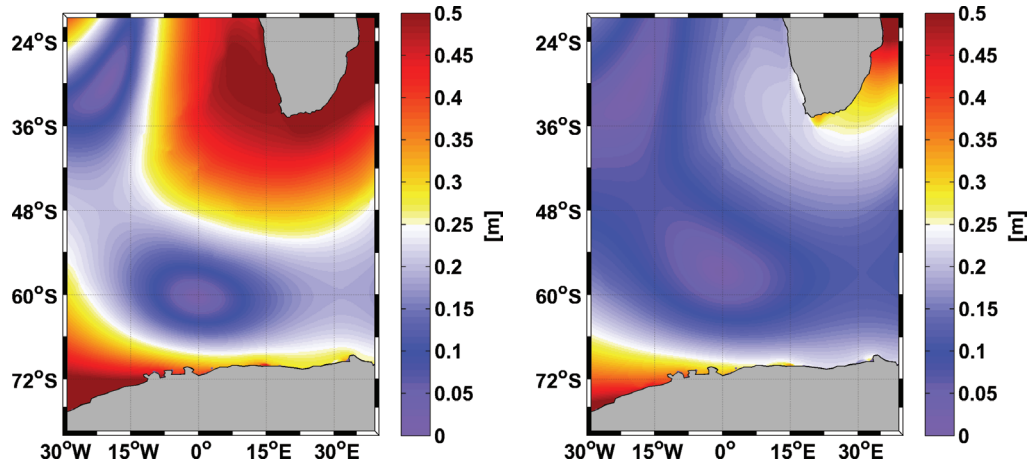


Figure 4.6: Amplitude of the M_2/S_2 tide derived from FES2004.

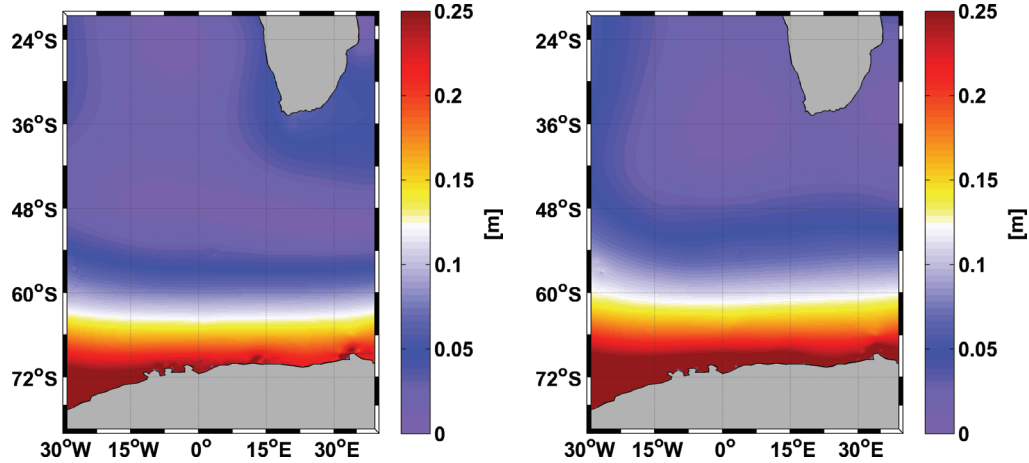


Figure 4.7: Amplitude of the K_1/O_1 tide derived from FES2004.

To evaluate the effect of a tidal correction, tides have been derived from the BPR measurements via the *response method* according to Munk and Cartwright (1966). The standard processing tool for PIES measurements (Kennelly et al. (2007)) developed at the University of Rhode Island provides a tidal analysis of the pressure time series based on this method. The contributions from the main tidal constituents (the short-period M_2 , S_2 , K_2 ,

N_2 , O_1 , P_1 , K_1 , Q_1 , the fortnightly M_f , and the semi-annual Ssa) to the observed signal can be derived from the OBP time series utilizing this tool.

An analysis of the phases of both corrections proves that the derived tides agree well in phase. A lagged correlation indicates a maximum correlation at a time lag of 0 hours (Fig. 4.8). The correlation is decreasing towards longer time periods. As tides are composed of periodic signals, the correlation rapidly fluctuates between values of 1 and -1 . However, the highest correlation appears clearly at the 0 lag and switches to -1 after approximately 6 hours. The alternating correlation can be referred to the semi-diurnal period which dominates the tidal signal.

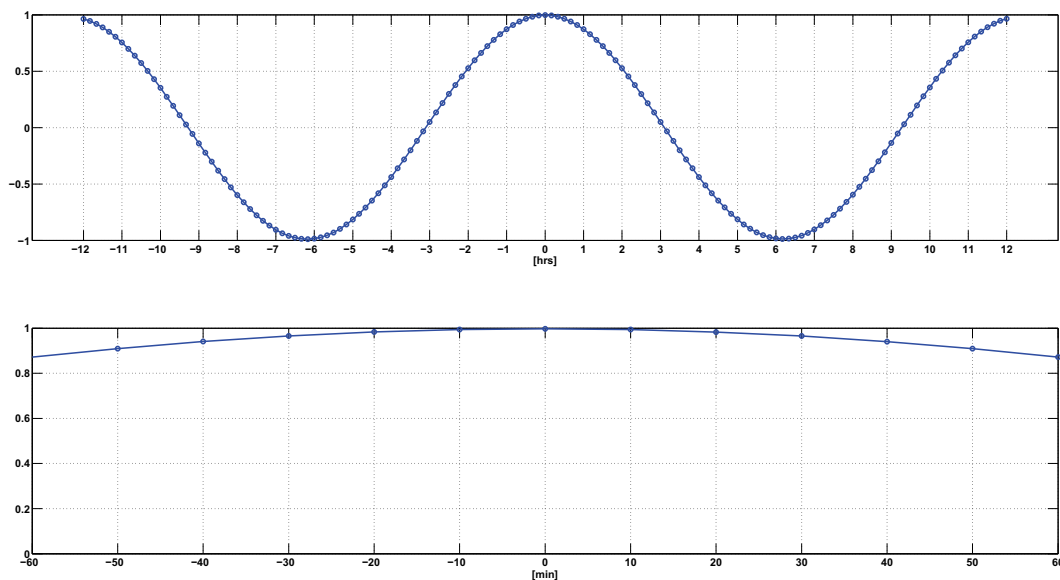


Figure 4.8: Lagged correlation of empirically determined and simulated tide at PIES position ANT-7.

Subtraction of the empirically derived tidal time series from the original OBP time series leads to the corrected OBP time series. The power spectrum of the corrected time series shows a clear reduction of the semi-diurnal and diurnal tides (Fig. 4.9, left panel). The power spectral density of the semi-diurnal and diurnal tides is reduced to $\leq 10^{-4}$. Signals of the diurnal tides in the South of the array, i.e. at ANT11 and ANT13, almost vanish completely. The power spectral density of the remaining semi-diurnal tides is around 10^{-4} at all positions.

When applying the correction derived from the tidal chart FES2004, a smaller correction of the short-period tides is achieved (Fig. 4.9, right panel). The signals of the semi-diurnal and diurnal tides in the corrected OBP time

series still show a spectral density of 10^{-3} .

Two quantify the differences between the empirically derived and the correction from the FES2004, the time series of tides provided by the two methods are compared (Fig. 4.10). The comparison of the two tidal corrections shows that both agree well in phase and feature similar amplitudes. Tides range between a surface height of approximately 60–160 cm. However, the difference between the time series shows a peak-to-peak range of about ± 5 cm. The standard deviation of the difference is at each PIES position around 2 cm.

4.2.2 Summary

In the AWI ACC PIES array, tides with amplitudes from 40 cm up to 80 cm can be observed. Spectral density induced by semi-diurnal tides decreases from North to South, whereas diurnal tides show a decreasing tendency. In order to resolve non-tidal variations of OBP, a correction of the measurements for tidal variability is required. Corrections derived from the tidal chart FES2004 and from the PIES measurements using an empirical approach have been compared.

The signal of the short-period tides, i.e. the semi-diurnal and diurnal tides, is significantly reduced in the OBP time series when corrected with the FES2004. However, the power spectral density of the corrected *in-situ* data shows that part of the tidal variability remains. Using the empirically derived correction reduces especially the diurnal, but also the semi-diurnal tide in the OBP time series to a large extent.

A comparison between the tidal variability derived from the tidal chart and from the BPR measurements indicates that both approaches feature the same phase. However, as already indicated by the differences in the spectral densities, the amplitudes of the derived tidal signals differ. The residual between both, the model- and observation-derived tides, shows synoptical scale anomalies of up to 5 cm. These differences may be referred to the unresolved short-period tidal constituents in the tidal model solution. Thus, for applications on short time scales, like an investigation of transport variability derived from OBP measurements, a tidal correction derived by the empirical response method might be preferred in order to evaluate the non-tidal oceanic variability.

As GRACE is corrected for tides by utilization of the FES2004, the difference between the modeled tides and the real tides especially for the high frequency constituents may lead to aliasing artifacts (as described before) in the GRACE solutions. Assimilation of the tidal signals derived from the measurements in this region could help to improve the tidal chart.

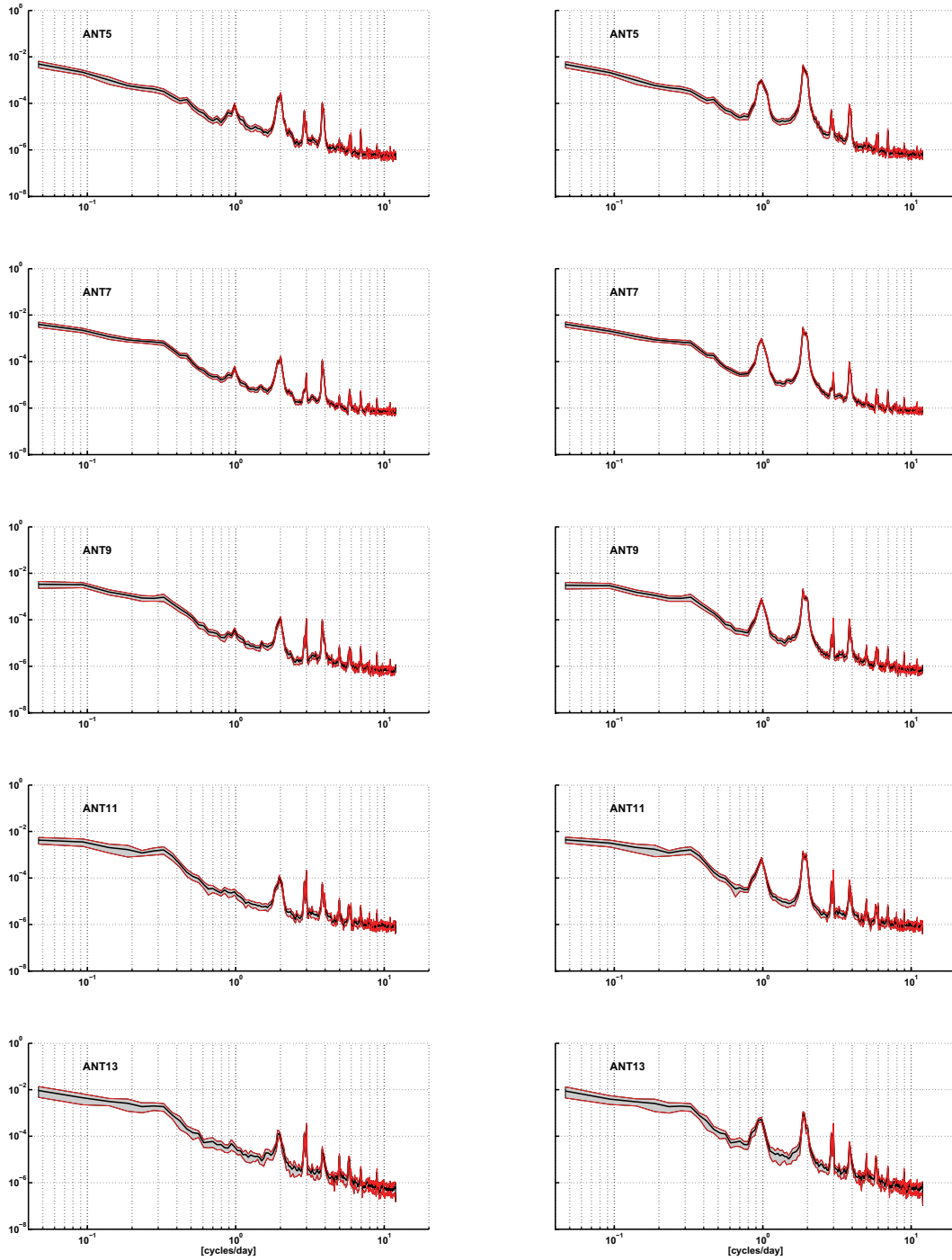


Figure 4.9: Power spectrum of the corrected time series. Left panel: correction after Munk and Cartwright (1966), right panel: correction utilizing the FES2004.

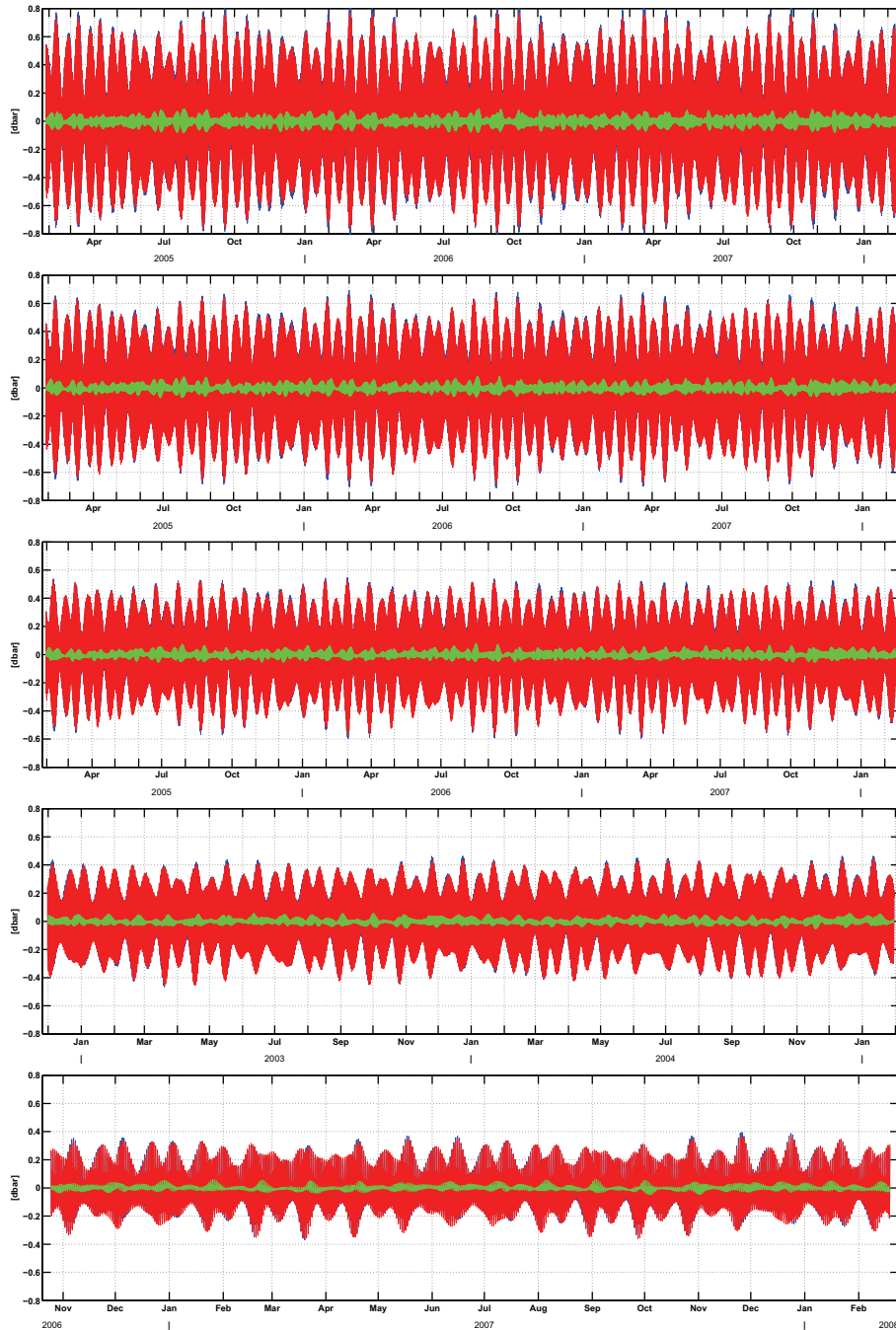


Figure 4.10: Tidal variability derived from an empirical analysis of the BPR data (blue) and the FES2004 (red). Green line indicates the differences between both time series.

4.3 Validation of FESOM

In chapter 3 the ocean model implementation was modified to obtain a realistic simulation of the ocean mass budget. This modification provides a strong reduction of unrealistic trends in the global average mass as induced by the atmospheric forcing. FESOM's ability to capture real oceanic variability on regional scales will be validated in the following by comparing simulated FESOM OBP against *in-situ* OBP observations.

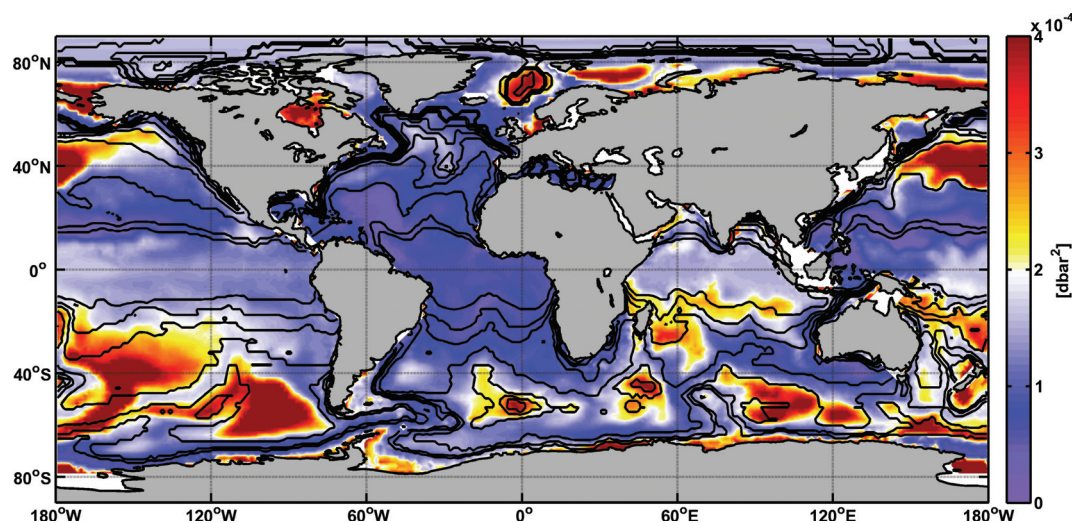


Figure 4.11: Variance of monthly mean OBP anomalies derived from FESOM simulations. Contour lines indicate f/H contours.

The variance of monthly mean OBP anomalies derived from FESOM simulations over the period from 2002-2007 features high variability especially at high latitudes (Fig. 4.11) and low variability at low and mid latitudes. The patterns of variability resembles f/H (f : Coriolis parameter, H : ocean depth) contours, reflecting the connection of OBP to the circulation (Fig. 4.11).

For the validation of FESOM we will show a comparison of FESOM and *in-situ* for two exemplary regions, one high and one low variance region (based on FESOM simulations). As a region showing high variance we considered the region south of Africa where the AWI ACC PIES array is located. The MOVE array in the tropical Atlantic, installed by the IfM GEOMAR in Kiel, constitutes an exemplary region with OBP low variance.

FESOM simulations indicate low variance of monthly mean OBP anomalies in the North of the array, whereas variance is higher in the south (Fig. 4.12). The structure of the pattern of high variability is related to the f/H

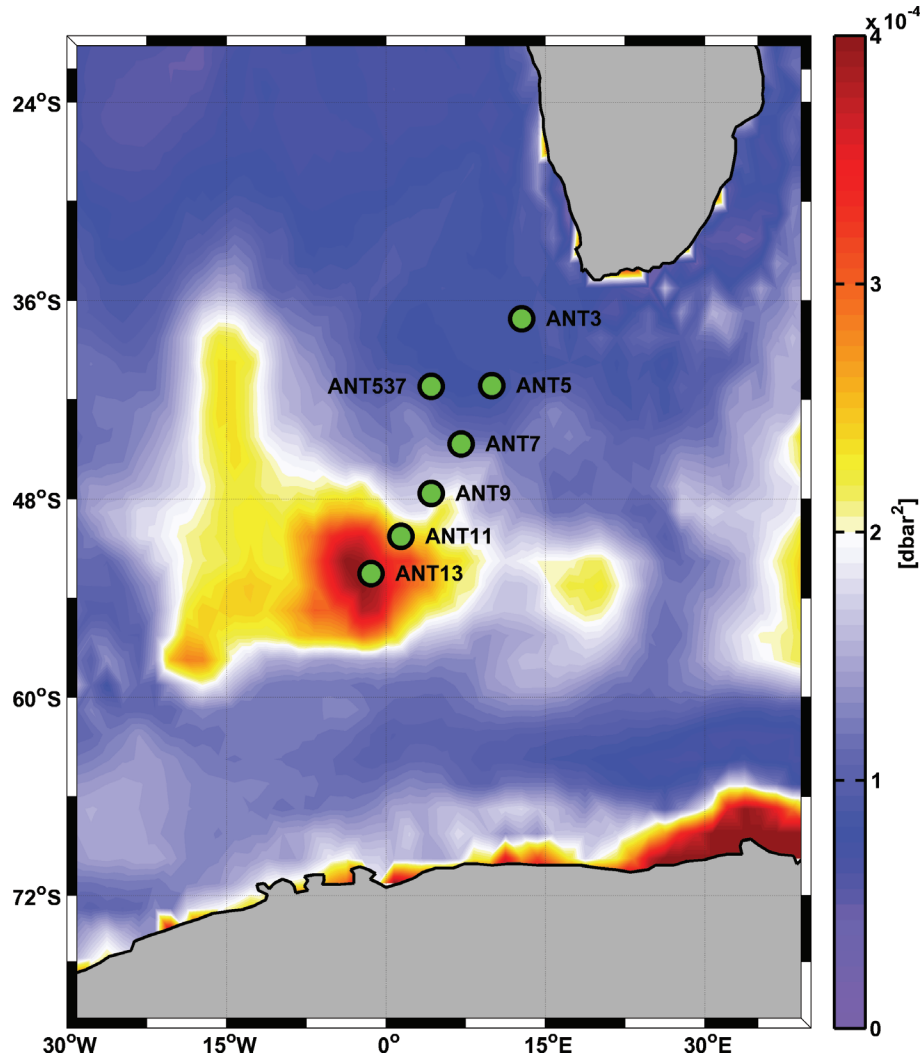


Figure 4.12: Variance of monthly mean OBP anomalies derived from FESOM simulations. Circles indicate positions of BPRs in the AWI ACC array which are used for validation.

contours (as explained before) in this region. The anomaly is limited by the Mid-Atlantic ridge in the West and the Atlantic Indic Ridge in the South.

As can be seen from the *in-situ* observations, the BPR measurements in the North feature high variability, in contrast to the model results (4.13). This indicates that the northern PIES are influenced by the strong variability in the Agulhas Basin, due to passing Agulhas Rings (Boebel et al. (2003)).

In the monthly anomalies derived from the *in-situ* measurements and FESOM simulations, the differences in variability can still clearly be detected

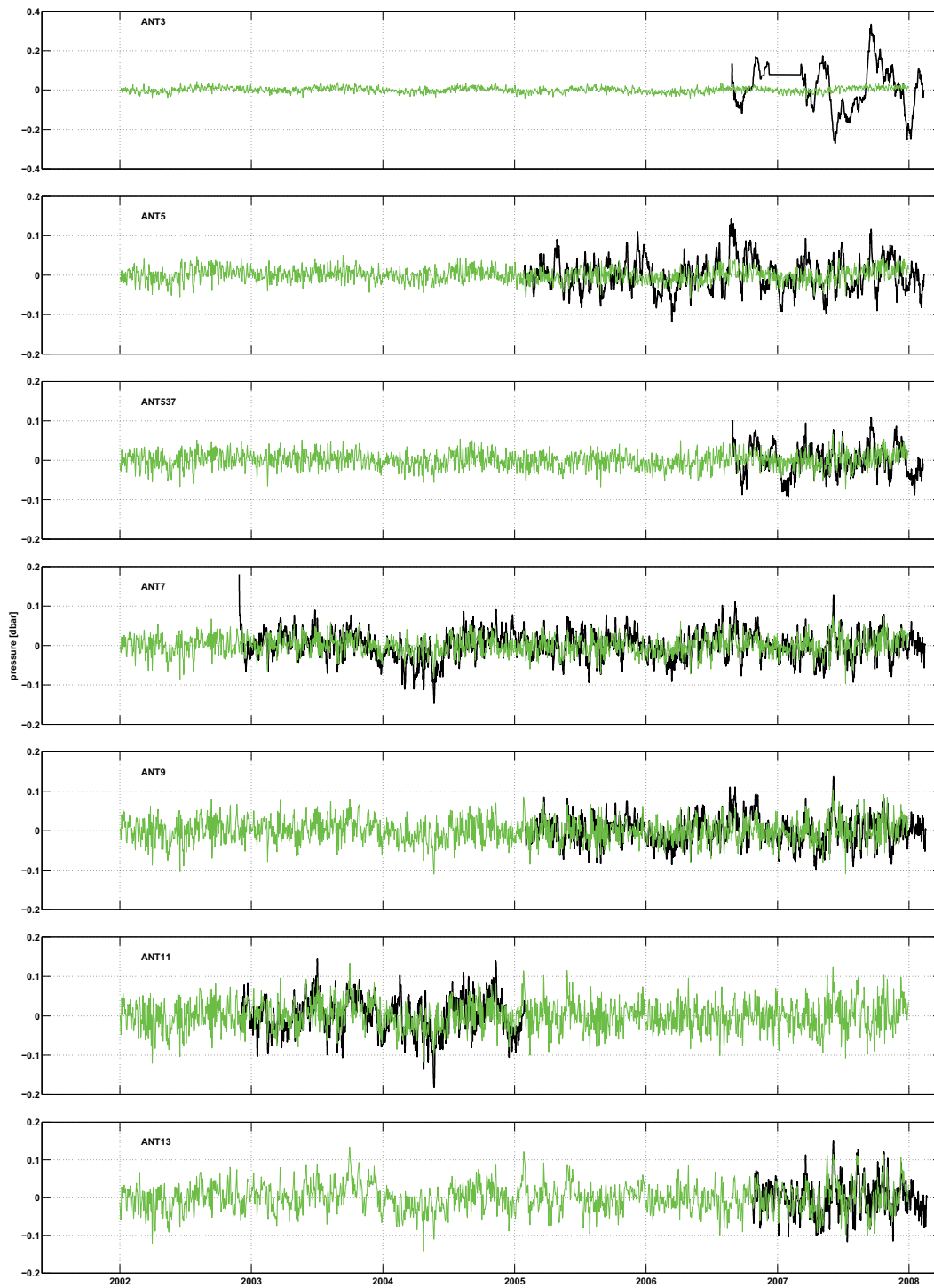


Figure 4.13: Daily mean derived from model simulations (green) and BPR measurements (black) in the AWI ACC array.

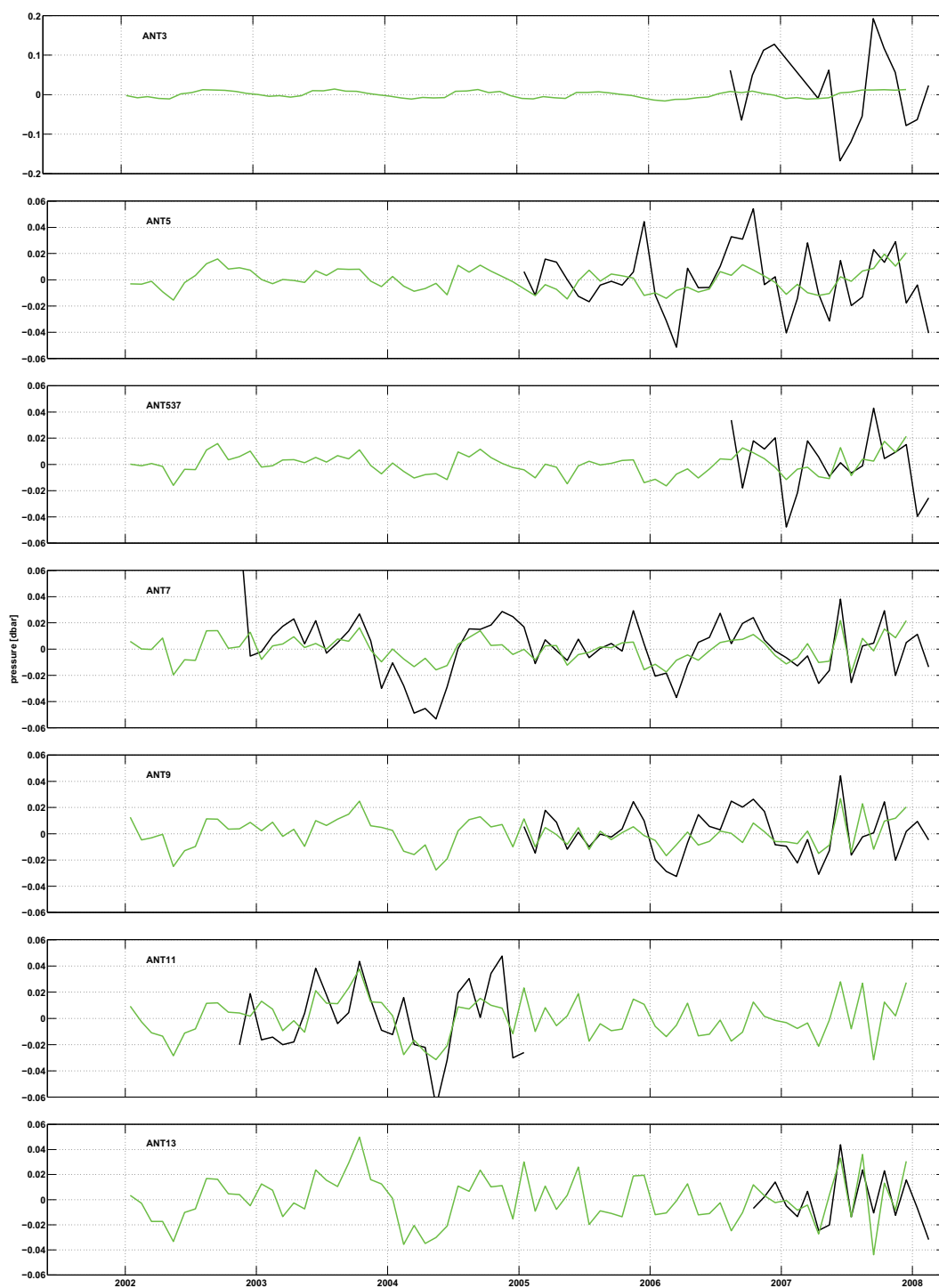


Figure 4.14: Monthly mean OBP anomalies derived from model simulations (green) and BPR measurements (black).

(Fig. 4.14). The PIES measurements in the North of the array (ANT3, ANT537, ANT5) feature high signal amplitudes which are not reproduced by the model. In the South the agreement between observations and modeled OBP anomalies is much better. These results are also supported by a spectral analysis of the time series (see also B). Many of the minima and maxima of the month-to-month variations are captured by FESOM (for example at ANT-7). However, the variability is underestimated by the model at a relatively coarse horizontal resolution of 1.5° .

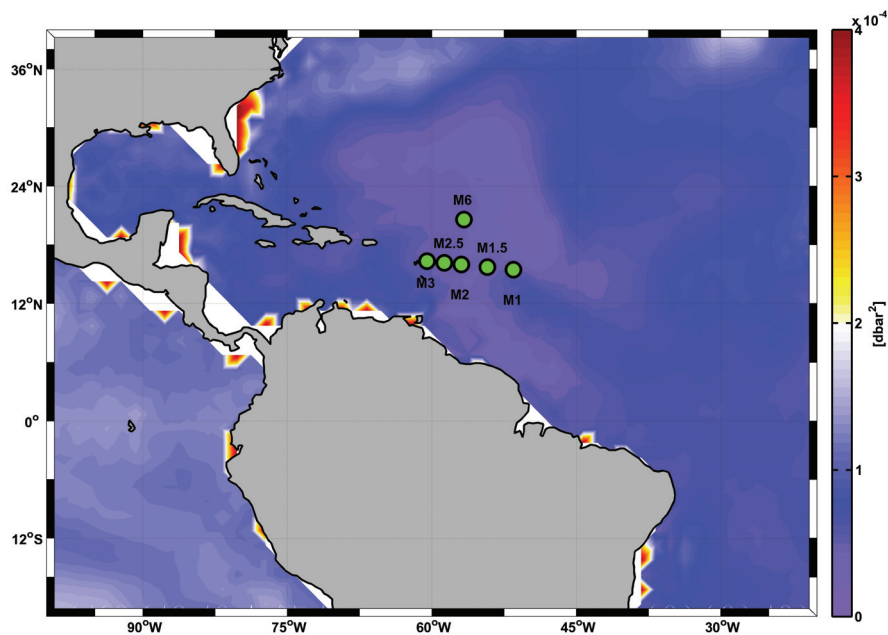


Figure 4.15: Variance of monthly mean OBP anomalies derived from FESOM simulations. Circles indicate positions of BPRs in the MOVE array which are used for validation.

Simulations with FESOM indicate relatively low OBP variability in the tropical Atlantic (Fig. 4.15). We compare the model results with measurements of a BPR array in this region. The MOVE (Meridional Overturning Variability Experiment) array has been designed to measure the influence of the interannual volume transport variability of the North Atlantic Deep Water (NADW) on the Meridional Overturning Circulation (MOC). It consists of traditional current meter moorings as well as PIES (positions indicated in

Fig. 4.15).

The measured time series have an amplitude of approximately 0.06 dbar (Fig. 4.17), which is actually smaller than the signal amplitudes measured in the ACC array. Highest variability can be detected at the PIES position M2. FESOM simulations indicate a similar range of variability in the array. However, amplitudes are slightly underestimated by the model.

On a monthly time scale, the OBP anomalies derived from model simulations show a dominant annual cycle. Highest correlations can be found with the western-most PIES time series, M3 and M2.5, where the annual cycle is more pronounced than at the other positions. The measurements at M6, M1.5, and M2 show higher month-to-month variability. This can be referred to small scale processes not resolved by the model or to unresolved tidal variability which are not canceled out in the monthly mean.

Comparisons of simulated OBP anomalies with all *in-situ* data available from the OBP data base with respect to correlation and standard deviation provide a more spatially extended view on the ability of FESOM to capture observed oceanic variability. High correlations at a significance level 95 % can be found at many locations in the global ocean (Fig. 4.18).

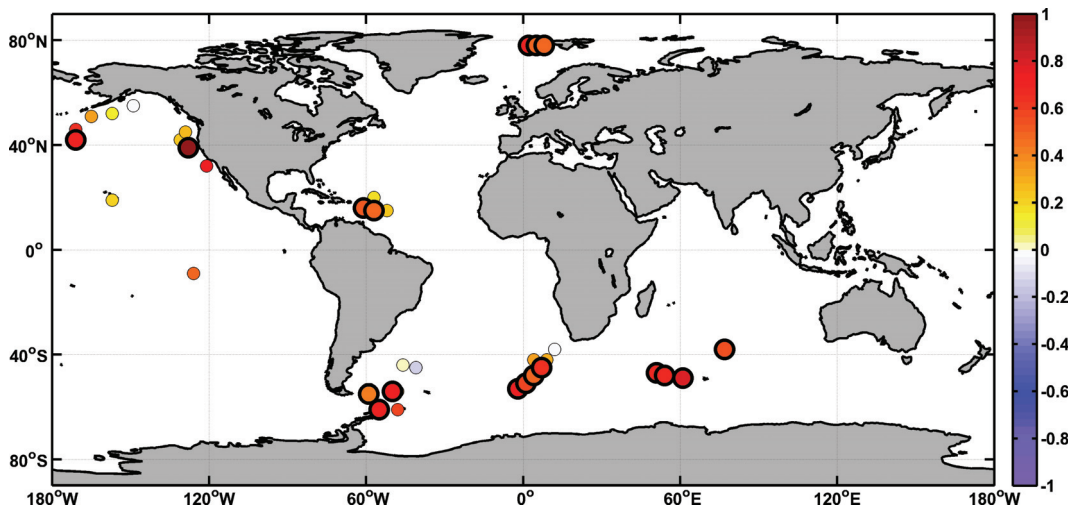


Figure 4.18: Correlation between FESOM OBP anomalies and *in-situ* data on a monthly time scale. Large circles indicate a correlation at a significance level of 95 %

Especially, at high latitudes FESOM OBP anomalies agree well with the observations. Lower correlations are found, as already described, in the North of the AWI ACC array, and at some positions in the MOVE array. Also in the NOAA DART array, correlation is low and not significant. A possible

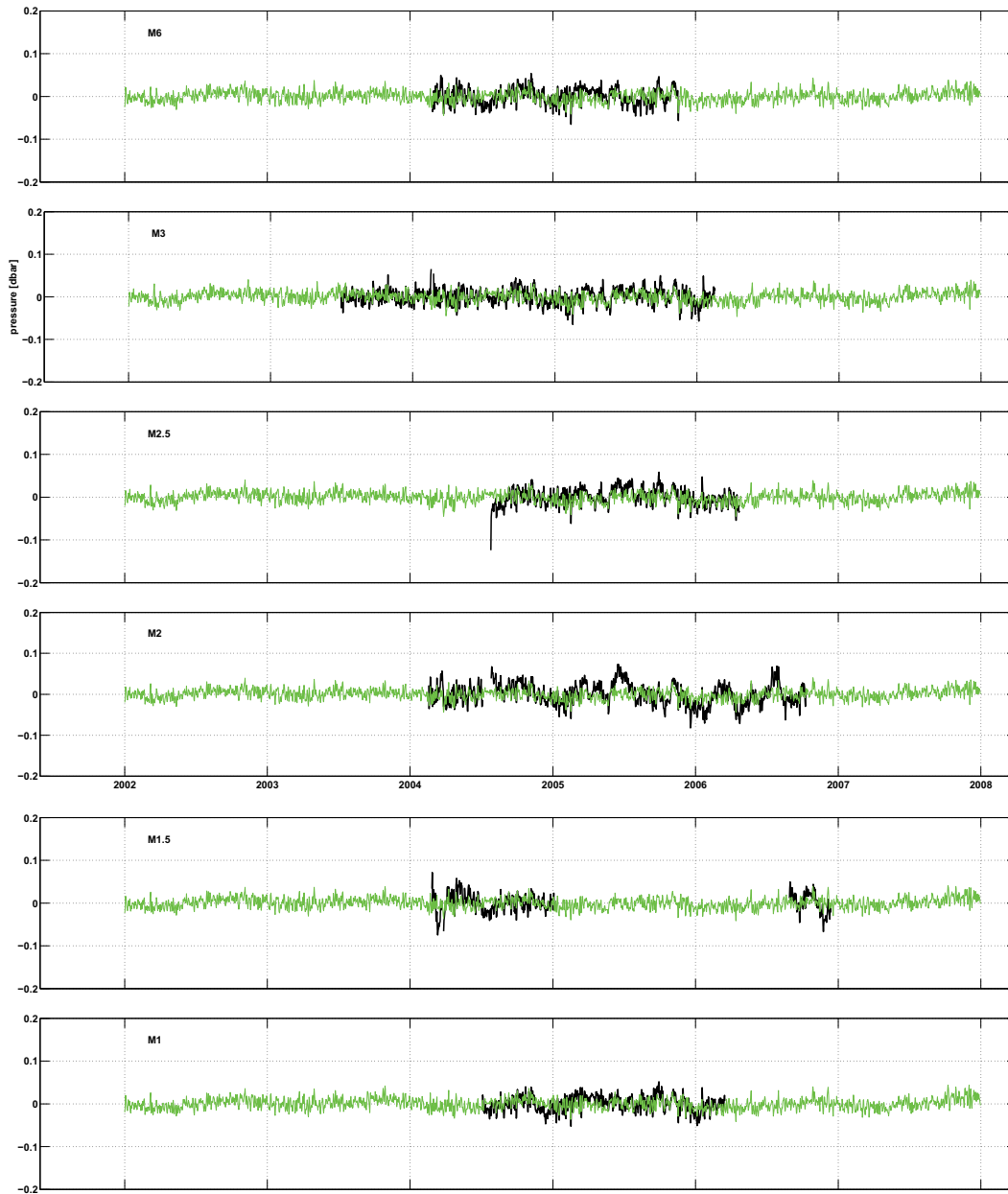


Figure 4.16: Daily mean derived from model simulations and BPR measurements in the MOVE array.

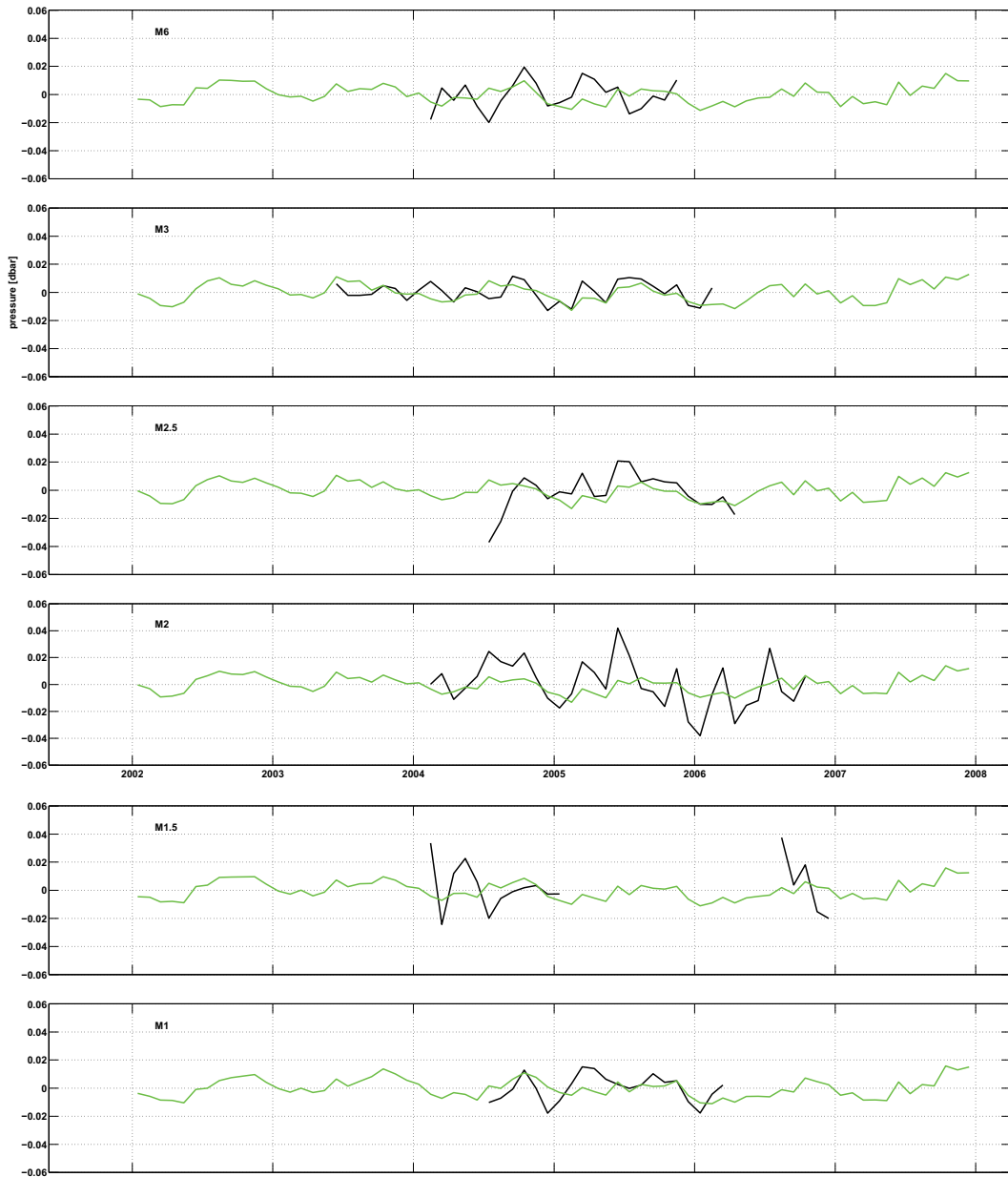


Figure 4.17: Monthly mean OBP anomalies derived from model simulations and BPR measurements.

explanation is that the relatively low correlation is due to the length of the measured time series. Some of the time series from the DART array stored in the OBP database comprise only a few months of data, which limits the significance of a correlation analysis due to the lack of data.

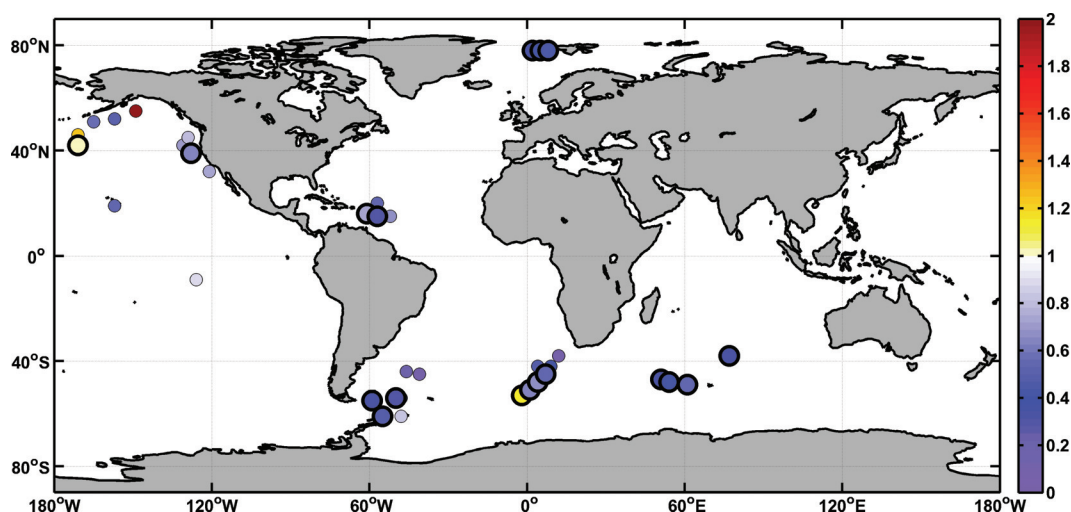


Figure 4.19: Ratio of standard deviation of FESOM OBP anomalies and *in-situ* data on a monthly time scale. Large circles indicate a correlation at a significance level of 95 %

In relation to the observed OBP fluctuations, variability of FESOM simulated OBP anomalies is low. This can be concluded from the ratio of standard deviations of the observations and the simulated OBP at positions where the time series have a significant correlation (Fig. 4.19). The underestimation of the variability is expected as point measurements represent to a certain extent local scale effects which are not captured by the model at 1.5° horizontal resolution.

4.3.1 Conclusions

The validation of FESOM against *in-situ* OBP anomalies shows that FESOM captures a considerable part of the real oceanic variability. Especially, in the high latitude arrays a good agreement between the model and the measurements is found. The standard deviation of the simulated time series is generally smaller than that of the measurements. Subgrid variability influences the BPR measurements which is not resolved by the ocean model at a relatively coarse resolution.

Regional patterns of OBP variability derived from model simulations are found to be related to f/H contours. High variability was detected at high latitudes whereas the variability of the model OBP at low latitudes is much smaller. In order to evaluate the agreement of these findings with observations, a comparison of OBP from two exemplary BPR arrays and simulated OBP in these regions has been performed. At high latitudes, in the AWI ACC array, the daily and monthly OBP variability in the South of the array is well captured by the ocean model whereas the variability observed in the North is not well represented in the model results. This is probably due to small scale effects induced by the Agulhas Rings influencing the BPR measurements in the Cape Basin, but not resolved by the ocean model. The low variability found in the model results in the tropical Atlantic is also observed. Measurements in a BPR array (the MOVE array) north of South America feature a synoptic scale variability of about 0.06 dbar which is small compared to the variability of about 0.1 dbar observed in the ACC array. However, the amplitudes are again slightly underestimated by FESOM. At a monthly time scale the model agrees well with the observations where the annual cycle dominates the measurement, whereas monthly peak-to-peak variations are not well reproduced.

Although, there are deficiencies in capturing small scale variability, the validation of FESOM indicates that the ocean model constitutes a capable tool to reproduce realistic oceanic variability and hence for a comparison to GRACE and the evaluation of GRACE's ability to measure ocean mass redistributions.

Chapter 5

Validation of ocean bottom pressure anomalies derived from gravity field solutions

The gravity field mission GRACE provides estimates of the Earth's time-varying and static gravity field. New measurement techniques first-time utilized for the GRACE mission yield the potential to observe oceanic mass redistribution (represented by ocean bottom pressure anomalies) from space. However, these new methods lead to unprecedented data sets which require a thorough validation.

In this chapter, a validation of the GRACE solutions over the ocean using *in-situ* bottom pressure measurements and model simulations is presented. First, GRACE products provided by the data processing centers are explained in a general way. The key questions regarding GRACE observations are: how are the gravity field solutions derived from the satellite measurements, how can we get ocean bottom pressure anomalies from the gravity field anomalies, and how can the main issues with the data handling be solved?

In-situ and simulated ocean bottom pressure data help to validate GRACE-derived ocean mass fluctuations. The point measurements and simulations provide information on the spatial scales of bottom pressure variability as well as on the temporal evolution of signals. Comparison of these data to GRACE measurements therefore yields a comprehensive assessment of the ability of GRACE to capture oceanic variability on different scales.

5.1 GRACE gravity field solutions

5.1.1 Data collection and processing

Gravity field observations, static and time-varying, have traditionally been obtained by orbit determination of low orbit satellites. The position of a low orbiter can be tracked using the Global Positioning System (GPS). Receiving signals from the geo-stationary GPS constellation allows for a computation of the position with reference to the GPS satellites. Since the position of the satellite is influenced by mass attraction, the orbit parameter yields a description of the gravity field.

One low orbiter, launched in 2000, is the CHALLENGING Minisatellite Payload (CHAMP). It provides observations of the Earth's time-varying and static gravity field. The Gravity Recovery and Climate Experiment (GRACE) is a satellite mission which succeeds the CHAMP mission in the area of Earth gravity field measurements. The new concept of this mission in contrast to CHAMP and previous gravity field observations is the utilization of two satellites following each other on the same orbital track, measuring gravity anomalies by determination of changes in their separation distance. The satellites were launched in 2002 and orbit the Earth with a nominal distance of 220 ± 50 km and in an altitude of approximately 500 km. A K-band microwave interconnection enables the satellites to measure the exact distance between them and its rate of change. To consider precise attitude¹ and non-gravitational forces the satellites are equipped with star cameras and accelerometers. The geo-location and precise timing are measured by using GPS tracking. Non-repeated polar orbits yield a time-varying representation of global mass (re)distribution.

One approach to solve for a global representation of the Earth's gravity field as measured by GRACE is the spherical harmonic solution. This method is well-established in geodesy to give a global description of geophysical fields like the geopotential or the Earth's magnetic field. The GeoForschungszentrum Potsdam (GFZ), the Center for Space Research at the University of Texas (CSR), and the Jet Propulsion Laboratory in Pasadena (JPL) use the spherical harmonic expansion to provide gravity field solutions derived from the pre-processed data.

The GRACE data are divided into products at three stages during the processing, beginning with the raw data received from the satellites, ending with the final gravity field solutions provided in spherical harmonic coefficients.

¹The attitude of a satellite or any rigid body is its orientation in space.

Level-0

The Level-0 data are the result of the data reception, collection and decommutation by the Raw Data Center (RDC) of the Mission Operation System (MOS) in NeustreelitZ (Germany). The raw data are received twice per day at the RDC. The two resulting files are then transferred to the Science Data System (SDS) where the data is extracted and reformatted according to the corresponding instrument like the accelerometer, the star camera etc..

Level-1

Level-1 data are the preprocessed, time-tagged and normal pointed instrument data and are subdivided into two data products: the Level-1A and the Level-1B data. The Level-1A data consist of the calibrated and time-tagged raw data and are not distributed to public. Level-1B include among others the inter-satellite range, range rate, range acceleration, the non-gravitational accelerations from each satellite, the pointing estimates, the orbit etc..

Level-2

Level-2 data are the fully processed 30-day solutions. The product consists of several data types. "Known" fields are provided by numerical models which give an estimate for the different types of mass contribution (ocean, atmosphere, tides etc.) and previously collected data yield an estimate of the geoid over land and ocean. To reduce aliasing effects, the "known" fields are subtracted from the original data during the processing from Level-1B to Level-2 data. Those background models are also provided by the processing centers and are added back for analysis of GRACE data over the ocean.

5.1.2 GRACE products

As already mentioned in the previous section, GRACE data are provided as updates to an *a-priori* best-known geopotential model. The *a-priori* knowledge about the gravity field is derived from numerical models of the ocean and the atmosphere and preceding satellite missions and used to get a first approximation. The estimation of the gravity field with respect to this so-called *background model* yields several advantages. Due to the use of the *a-priori* model as a reference the iterative linearized least-squares approach to the solution of this essentially non-linear problem is better behaved since the linearized updates are small. Furthermore, due to orbital track coverage limitations, rapid variability in the gravity field cannot be well determined

from GRACE data, though, if neglected, it has the potential to corrupt the GRACE estimate through aliasing.

The background gravity model value at time t reads

$$G^*(t) = \bar{G}^* + G'(t - t_0) + \delta G^{st}(t) + \delta G^{ot}(t) + \delta G^{pt}(t) + \delta G^{a+o}(t), \quad (5.1)$$

where \bar{G}^* represents the *a-priori* best-knowledge of the static geopotential, G' the secular variations of the harmonics, δG^{st} , δG^{ot} and δG^{pt} the solid, ocean and pole tides, and δG^{a+o} is a combination of atmospheric and oceanic non-tidal variability.

The gravity field solutions used for the analysis consist of a background model part and the residuals derived from GRACE. The de-aliasing products for oceanic purposes are the GAC/D background model and the GSM GRACE field. The acronyms are defined as follows:

first character		
G	=	geopotential coefficients
second character		
S	=	Estimate made from only GRACE data
A	=	Average of any background model over a time period
third character		
C	=	Combination of non-tidal atmosphere and ocean. Vertically integrated atmosphere on land and vertically integrated atmosphere and ocean elsewhere
D	=	Combination of non-tidal atmosphere and ocean. Atmosphere over land is set to 0. Surface pressure and vertically integrated ocean over the ocean.
M	=	Estimate of the static field.

Table 5.1: Abbreviations for GRACE products used for investigating the solutions over the ocean.

Thus, the GSM product denotes the static gravity field for a respective epoch (i.e. one month) and the GAC/D products the according corrections from non-tidal oceanic and atmospheric background models which are to be added back for a correct representation of oceanic mass variations.

5.1.3 Deriving OBP from GRACE solutions

The GRACE processing centers provide monthly solutions of the time-varying gravity field in the form of spherical harmonic coefficients up to degree and

order 120. For a representation of GRACE-derived OBP, a transformation of the geoid potential to surface mass loading has to be performed. The mapping of the data given in spherical harmonics onto a latitude-longitude grid (θ, Φ) reads:

$$p_G(\theta, \Phi) = \frac{R_e g \rho_e}{3} \sum_{l=1}^{l_{max}} \sum_{m=0}^l \frac{2l+1}{1+k_l} \widetilde{P}_{lm}(\sin(\theta)) \cdot [C_{lm} \cos(m\Phi) + S_{lm} \sin(m\Phi)], \quad (5.2)$$

where R_e is the Earth's mean radius, C_{lm} and S_{lm} are the time dependent components of the GRACE spherical harmonic coefficients of degree l and order m , \widetilde{P}_{lm} are the fully normalized associated Legendre functions, k_l is the load Love number² of degree l , ρ_e is the Earth's average density, and g is the gravitational acceleration. p_G is then the absolute OBP value at point (θ, Φ) derived from GRACE gravity anomalies.

5.1.4 Correction for geocenter motion

The geocenter is defined as the Earth's center of mass. In theory, satellite orbits are depicted in an inertial reference frame whose origin is the geocenter. In this inertial system, the degree 1 spherical harmonic coefficients of the geopotential are zero, which means that the geocenter is fixed. In a reference frame attached to the solid Earth (terrestrial reference frame) defined by the center of figure of the Earth, the geocenter moves about this center due to mass re-distribution, which is then called the *geocenter motion*. The latter reference frame is that of all terrestrial measurement devices (like BPRs and the ocean model in this case). In order to compare satellite to Earth-bound measurements the satellite measurements have to be corrected for this geocenter motion. Not accounting for the geocenter motion would result in GRACE estimates of bottom pressure at locations just above or below the actual ocean floor (varying over the year). Depending on the location this can add up to seasonal variation of 1-2 cm when expressed in equivalent water height.

Data from Satellite Laser Ranging (SLR) and Doppler Orbitography and Radiopositioning Integrated by Satellite (DORIS) can be utilized to obtain estimates of the geocenter motion about the center of figure of the Earth. A world-wide station network of SLR and DORIS stations has been setup and

²Love numbers are measures of how much a planet's surface and interior move in response to the gravitational pull of nearby bodies.

currently consists of around 50 SLR and 50 DORIS stations. The (multi-year) average position of SLR and DORIS station coordinates yields a representation of the center of mass which in first order coincides with the center of figure. The comparison to instantaneous station coordinates (e.g. monthly coordinates) with the mean coordinates provides a measure of the instantaneous geocenter/center of figure vector and of its variation in time which can be adopted as *geocenter motion*.

Estimates of geocenter motions have been derived from different satellite missions. Cretaux et al. (2002), for example, provides annual and semi-annual variations of the geocenter obtained from LAGEOS-1, LAGEOS-2 SLR, TOPEX/POSEIDON SLR and DORIS measurements. The resulting data is given in amplitude and phase which can be re-formulated to a geocenter motion X, Y, Z in meter

$$\begin{pmatrix} X \\ Y \\ Z \end{pmatrix} = \begin{pmatrix} X_{am} \cdot \cos(\omega(t - X_{ph})) \\ Y_{am} \cdot \cos(\omega(t - Y_{ph})) \\ Z_{am} \cdot \cos(\omega(t - Z_{ph})) \end{pmatrix}, \quad (5.3)$$

where X_{am}, Y_{am}, Z_{am} are the amplitudes and X_{ph}, Y_{ph} and Z_{ph} are the phases. Since the annual signal features the dominant amplitude, as a first approximation we use the annual geocenter motion estimates derived from Cretaux et al. (2002) (Tab. 5.2).

	X	σ_x	Y	σ_y	Z	σ_z
Amplitude (mm)	2.6	0.5	2.5	0.1	3.3	1.0
Phase (day of the maximum)	32	7	309	4	36	10

Table 5.2: Amplitude (in mm) and phase (day of maximum signal) of the estimated annual geocenter motion based on Cretaux et al. (2002).

Thus, with (5.3) for every time t ($t=0$ for Jan 1st of each year) one can obtain an estimate for the geocenter motion using the values from Tab. 5.2.

Now, the relative deflection X, Y, Z of the geocenter with respect to the center of figure can be related to the fully normalized (as provided by GRACE) degree 1 potential coefficients by

$$\begin{pmatrix} C_{11} \\ S_{11} \\ C_{10} \end{pmatrix} = \frac{1}{\sqrt{3} \cdot R_e} \begin{pmatrix} X \\ Y \\ Z \end{pmatrix}, \quad (5.4)$$

where the Earth's radius R_e is also expressed in meters ($6.378 \cdot 10^6$ m).

For the correction the coefficients are added to the GRACE sets of spherical harmonics. With this additional set of degree 1 coefficients we are now able to derive the complete surface mass loading which is comparable to the Earth-bound measurements as bottom pressure measurements and simulated OBP.

5.1.5 Detection of OBP signals in GRACE solutions

In the open ocean, the different accuracies and spatial scales of satellite data and point measurements complicate comparisons between these two datasets of OBP. While GRACE estimates are representative for phenomena with a horizontal scale of several hundreds of km, *in-situ* OBP measurements are pointwise by nature. Furthermore, spurious meridional patterns due to aliasing (Seo et al. (2008)) are evident in many GRACE satellite products (Fig. 5.1). Therefore, the application of an adequate filter is necessary to allow for a comparison to *in-situ* OBP data.

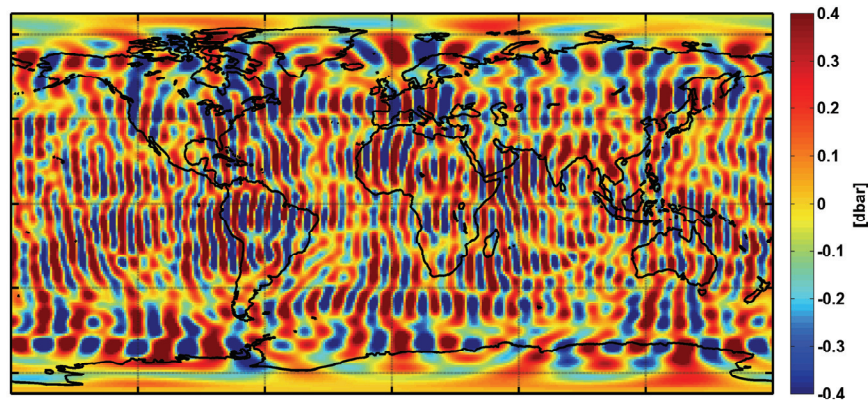


Figure 5.1: Typical GRACE-derived monthly OBP anomaly (GFZ RL04, GSM+GAD, d/o 1-50, Sept. 2003).

An obvious filter approach is the application of a two dimensional Gauss function with a carefully chosen radius (Wahr et al. (1998)). As can be seen in Figure 5.2 the striping artifacts are reduced in the Gauss filtered solution and geophysical phenomena can be detected. The land signal is dominated by the hydrological cycle in river basins (Ramillien et al. (2004)) and snow

accumulation in high latitudes (Frappart et al. (2006)), the ocean signal, by the redistribution of water due to circulation variability and the seasonal cycles of river runoff and net evaporation. Retrieval of the small amplitudes of mass variations in the ocean, compared to the large hydrological signals over land, requires a sophisticated filtering of GRACE data.

However, due to the indiscriminative nature of the Gauss function, this method mixes land and ocean signals near the coasts. Furthermore, ocean circulation and thus OBP variations are strongly affected by bottom topography. Negative and positive OBP anomalies are often separated by topographic features like submarine ridges. An isotropic filter like the Gauss filter is bound to mix the signals of such a dipole.

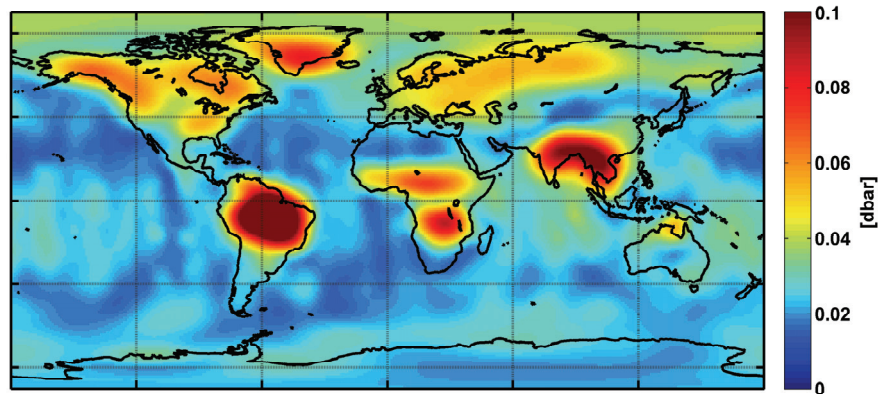


Figure 5.2: RMS monthly variability of OBP derived from a GRACE solution filtered with a 750 km Gauss filter (GFZ RL04, GSM+GAD, d/o 1-50).

Swenson and Wahr (2006) developed a filtering mechanism which is based on the removal of correlated errors in the GRACE spherical harmonic solutions. Chambers (2006) improved this technique to study gravity variations over the ocean using an empirical approach to obtain an optimized set of parameters. This kind of filtering gives reasonable results on a global and ocean basin scale (Ponte et al. (2007)), but also introduces the risk of attenuation of signals³.

Using an equivalent Gauss filter radius of about 800 km, Rietbroek et al. (2006) found a strong correlation between GRACE anomalies and OBP mea-

³An analysis of solutions derived with this kind of filtering follows in section 5.3.

measurements in the Kerguelen and Crozet region. Their success already indicates that signals from an ocean bottom pressure recorder (BPR) represent large-scale ocean variability in this area. Thus, we expect OBP anomalies to be coherent over an area larger than the immediate vicinity of a BPR.

The following section presents a newly developed GRACE data filtering algorithm which is based on the determination of an area of coherent signals around any given point. We will demonstrate that these patterns vary in size and can have a rather complex structure which partly follows bottom topography. For this purpose, we use results from a Finite Element coupled Sea ice–Ocean Model (FESOM; Timmermann et al. (2009)).

5.2 A new filter algorithm for GRACE data

5.2.1 Coherence patterns of OBP variability

For this study the traditional FESOM implementation has been modified to give a proper representation of ocean mass fluctuations (described in chapter 3). Validation of the modeled OBP anomalies against *in-situ* measurements indicates that the model captures a large part of real oceanic variability. The model agrees well with the *in-situ* data, especially at locations where measurements tend to represent larger scale effects and are less influenced by small scale variability.

FESOM simulations indicate that on a monthly time scale OBP anomalies are coherent over large areas of complex geometry. A new filtering method for GRACE-derived ocean mass anomalies is obtained by applying these coherence patterns on a regular grid.

We use FESOM simulations to identify the patterns of coherent OBP variability. To eliminate the seasonal cycle (which yields the dominant signal but on a much larger, hemispheric scale), a five months high-pass filter has been applied to the anomalies. From the resulting dataset p'_F , we determine areas of high coherency by calculating the cross-correlation between the time series at fixed positions (positions of bottom pressure recorders for the validation against *in-situ* measurements, model grid points for the global analysis) and time series at all points of the model domain within a 20° radius. The correlation between an anomaly at a position \vec{x}_0 and one at a position \vec{x} is defined as

$$r(\vec{x}, \vec{x}_0) = \frac{E(p'_F(\vec{x}) \cdot p'_F(\vec{x}_0))}{\sigma_{p'_F(\vec{x}_0)} \cdot \sigma_{p'_F(\vec{x})}}, \quad (5.5)$$

where the p'_F are the high-pass filtered FESOM OBP anomalies, E is the expected value and σ is the standard deviation. The pattern of high coherency ("coherence pattern") is then defined as the area with correlations larger than 0.7. It turns out that OBP anomalies on a time scale of 1-5 months are spatially coherent over large areas which are strongly related to bottom topography. For a BPR position close to Amsterdam Island for example, we find a coherence pattern with a diameter of approximately 1500 km, for a position in the NOAA/DART Array we find a pattern diameter of approximately 1000 km (Fig. 5.3).

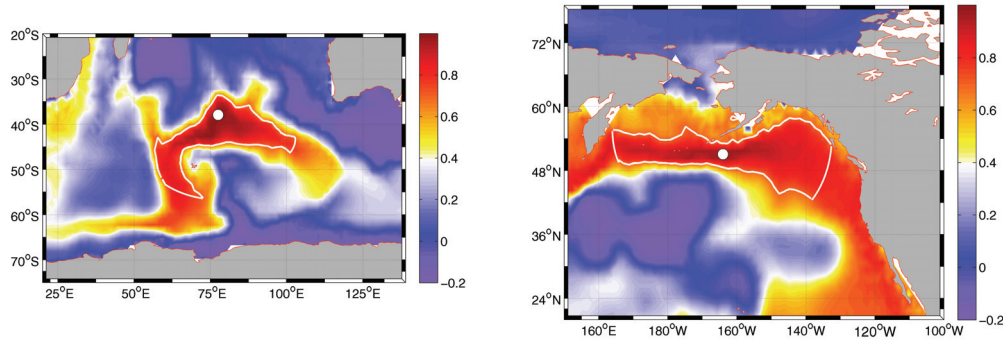


Figure 5.3: Two examples of model-derived patterns of high spatial coherency ("coherence patterns"), defined by the areas with correlations larger than 0.7 inside a circle with 20° radius. Examples refer to the BPRs close to Amsterdam Island (left) and the NOAA Dart Array (right). White circles indicate the reference points (BPR positions), white lines the cut-off edge.

OBP measurements at these positions are representative for the areas defined by the coherence patterns. We use these coherence patterns to filter the GRACE data by weighting the data for each position inside the 20° circle with the pre-computed correlation coefficient. The weighting function r^* is defined with a cut-off at a correlation of 0.7 as

$$r^*(\vec{x}, \vec{x}_0) = \begin{cases} r(\vec{x}, \vec{x}_0) & \text{for } r(\vec{x}, \vec{x}_0) \geq 0.7 \\ 0 & \text{for } r(\vec{x}, \vec{x}_0) < 0.7 \end{cases} \quad (5.6)$$

In order to generate a smooth transition in areas where the maximum distance criterion holds and the correlation is still above 0.7, a monotonically decreasing cut-off function centered at a distance of 18° is additionally applied:

$$\zeta(\vec{x}, \vec{x}_0) = \frac{1 - \tanh\left(\frac{\Delta - 18^\circ}{2^\circ}\right)}{2}, \quad (5.7)$$

where Δ is the distance [in degrees] between \vec{x} and \vec{x}_0 . The filtered GRACE solution p_G^* is then calculated by

$$p_G^*(\vec{x}_0) = \frac{\int_C p'_G(\vec{x}) \cdot r^*(\vec{x}, \vec{x}_0) \cdot \zeta(\vec{x}, \vec{x}_0) dA}{\int_C r^*(\vec{x}, \vec{x}_0) \cdot \zeta(\vec{x}, \vec{x}_0) dA} \quad (5.8)$$

where C is a circle with a radius of 20° around \vec{x}_0 . The result for every \vec{x}_0 is a time series that is comparable to the point measurement of an OBP recorder. By applying this procedure to every point of a $1.5^\circ \times 1.5^\circ$ grid, we obtain global maps of GRACE-derived mass anomalies.

5.2.2 Improvement of GRACE solutions due to pattern filtering

As a reference dataset, we use GRACE data (GFZ RL04, d/o 1-50) that have been smoothed with a 750 km Gauss filter (Fig. 5.2). The radius has been determined from studies in which OBP anomalies derived from GRACE data were filtered with different Gauss radii and then compared to in situ data. It was found that a radius of 750 km yields the best results.

Even with the optimized radius, a comparison with BPR data reveals that OBP anomalies derived from the GRACE solutions and filtered with a Gauss filter fail to reproduce the characteristic extremes of the in situ time series in many cases. Data filtered with the coherence pattern method feature a better agreement. The course of minima and maxima is captured rather well, and the amplitude is close to the observations. Two typical examples are shown in Fig. 5.4.

Close to Amsterdam Island (Fig. 5.4, left panel), the Gauss-filtered solution fails to reproduce the observations in amplitude and phase. The course of minima and maxima is much better captured in the pattern-filtered time series. Gauss-filtering in the NOAA Dart Array causes a slight underestimation of the amplitude for most of the time (Fig. 5.4, right panel). The characteristic extremes are not well captured. The pattern-filtered solution features a higher amplitude and reproduces a larger part of the observed variability. Correlations between GRACE and in situ time series increase from -0.01 to 0.4 for the Amsterdam Island position and from 0.02 to 0.32 for the BPR in the NOAA Dart Array. For both positions, the correlation is only significant (at a level of at least 85 %) when the pattern filter is applied.

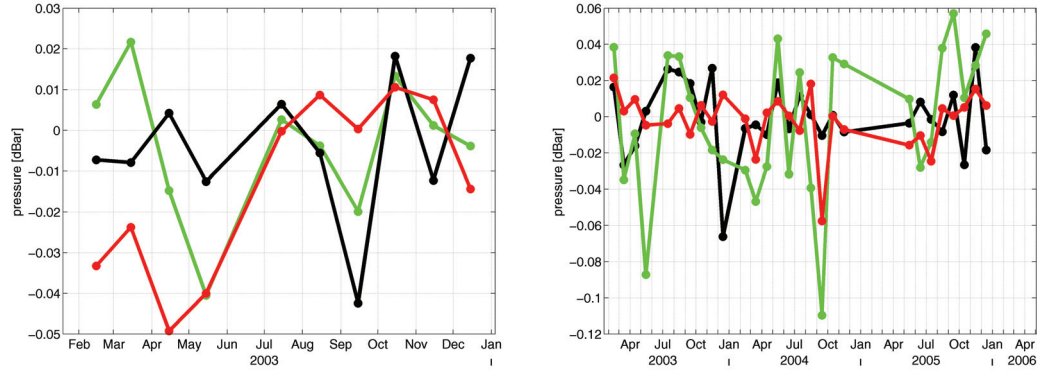


Figure 5.4: Time series of OBP anomalies at $77.58^{\circ}E$, $37.9^{\circ}S$ (CNES, Amsterdam Island) and $164^{\circ}W$, $51.07^{\circ}N$ (NOAA DART Array). Black line indicates in situ observations, red line the Gauss-filtered GFZ RL04, green line pattern-filtered GFZ RL04.

Applying the pattern-filtering algorithm to GRACE GFZ RL04 monthly solutions for other BPR positions all over the globe yields an improved correlation with *in-situ* OBP time series in comparison to the Gauss filtered data in many cases (Fig. 5.5).

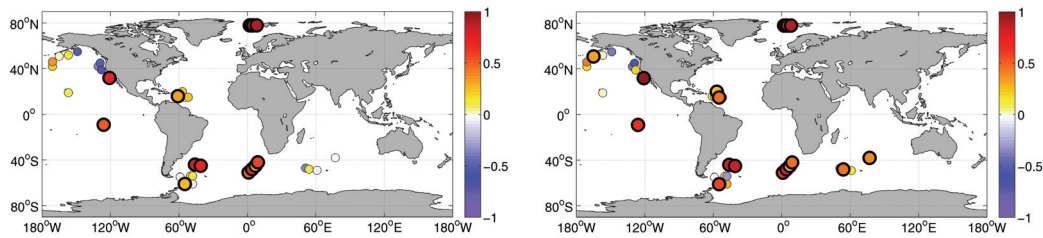


Figure 5.5: Correlations between *in-situ* and GRACE-derived OBP anomalies. Left: Gauss-filtered GRACE data. Right: Pattern-filtered GRACE data. Large circles indicate a correlation that is significant at an 85 % level.

Especially in the Crozet/Kerguelen/Amsterdam Islands region and in the southwestern and tropical Atlantic (POL ACCLAIM, CNES and IfM MOVE Arrays) the agreement between GRACE and *in-situ* measurements is enhanced. The correlation increases by 0.1-0.2 at these locations, and even switches from a correlation close to zero to a significant positive correlation

in the Crozet/Kerguelen/Amsterdam Islands region. Applying a Gauss filter to the GRGS solution, Rietbroek et al. (2006) found an even higher correlation in the Crozet/Kerguelen region; however, a comparison to other BPRs shows that the agreement strongly varies with location and is weaker than for the GFZ solution in other places. For 18 positions, the correlation between pattern-filtered GFZ data and *in situ* measurements is significant at the 85 % level; for 7 of them the correlation is significant even at the 95 % level. Compared to the Gauss-filtered data with only 14 (3) positions significant at the 85 % (95 %) level, the improvement is obvious.

Global maps of root-mean-square (RMS) monthly variability of the GRACE solutions filtered with a 750 km Gauss filter (Fig. 5.6, left) show a high variability in and adjacent to the seasonally ice-covered areas. The ocean signal in coastal regions is highly influenced by the large hydrologic cycle over land due to the indiscriminate nature of the Gauss filter; the signature of land leakage effects is evident. In low and mid latitudes the signals are very smooth, but spurious meridional patterns are still visible. Due to the smoothness of the variability patterns it is difficult to identify circulation patterns or other oceanographic signals correlated to OBP anomalies.

Monthly RMS variability derived from pattern-filtered solutions (Fig. 5.6, right) shows a similar structure with high variability in the high latitudes. However, the an-isotropy of the pattern-filtering does not smooth out local gradients and features on a much smaller scale can be clearly identified. Specifically, most of the currents with high variability, as for example the Zapiola Eddy (a quasi-barotropic anticyclonic eddy centered at $45^{\circ}S$ $42^{\circ}W$ east of South America) and the Agulhas Return Current, are well pronounced. The clear representation and sharp boundaries of these features and the reduced variability along the coast indicate a good reduction of land leakage effects. This is particularly well visible close to Amazon Basin.

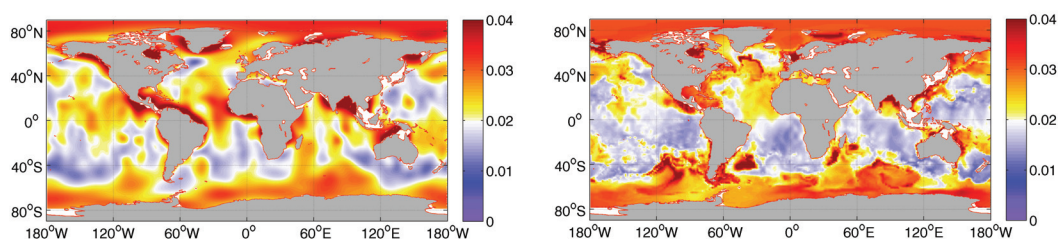


Figure 5.6: RMS monthly variability of GRACE GFZ RL04. Left: Gauss-filtered with 750 km radius. Right: Using the newly developed pattern-filtering algorithm.

Averaging the filtered data over the entire global ocean yields a seasonal cycle with a maximum in Sept./Oct. and a minimum in April, which is very similar in the two datasets (Fig. 5.7).

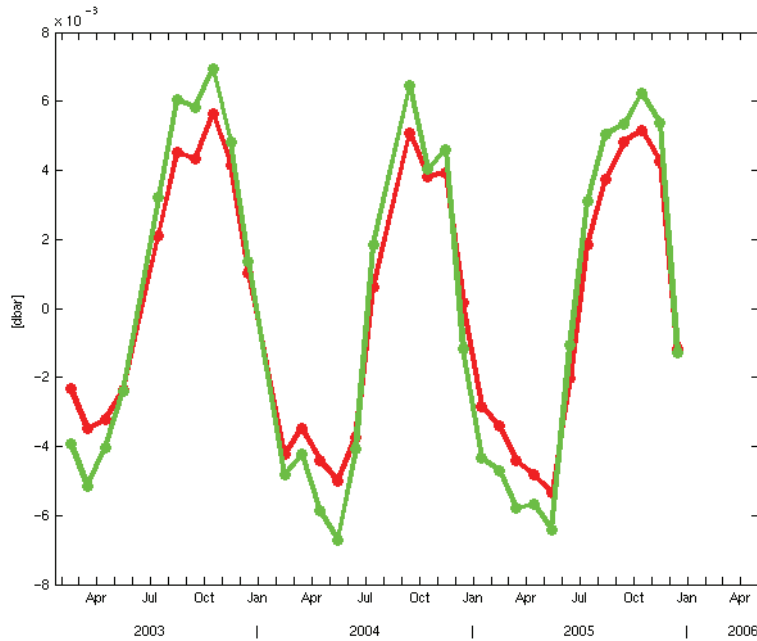


Figure 5.7: Global mean OBP anomalies derived from GFZ RL04 solutions with a 750 km Gauss filter (red) and the coherence-pattern filter (green).

While an amplitude of less than 0.5 cm equivalent water column height is found in the Gauss-filtered data, the pattern-filtered data feature an amplitude of about 0.7 cm, which agrees well with results from Lombard et al. (2007).

An analysis of the damping effects shows that the biases of the pattern filter and the Gaussian filter are of the same order of magnitude. Additional spectral filtering of the spherical harmonic coefficients reduces the noise but yields anomalies which still have a ten times higher amplitude than the *in-situ* data. When, in the second step, the pattern filter is applied, damping varies with regions due the different shapes of the patterns. On average, damping introduced by the pattern filtering matches that of a Gauss filter with a radius of 750 km. The data derived through pattern filtering reproduce the amplitude and phase of the *in-situ* data better than the Gauss-filtered data.

5.3 De-striped GRACE solutions

The de-striping algorithm introduced by Swenson and Wahr (2006) and specialized by Chambers (2006) for the evaluation of GRACE derived OBP anomalies is based on correlated errors in the spherical harmonic solutions. The typical elongated stripes in the GRACE solutions (Fig. 5.1) are found to be correlated for degree and order > 8 . The basic idea of de-striping is to fit higher degree polynomials to the spherical harmonics. Subtracting the fitted polynomial leads to a reduction of the striping artifacts. However, this empirical method which relies on the assumption that the suggested polynomial describes error-only contributions can lead to an attenuation of signals.

De-striped solutions are provided on the GRACE Tellus website⁴ at three different horizontal resolutions. Since de-striping reduces the north-south elongated patterns associated with errors but still leaves artifacts in the solutions, the de-striped fields are additionally filtered with a 300 km, 500 km or 750 km Gauss filter⁵.

Removal of the correlated errors leads to a good representation of the OBP anomalies in the GRACE data when compared with the *in situ* data (Fig. 5.8). Similar to the pattern-filtered only data (see Fig. 5.5), the *in-situ* OBP anomalies observed at high latitudes are well captured by the de-striped solutions. We get even more significant correlations at some positions (Fig. 5.8). The solutions filtered with three filter radii feature similar high or low correlation to the *in-situ* data in the different arrays. However, the number of significant correlations to the *in-situ* are highest in the 500 km in comparison to the solution filtered with the 300 km and 750 km radius Gauss filter.

The main differences of the three solutions are detected in the standard deviation compared to the *in-situ* data. Obviously, a large Gauss radius reduces the variability in the GRACE data. In Figure 5.9 a high overestimation of the amplitudes of the *in-situ* measurements especially in the NOAA DART array and in the MOVE array can be detected, which reduces with application of a larger Gauss radius. The variability observed in the *in-situ* data in the Framstrait is already slightly underestimated in the 300 km solution, though.

Even with an optional choice though, the isotropic structure of the Gauss filter may still lead to an insufficient representation of the OBP anomalies. In order to further improve the de-striped solutions, we applied the pattern filter also to the de-striped data. To avoid spurious damping we chose the

⁴Data are available at <http://grace.jpl.nasa.gov/data/mass/>.

⁵In the following we evaluate the effect of the different filter radii based on the GFZ RL04 solution, since this effect is found to be consistent for the three data products from GFZ, JPL, and CSR.

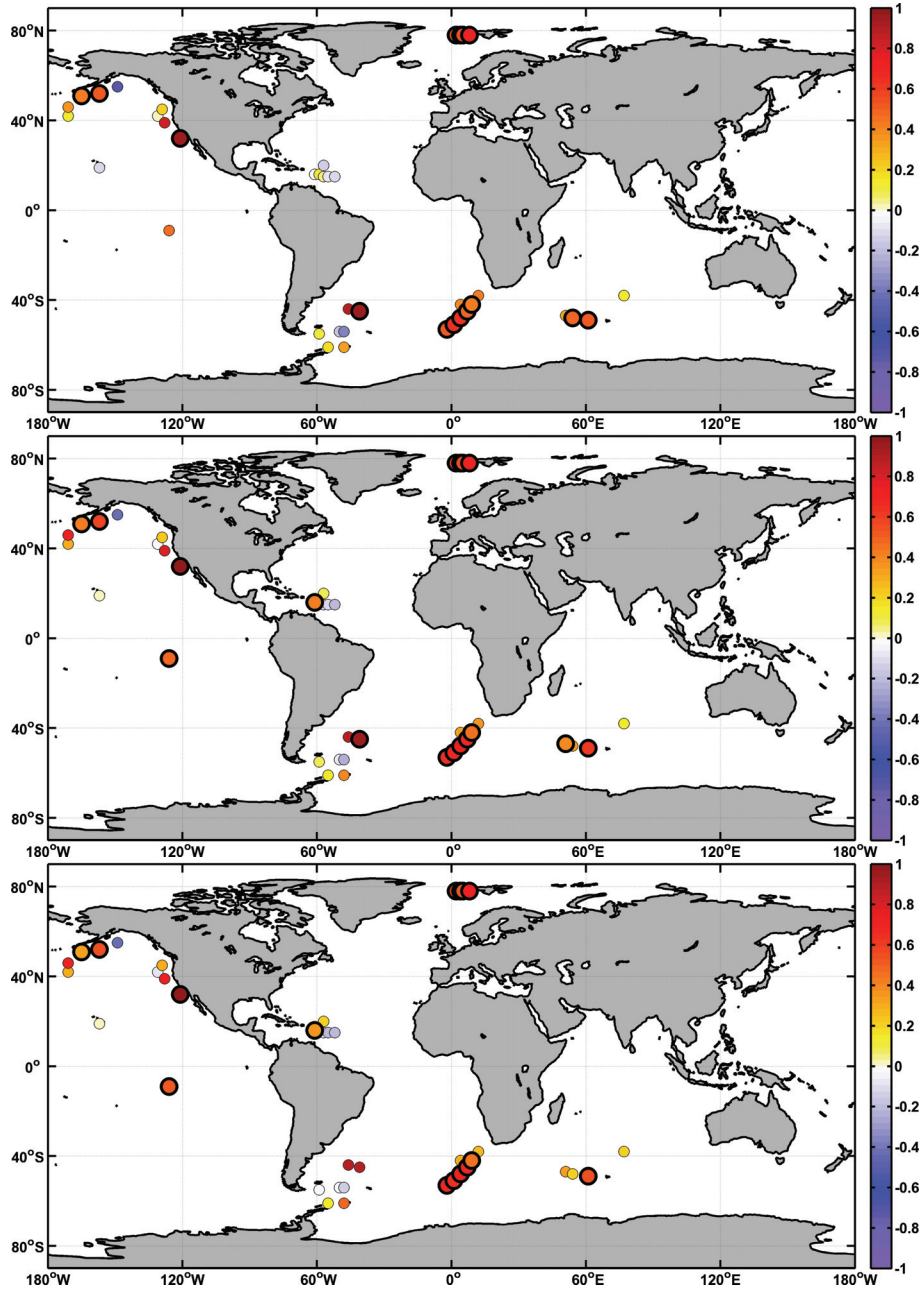


Figure 5.8: *In-situ*/GRACE comparison. Correlation between the de-striped GRACE solutions (derived from GFZ RL04) and the *in-situ* data (from top to bottom: 300 km, 500 km, and 750 km Gauss filtered). Large circles indicate a correlation significant at a 95 % level.

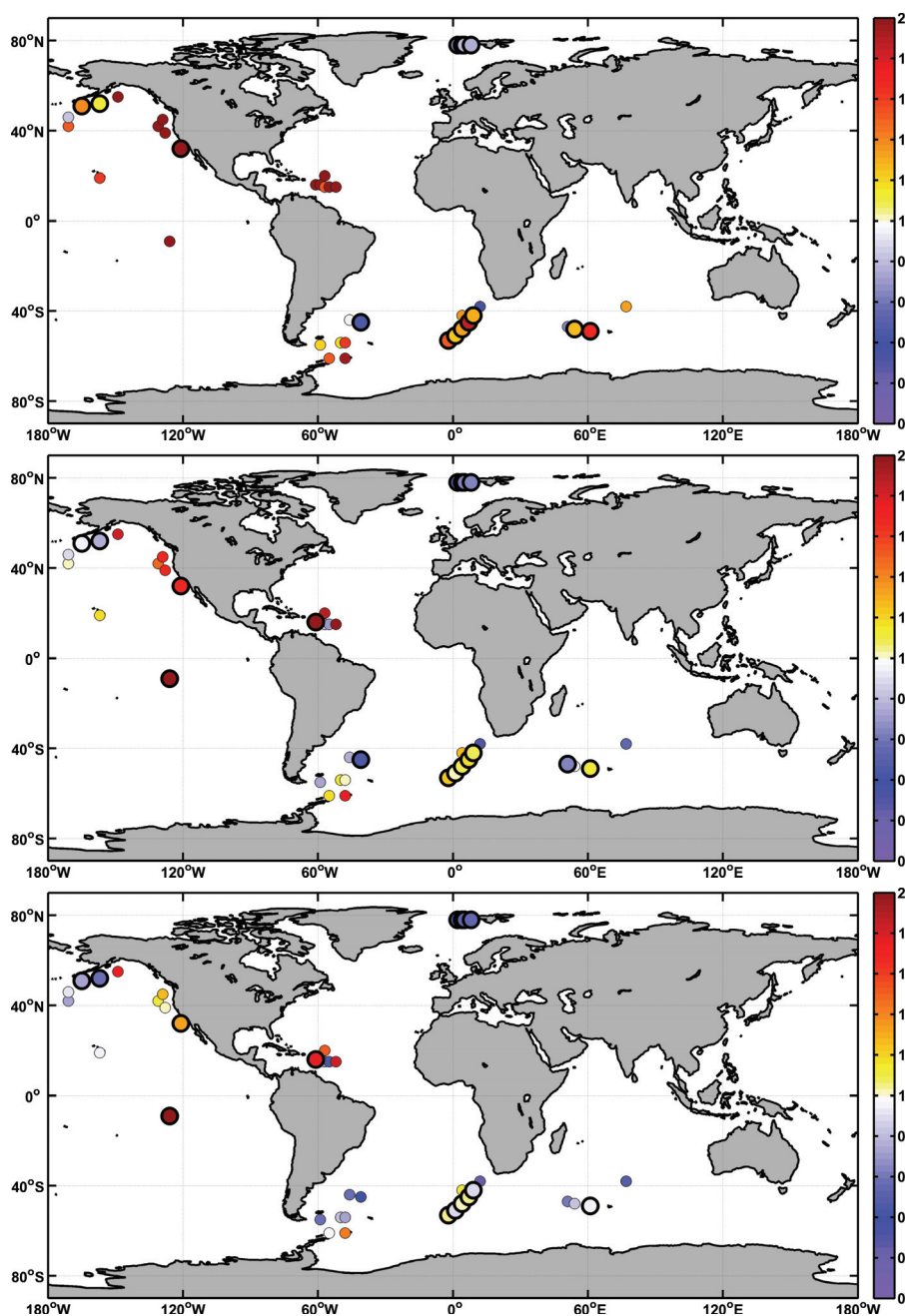


Figure 5.9: Ratio between the standard deviation of the *in-situ* measurements and GRACE-derived OBP (GFZ RL04, de-striped). Blue indicates a higher standard deviation of the *in-situ* measurements than GRACE, red the opposite. (from top to bottom: 300 km, 500 km, and 750 km solutions.) Large circles indicate a correlation at a 95 % significance level.

de-stripped solutions with a small equivalent Gauss filter radius (300 km).

The application of the pattern filter slightly improves the correlations to the *in-situ* data even for the de-stripped GRACE solutions (Fig. 5.10). The variability in the pattern-filtered solutions is comparable to the 500 km-750 km solutions (Fig. 5.11).

The solutions from the three processing centers show mainly similar correlations to the *in-situ* data. The deficiencies already found in the 750 km Gauss filtered and pattern-filtered solution (Section 5.2.2) still remain in the tropical Atlantic whereas the JPL product indicates the lowest correlations in this region. Also the measurements in the Framstrait are not as well captured as in the GFZ and CSR solution.

These disagreements are also reflected in the standard deviation found in the GRACE products in the respective regions. In the tropical Atlantic GRACE consistently, i.e. in all data products, overestimates the variability seen in the *in-situ* measurements. Especially, the JPL solution features too much variability in this region. Probable causes for this overestimation will be illustrated in the following Section.

5.4 Global and regional validation

In order to assess the ability to capture ocean bottom pressure variability the validation of GRACE has been expanded to regional and global scales. For the regional validation we derived a skill which describes the ability of GRACE to detect OBP anomalies in the different BPR arrays and is based on the correlation in the arrays. This validation has also been performed for the simulated OBP anomalies. The results enable us to evaluate the regions where the model performs better, equal or worse than GRACE.

5.4.1 Regional validation

We defined 6 regions according to the positions of the BPR arrays for the regional evaluation of the ability of GRACE to measure OBP variability. 4 of the 6 arrays are situated at high latitudes: the ACC array south of Africa and the PIES array in the Framstrait, set up and maintained by the AWI, the array in Drake Passage, consisting of various deployments of the POL, and the BPRs in the Kerguelen region. The NOAA DART array in the Northern Pacific consists of BPRs primarily used for tsunami warning. Therefore it is situated along the coast of North America at mid latitudes. In the low latitudes the MOVE array in the tropical Atlantic provides OBP measurements.

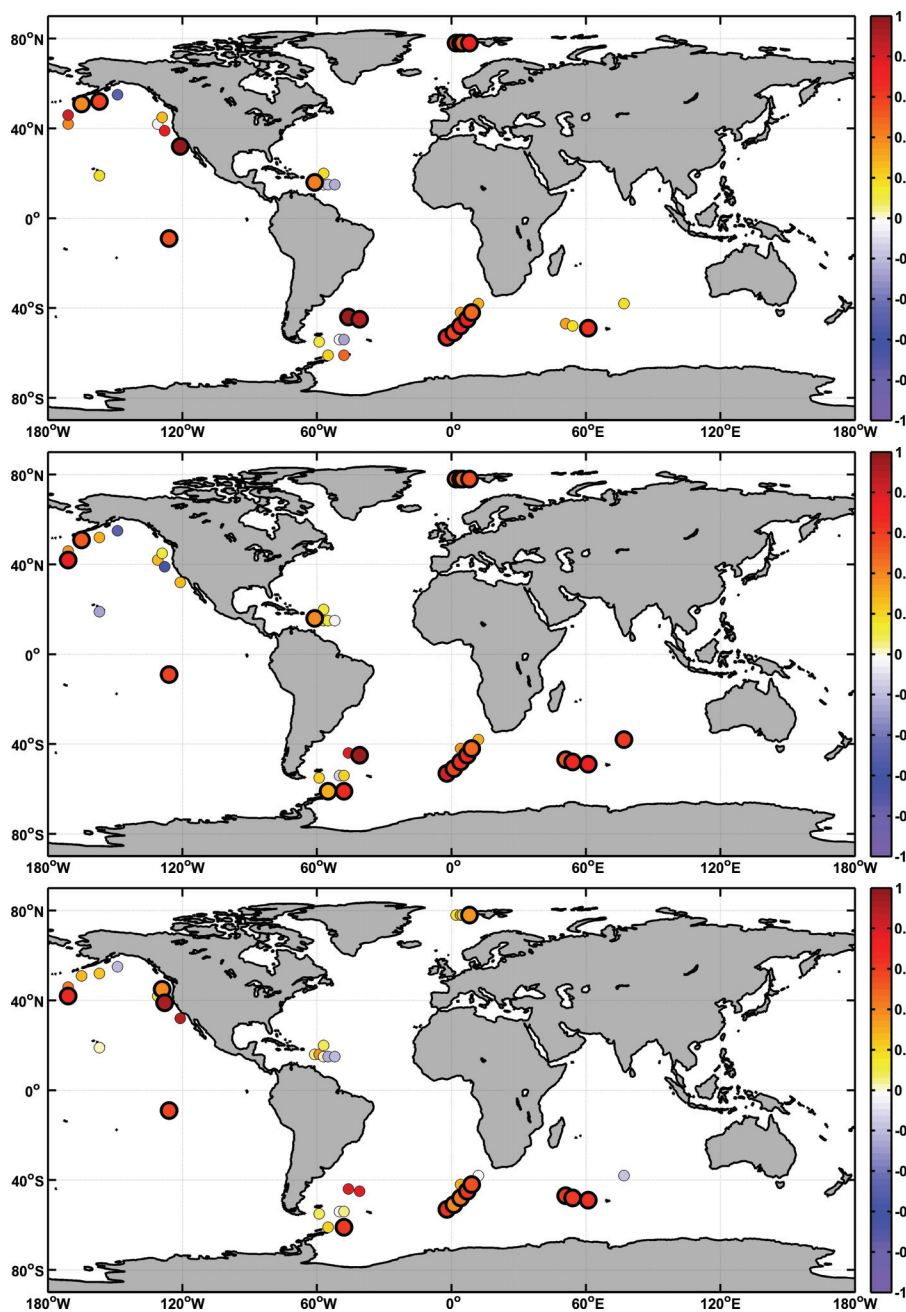


Figure 5.10: *In-situ*/GRACE comparison. Correlation between the 300 km-dstriped and additionally pattern-filtered solutions. Upper panel: GFZ RL04, mid panel: CSR RL04, lower panel: JPL RL04.1. Large circles indicate a correlation significant at a 95 % level.

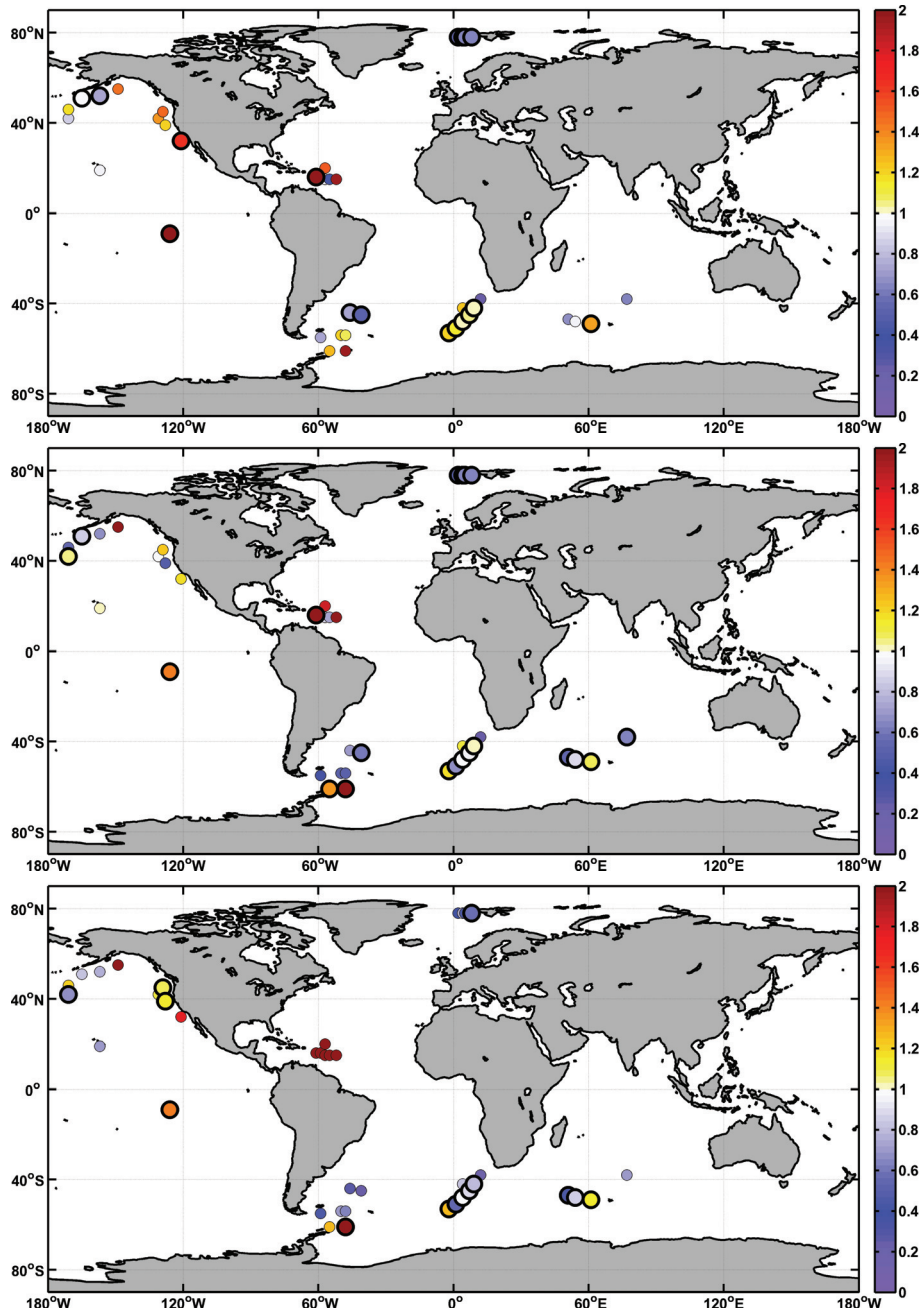


Figure 5.11: Ratio between the standard deviation of the *in-situ* measurements and GRACE-derived OBP (300 km de-striped and pattern filtered). Blue indicates a higher standard deviation of the *in-situ* measurements than GRACE, red the opposite. (from top to bottom: GFZ RL04, CSR RL04, JPL RL04.1) Large circles indicate a correlation at a 95 % significance level.

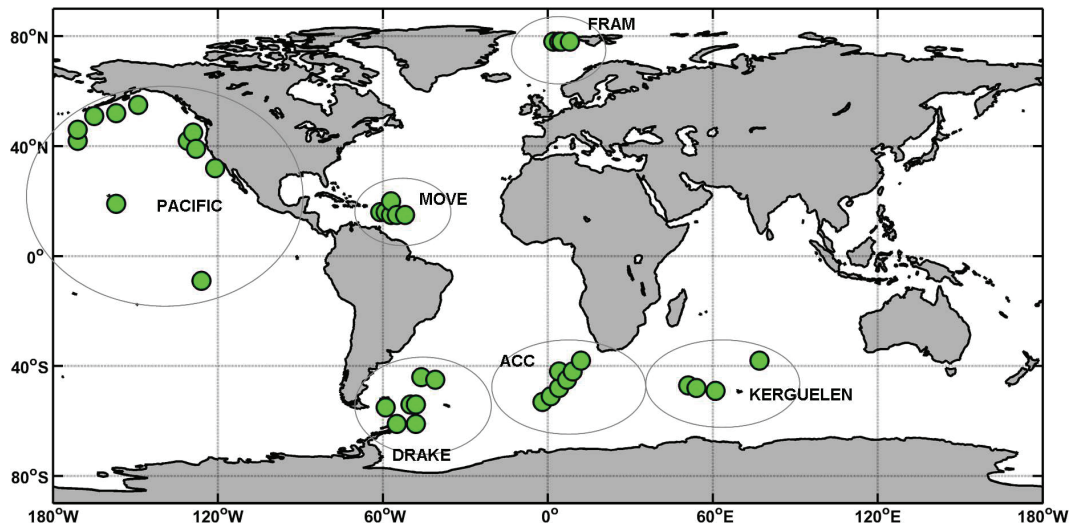


Figure 5.12: Positions of the BPRs and definition of arrays.

The relation between GRACE-derived OBP and *in-situ* measurements can be described with the correlation between those two kinds of measurements. The correlation indicates to what extent the time series are linearly connected. Testing the correlation against coincidence, i.e. testing the null hypothesis that the correlation between the time series is 0, leads to a so-called *p-value*. The p-value is the probability that the null hypothesis was rejected although it was true. Therefore, the p-value being small indicates that the correlation is significantly non-zero.

Relying on this connection between correlation and p-value, we define a skill for assessing the quality of GRACE measurements in the different regions. For each BPR i and each region A the skill s_A reads:

$$s_A = \frac{1}{|A|} \sum_{i \in A} (1 - p_i) \cdot r_i \quad (5.9)$$

where r_i is the correlation between GRACE-derived and *in-situ* OBP and p_i the according p-value. Hence, s_A ranges between -1 and 1 and combines the relevance of the correlations in each array to one number.

Table 5.3 indicates that generally highest correlations are obtained in the high latitude arrays. GRACE as well as FESOM OBP anomalies feature a higher agreement with the *in-situ* data for example in the Framstrait or ACC AWI array. At low latitudes like in the MOVE array correlations are weaker. Correlations between the de-stripped and pattern-filtered solutions and the *in-situ* observations are generally slightly higher than correlation to

	CSR	GFZ	JPL	FESOM
ACC AWI	0.52/0.52	0.49/0.49	0.39/0.4	0.42
DRAKE	0.33/0.39	0.28/0.32	0.18/0.28	0.34
MOVE	0.1/0.1	0.09/0.08	0.005/0.008	0.24
KERGUELEN	0.58/0.63	0.26/0.26	0.42/0.42	0.64
FRAM	0.53/0.55	0.65/0.66	0.12/0.16	0.56
PACIFIC	0.09/0.18	0.33/0.37	0.31/0.36	0.41

Table 5.3: Skill calculated for the BPR arrays. First number denotes the skill derived from the 500 km de-striped solution, second from the 300 km de-striped, pattern-filtered GRACE solutions. FESOM solution remained unfiltered.

the 500 km de-striped only.

The CSR and GFZ solution show the highest correlations for most of the arrays, whereas the anomalies derived from the JPL solution indicate a lower agreement to the *in-situ* data. Especially in the Framstrait array and also the MOVE array in the tropical Atlantic correlations are much lower.

FESOM simulations feature a similar agreement with the *in-situ* data in the different array as the GFZ and CSR solution. Correlations are higher in the MOVE array and the Kerguelen array from CNES.

5.4.2 Basin and global scale

For a basin-scale comparison we divided the global ocean into five basins: the Atlantic, the Indic, the Pacific, the Southern Ocean, and the Arctic Ocean (Fig. 5.13). The subdivision into the different basins differs from the official definition of the ocean basins, but is useful for this study, since it separates main circulation patterns like for example the Antarctic Circumpolar Current (ACC) from other circulation regimes.

Figure 5.14 shows the OBP anomalies derived from GRACE solutions⁶ and FESOM simulation averaged over the 5 basins as well as the global average. The three products from JPL, CSR, and GFZ show very similar results for all basins and as a consequence for the global average. The largest discrepancies between the GRACE solutions can be detected in the Atlantic and the Arctic Ocean.

⁶Based on the successful application of the pattern-filtering on the de-striped solutions as validated in the previous section, in the following the 300 km de-striped and additionally pattern-filtered GRACE solutions are considered.

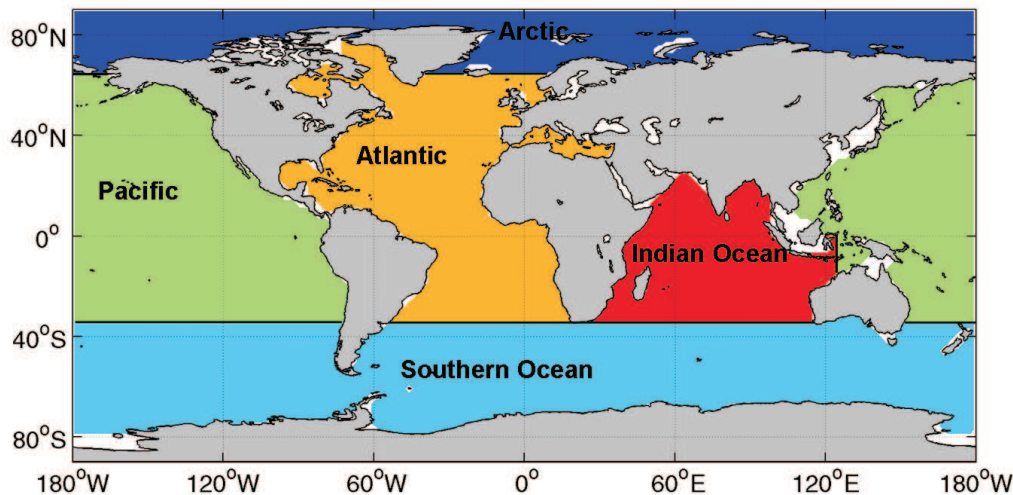


Figure 5.13: Map of subdivision of the global ocean into basins.

In the Arctic the anomalies derived from the CSR (green line) and GFZ (red line) solution mainly vary in phase, whereas the JPL (blue line) product differs from both. The largest differences occur in the middle of 2003 and the end of 2006 where the GFZ and CSR anomalies feature a maximum which is not visible in the JPL solution.

In the Atlantic the month-to-month variations mainly coincide between the three products, but the amplitudes of the anomalies differ slightly. In the late 2004 the JPL and GFZ solution feature a similar course of the time series whereas the CSR product resembles FESOM by showing a maximum in this period.

The best agreement with the model simulation is obtained in the Pacific, Indic and Southern Oceans. In the Atlantic and the Arctic, where also the three GRACE products differ the most, FESOM shows fluctuations different from GRACE. Anomalies in the Arctic and also the month-to-month variability are smaller in the model simulation. This may be referred to mass effects not captured by the model, like the changing Greenland ice sheet mass (see also Fig. 5.16).

In the Atlantic basin, the annual cycle detected in the GRACE solutions features a different month-to-month variability than the model. This disagreement between FESOM and GRACE is probably induced by the influence of land hydrology or tidal aliasing on the ocean signals. As we saw in the comparison to the *in-situ* data, the model performs better in capturing OBP

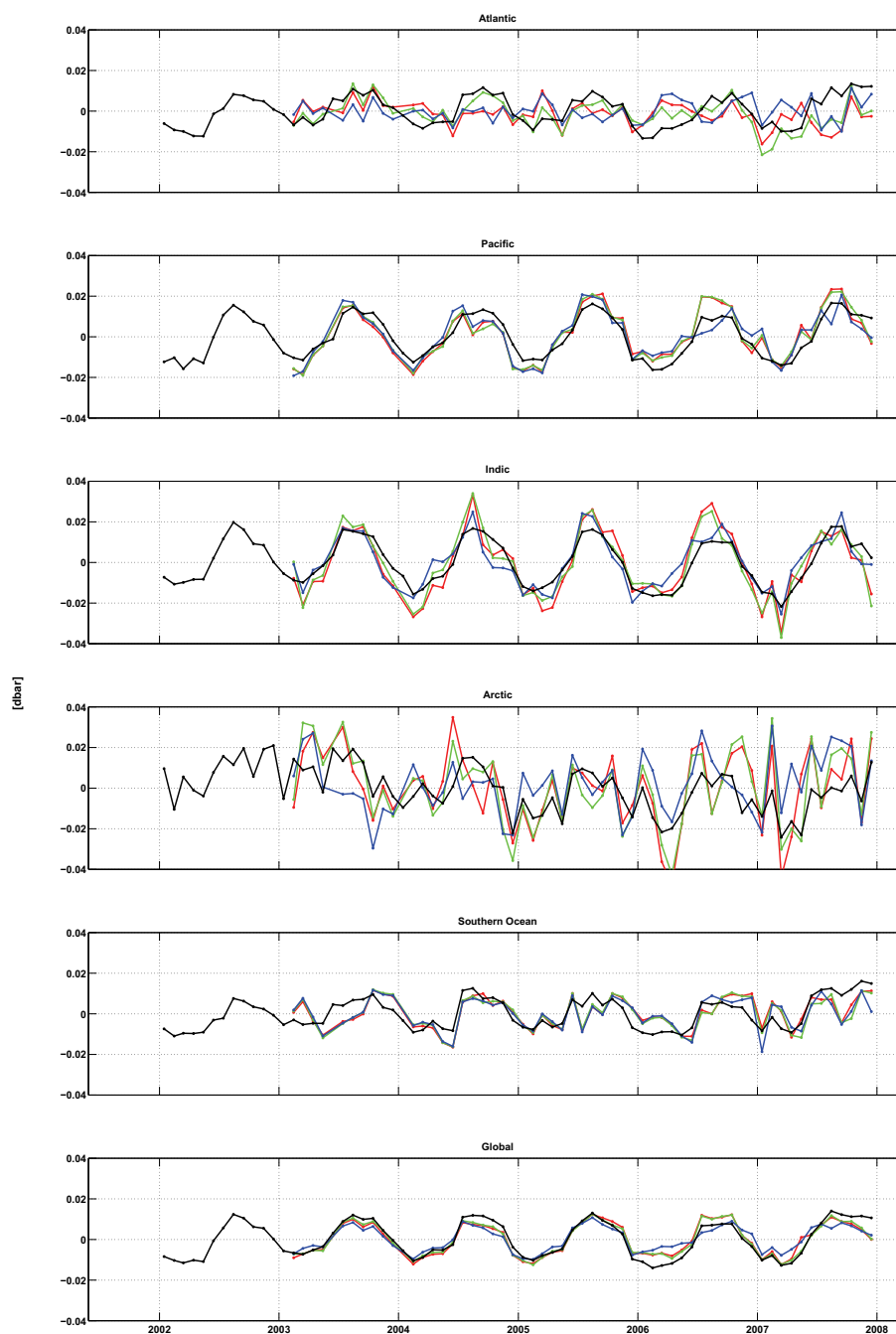


Figure 5.14: Basin-averaged time series of ocean bottom pressure anomalies derived from model results (black) and GRACE solutions (blue: JPL, red: GFZ, green: CSR).

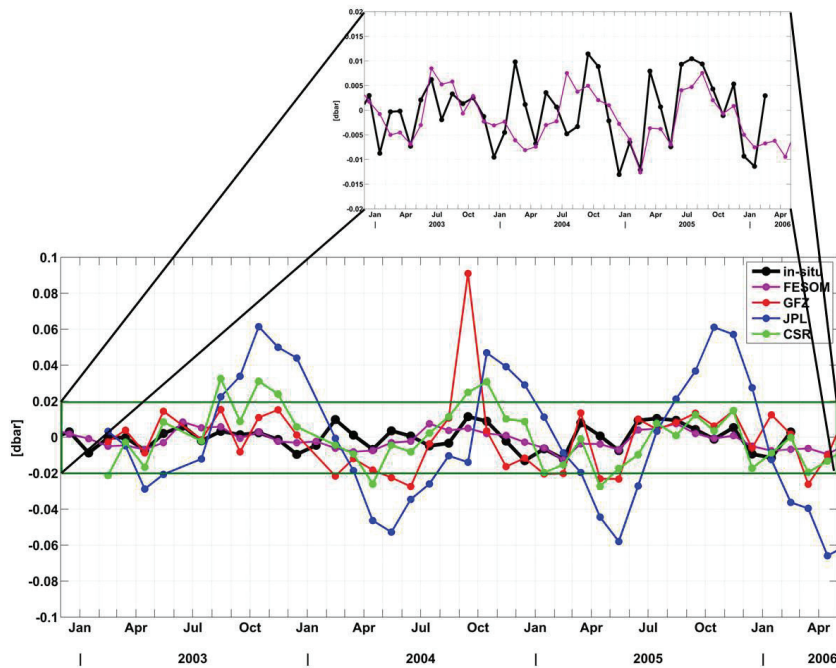


Figure 5.15: Time series of OBP anomalies in the MOVE array (tropical Atlantic) derived from *in-situ* data (black), GRACE (JPL: blue, GFZ: red, CSR: green) and FESOM (magenta).

anomalies in the MOVE array part of the Atlantic (Sec. 5.4.1). If we have a closer look at the OBP anomalies measured in this area, we can see that the *in-situ* measurements are highly overestimated by GRACE. The standard deviations differ by a factor of 3 (GFZ, CSR) to 6 (JPL). FESOM results show a better agreement in amplitude and phase (Fig. 5.15). The standard deviation of 0.7 mbar is very close to the measured deviation of 0.67 mbar. Although some features on a monthly scale cannot be reproduced, the model is apparently able to reproduce the annual cycle. The large overestimation in the GRACE data indicates that the solution in this region is dominated by non-oceanic effects like a land leakage (from the Orinoco basin) or the already discussed tidal aliasing which could also lead to an influence on the basin-wide average.

In variance maps of OBP anomalies derived from the de-striped solutions the effect of aliasing becomes even more obvious (Fig. 5.16). We see that the striping is mostly reduced in the CSR solution whereas artifacts still remain in the GFZ solution. The JPL solution features high variability north (and south-east) of South America which can not be observed either in the two

other products or the ocean model FESOM. This spatial feature covers the entire MOVE array and indicates that the large annual cycle detected in the time series of this solution is present for a large region in the tropical Atlantic.

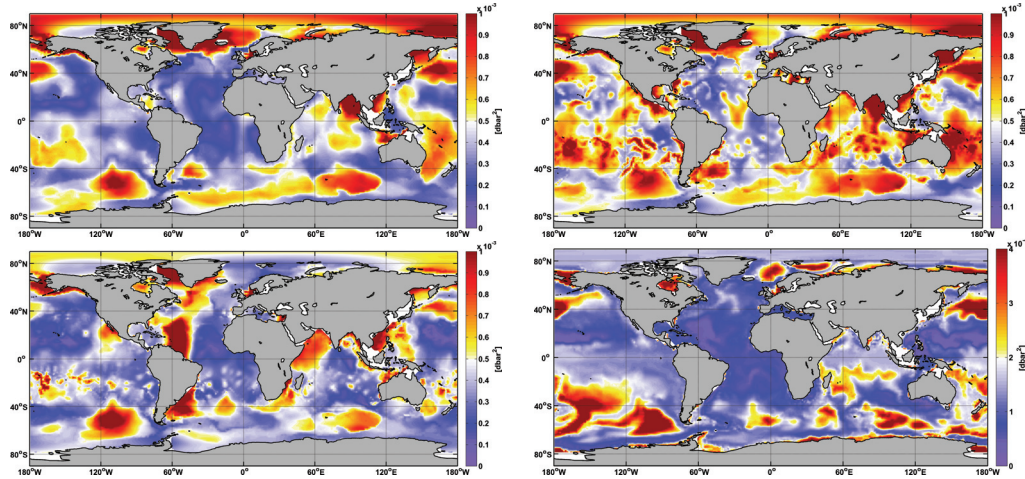


Figure 5.16: Variance of OBP anomalies derived from the de-stripped GRACE solutions (upper left: CSR, upper right: GFZ, lower left: JPL) and FESOM simulations (lower right).

In general, we see that patterns of high variability as seen in the model simulations can also be detected in the GRACE solutions. Especially in the Southern Ocean the patterns agree well in their spatial distribution. As already indicated in Section 4.3, these patterns are strongly related to f/H contours. The highly variable North Pacific can clearly be detected in GRACE and FESOM. However, strong fluctuations that may be related to the Zapiola Gyre close to the south-east coast of South America are much weaker in the model simulations. Agulhas Rings south of Africa moving to the North imprint a signal in the GRACE solutions which are missing in the model. Due to the horizontal resolution of about 1.5° the model cannot reproduce the high fluctuations in this region. Apparently, features originating from mass redistribution related to over-land effects, like the Monsoonal Flooding in Bangladesh or the changing ice mass balance of Greenland, induce strong variability in the GRACE solutions. These features are not included in the model implementation and therefore not captured.

5.5 Conclusions

We have presented a newly developed pattern-filtering method to obtain global fields of ocean mass anomalies from GRACE monthly solutions. The algorithm is based on the detection of patterns of coherent ocean bottom pressure variability; it uses information from modeled circulation patterns. We have demonstrated that the new method yields improvements for the correlation between GRACE-derived and *in-situ* OBP anomalies. Not only is this true for the high latitudes where the Gauss-filtered solutions were already good at many locations, but also in the tropics and close to the coasts the pattern-filtered GRACE-derived OBP signals get closer to the observations, so that the number of positions with a significant correlation between GRACE and in situ data increases. Land leakage effects are strongly reduced. The new pattern-filtering method thus provides the ability to extract features of oceanic water mass movements in more detail.

The de-stripping reduces noise in the GRACE solutions of all three processing centers and yields high correlations between GRACE-derived and the *in-situ* data. Whereas increasing of the radius of the additionally applied Gauss filter has no large impact on the correlation between *in-situ* and de-stripped GRACE data, the variance decreases with a larger Gauss radius. The variability of the *in-situ* OBP is overestimated in the 300 km solution for most of the arrays. The 500 km and 750 km solutions feature a more similar variability to the *in-situ* data.

A combination of a high resolution (300 km Gauss filtered) de-stripped solution with the pattern filtering algorithm improves correlations even further. However, in the tropical Atlantic GRACE solutions from the CSR, GFZ, and JPL, still fail to reproduce the variability seen in the *in-situ* measurements. In general, an overestimation of the amplitudes of the time series measured by the pressure gauges can be found in this region. This overestimation is mostly pronounced in the JPL data which feature an unrealistically large hydrological cycle probably due to aliasing effects or a large hydrological cycle over land (Orinoco basin) influencing the oceanic signals in this region.

The regional assessment of GRACE data in the different arrays indicates that the product from CSR features the highest agreement to the *in-situ* data for most of the arrays. In general, the CSR and GFZ solutions show very similar results whereas the JPL product features large differences to both especially in the Arctic and tropical Atlantic. These differences can only be referred to the different processing software which is used at the processing centers since a consistent set of background models is used for the de-aliasing of all Release 04 products.

On basin and global scale the GRACE solutions mainly coincide with

results from our ocean model FESOM. The annual cycle of the global average found in FESOM and GRACE agrees well with findings by Lombard et al. (2007) in amplitude and phase. Main differences can be detected in the Atlantic and Arctic ocean. In the case of the Atlantic those discrepancies may be related to the previously discussed hydrological cycle or aliasing effects. Differences between the ocean model and GRACE in the Arctic Ocean can be mainly attributed to over land processes like the Greenland ice sheet melting which is measured by GRACE, but not resolved in the model.

Chapter 6

Ocean mass variability in the Southern Ocean

The Antarctic Circumpolar Current (ACC) attracts attention of oceanographers due to its unique role in the world ocean. It circles Antarctica providing connections between major ocean basins and has thus an important effect for global oceanic exchange and variability. Understanding the driving forces of the ACC variability presents a challenging task for both theoretical and observation-based investigations. The theoretical principles underlying the ACC dynamics have been discussed in many papers (see e.g. Olbers et al. (2004) for a recent study on the dynamical balance, transport and circulation).

The average velocities (10 cm/s) in the ACC are relatively slow, but due to the depth the transport is high compared to any other current. In a recent study (Cunningham et al. (2003)) an average transport through the Drake Passage of 134 Sv (with a standard deviation of 11.2 Sv for the mean), and transport variations from 95 Sv to 158 Sv were found. The maximum transport tends to occur in late winter and early spring. The main transport is carried in two jets, the Subantarctic (53 ± 10 Sv) and the Polar Front (57 ± 5.7 Sv) (Fig. 6.1).

The zonal geostrophic transport is in balance with a meridional pressure gradient. The latter is a consequence of the westerly winds over the Southern Ocean, which produce a northward Ekman transport leading to a slope in the sea surface and, on a larger time scale, affecting the oceanic density distribution. Together with buoyancy forcing this induces the meridional pressure gradient and an eastward geostrophic flow.

Changes in the atmospheric pressure gradient between the low pressure system around Antarctica and the high pressure system at mid-latitudes modulate the strength of westerlies. Due to this relation atmospheric fluctu-

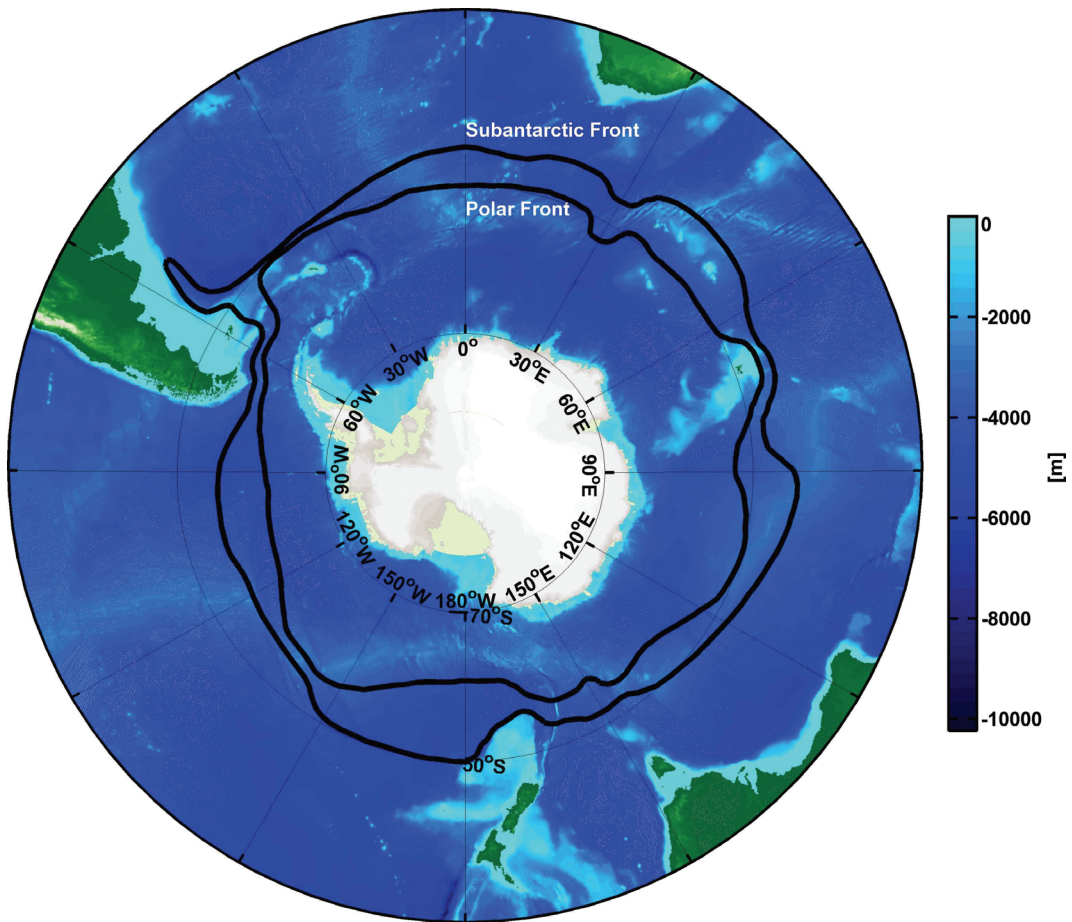


Figure 6.1: Bathymetry of the Southern Ocean. Black lines indicate the mean positions of the Subantarctic and Polar Front (Belkin and Gordon (1996)).

ations are connected to the transport in the ACC.

Variability of atmospheric patterns over the Southern Hemisphere is dominated by the Antarctic Oscillation (AAO) or Southern Annular Mode (SAM). This mode explains 20-30 % of the total variance in the wind fields (Thompson and Solomon (2002)). Since short-term transport fluctuations in the ACC are found to be mainly barotropic, the relationship between oceanic transport variability and the SAM is of special interest for understanding the ACC.

Meredith et al. (2004) (see also Olbers and Lettmann (2007)) found a connection between the SAM index and volume transport derived from model simulations on an annual time scale. A correlation of about 0.68 significant at a 99 % level of the SAM index to sea surface pressure measurements

south of Drake Passage could be observed. Interannual month-by-month trends from 1990 to 1999 in the SAM agree well with observations of ocean bottom pressure south of Drake Passage. They concluded that the transport variability is therefore related to the SAM.

These findings contradict recent investigations of ACC transport variability (Cunningham and Pavic (2007)) based on observations of surface geostrophic currents through a section across Drake Passage. SAM was found to be only weakly correlated with the transport variability observed in Drake Passage. A positive trend detected in the SAM (Thompson and Solomon (2002)) that is related to a long-term strengthening of the westerly winds and thus expected to influence the ACC transport has not been found in the ocean measurements. This controversy invites new studies based on both observations and numerics to clarify the connections behind the ACC transport variability. This section contributes in this direction as a study on the transport variability related to OBP anomaly gradients derived from GRACE solutions. Based on results from FESOM simulations, previous studies and utilizing *in-situ* OBP data, the recent de-striped GRACE releases are evaluated for ACC transport variability. A study on the relation of SAM and GRACE OBP provides valuable information on the ability of GRACE to capture oceanic variability in the temporal and spatial domain by using known and FESOM-based SAM/OBP-relations.

6.1 OBP-estimated transport variability from GRACE and FESOM

Ocean bottom pressure fluctuations yield a relation to the transport variations via the momentum equations. The region of Southern Ocean is a good candidate for the validation of GRACE data with respect to their ability to capture transport variability. Barotropic variations in the ACC induced by the SAM can be expected to imprint a signature in the GRACE ocean bottom pressure data. Quantification of transport variability as seen in GRACE can then improve our understanding of the mass variability in the Southern Ocean and the ACC in particular.

First encouraging results in the field of observing ACC transport variability with GRACE have been obtained by Zlotnicki et al. (2006). They compared ocean bottom pressure data derived from the early JPL GRACE Release 02 along 40° S and 65° S and the difference between them for each basin with results obtained from the ocean models ECCO and ROMS. Furthermore, they used QuikSCAT wind estimates to underline the relation

between wind fluctuations and changes in zonally (along the southern boundary of the ACC) averaged bottom pressure. A good agreement in phase was found for each basin between the models and GRACE-derived differences, but the amplitude was generally overestimated in GRACE data filtered with a 500 km Gaussian filter. A three-year decreasing trend has been detected in all three data sets in the average along the southern ACC boundary which was related to a weakening of winds.

Due to aliasing artifacts in the GRACE solutions (see Section 5.1) errors in the amplitudes of OBP anomalies continue to introduce uncertainties into the determination of the range of variability. However, these errors are apparently reduced in the new GRACE releases as well as by new filtering mechanisms (such as pattern-filtering, de-stripping etc. discussed in Section 5.2 and 5.3).

Since 2006 new releases of GRACE data with reduced errors have been produced by the different processing centers. The time series are now spanning the period 2003-2008. Corrections for geocenter motion and post-glacial rebound (PGR) are included in the post-processed fields based on Chambers (2006).

We investigated the representation of the ACC in the currently available de-stripped GRACE solutions. For this purpose transport variability derived from GRACE OBP anomalies has been compared to results obtained by Zlotnicki et al. (2006) as well as to variations derived from simulated OBP anomalies and Drake Passage volume transport. We utilized the FESOM results to derive OBP anomalies as well as the total transports.

In addition to the estimation of transport variability we analyzed the representation of SAM in the GRACE-derived and FESOM OBP. We determined the connection between the atmospheric variability (as represented by SAM) and transport variability that can be derived from GRACE retrievals and model simulations. This analysis gives an insight into how the atmospheric variability influences the mass distribution measured by GRACE and simulated by FESOM.

6.2 Estimates of ACC transport variability

Most studies on the ACC transport variability focus on the region of Drake Passage. In the South the current is limited by the northern tip of the Antarctic Peninsula and in the north by the southernmost boundary of South America. The flow has to pass this tight opening and therefore the characteristics of the entire current are reflected at this place.

Although, most of the studies focus on the ACC in Drake Passage, an

investigation of the ACC in other regions is of interest. Determining the transport variability in different regions of the Southern Ocean gives us an idea of the spatial and temporal development of the flow.

We already evaluated OBP variability in the AWI ACC PIES array (Section 4.3) and assessed the ability of FESOM (Section 4.3) and GRACE (Section 5.3) to capture the oceanic variability in this region. The gradients of OBP anomalies now provide an estimate of the transport variability (Hughes et al. (2003)) of the ACC south of Africa.

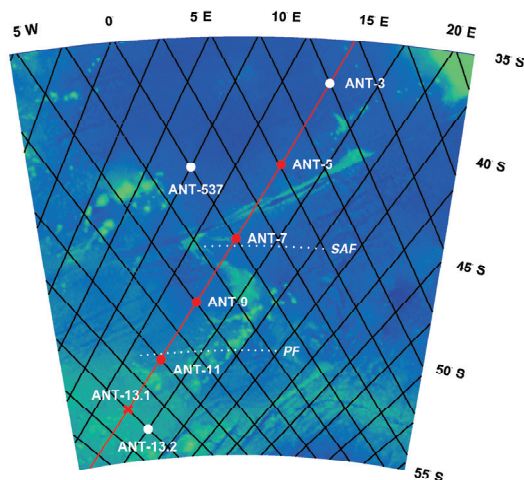


Figure 6.2: Map of PIES positions in the AWI ACC array. The position of ANT-13 was moved to the Greenwich meridian during Polarstern cruise ANT-XXIV/3. White lines indicate the mean position of the Subantarctic Front (SAF) and the Polar Front (PF))

Calculation of the ACC transport (and transport variability) in Drake Passage and in the ACC BPR array using FESOM simulations provides a view on the representation of the current in our ocean model. Regional differences in the ACC transport are evaluated and quantified. Transport variability derived from *in-situ* OBP give a ground-truth estimate and form a base for an quality assessment of GRACE and FESOM data with respect to capture the ACC transport variability.

6.2.1 Regional comparison of ACC transport variability

In order to determine the regional differences in ACC transport variability, we use model simulations and compared the oceanic transport through Drake Passage and through the section constrained by the northern- and southern-most PIES positions in the BPR array.

Several studies of transport through Drake Passage show that the total transport is of about 134 Sv (e.g. Cunningham et al. (2003)). FESOM model simulations indicate a total transport of approximately 127 Sv (Fig. 6.3) which lies in the error bounds of the estimates derived from observations.

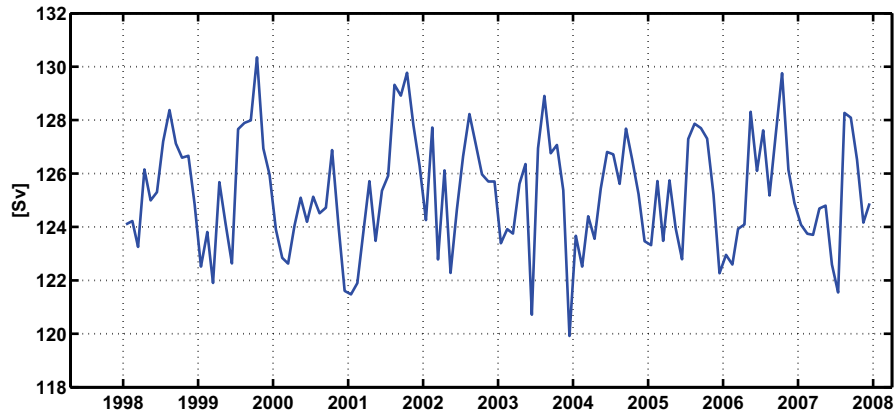


Figure 6.3: Simulated transport through Drake Passage derived from a 10 yr FESOM simulation with a 40 yr spin-up.

Considering the circumpolar structure of the current, we expect almost the same amount of transport through any¹ section across the flow. Therefore, we also expect that the transport measurement across the ACC array south of Africa is of the same amount as the transport in Drake Passage.

To assess this, we derive the total transport through the section between PIES positions ANT-5, situated at $41^{\circ} 08' S$ $9^{\circ} 56' E$, and ANT-13 at $52^{\circ} 30' S$, $1^{\circ} 24' W$ from model simulations. FESOM results show a total transport of about 76 Sv (Fig. 6.4) which is much smaller than the transport through Drake Passage. However, those differences can be explained by the spatial setup of the array and the representation of the ACC in the model.

¹Except sections south of Australia, where the ACC transport is influenced by the Indonesian Throughflow.

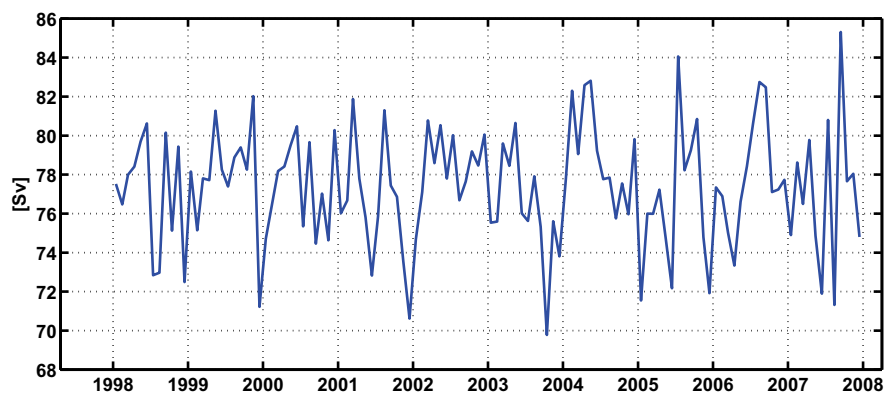


Figure 6.4: Simulated transport through section defined by ACC PIES array.

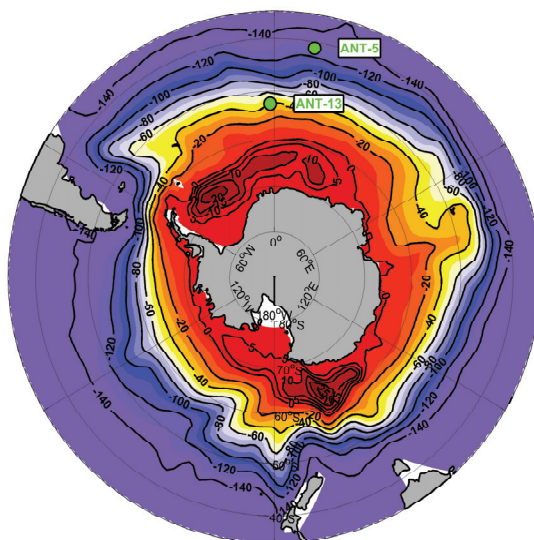


Figure 6.5: Southern Ocean stream function derived from FESOM simulation. Current boundaries of the AWI ACC PIES array are indicated by the northern- and southernmost PIES position in the periphery of the current. Position ANT-5 and ANT-13 are marked by green circles.

The main jets, the Subantarctic and the Polar Front, are covered by the PIES array and the main part of the real transport is likely to be captured. However, due to the coarse model resolution, the flow is broader than ob-

served (Fig. 6.5), so that the transport between the PIES ANT-5 and ANT-13 represents only a part of the total model transport. When integrated over an extended section from 40° S to 60° S the total transport is estimated to be about 127 Sv (Fig. 6.6), similar to the transport through Drake Passage.

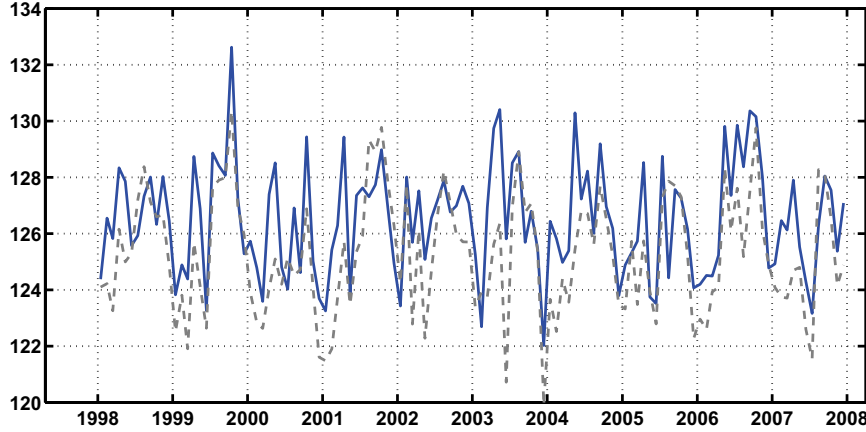


Figure 6.6: Transport through section south of Africa covering the entire model ACC (blue). Gray line indicates transport through Drake Passage.

Both sections, the Drake Passage and South Atlantic section, feature a similar peak-to-peak variability.

6.2.2 Transport variability in the ACC array from measurements and FESOM simulations

Hughes et al. (2003) provides a formula for calculating estimates of the barotropic geostrophic transport. Being aware of the assumptions made for the derivation of this formula, an approximation of transport variations between to stations a and b can therefore be derived from:

$$\Delta T_g = \frac{H}{f\rho_0} (\Delta p_b - \Delta p_a), \quad (6.1)$$

In which ΔT_g is the change of the mean vertically averaged transport. The change in pressure at station a and b is denoted by Δp_a and Δp_b . The Coriolis parameter f is taken constant using the average latitude of the stations. The vertical scale height H is set to the average depth of the two stations.

For the validation of GRACE-derived transport variability in the AWI ACC array, a comparison between FESOM-, GRACE-, and *in-situ* OBP gradients provides a view on the spatial scale of processes resolved by GRACE (and FESOM).

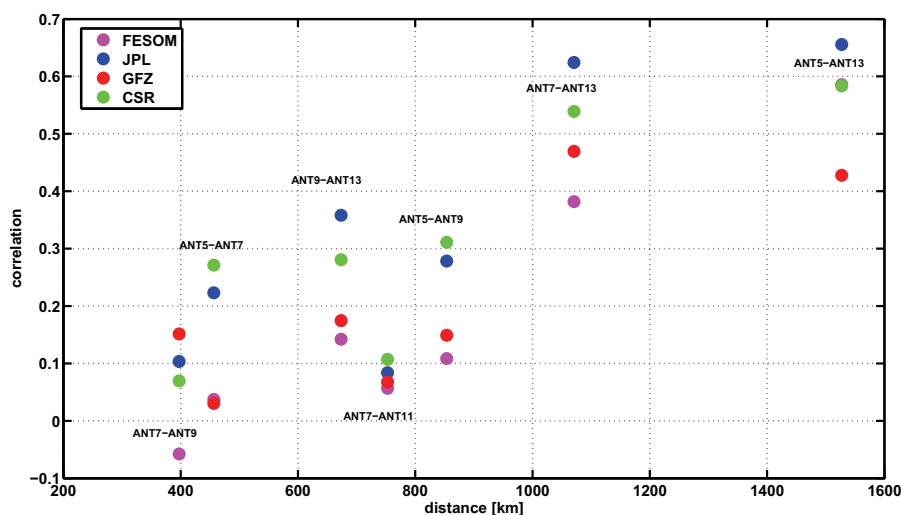


Figure 6.7: Correlation between OBP gradients derived from GRACE, FESOM and *in-situ* OBP gradients depending on station distance.

As indicated figure 6.7 the correlation between FESOM/GRACE and *in-situ* OBP gradients increases with increasing distance between the considered stations. The correlation to the gradient between ANT-7 and ANT-11 forms an exception. Although the distance between ANT-7 and ANT-11 is larger than for example the distance between the stations ANT-9 and ANT-13, the OBP anomaly gradients of *in-situ* and FESOM/GRACE data show a lower correlation. Spatially coherent features in the time series, like an annual cycle which leads to a high correlation of *in-situ* and FESOM/GRACE OBP anomalies in the first place, are canceled out when computing the gradients. Local processes like the meandering of the Subantarctic and Polar Front in the vicinity of the PIES ANT-7 and ANT-11 (see Fig. 6.2) likely dominate the measurements. These features are not reproduced by FESOM or GRACE at a resolution of a few hundred kilometers.

In general, FESOM gradients feature a lower correlation to the *in-situ* data than the GRACE-derived gradients. As indicated by the results from section 6.2.1, the pathway of the ACC may extend more to the North and to the South than in reality. Thus, the anomalies of OBP gradients between

the PIES positions in the model likely differ from real fluctuations, since the hydrographic features are shifted in the broader model flow.

Comparison of the three GRACE solutions with respect to the correlation to the *in-situ* data indicates that gradients derived from the JPL solution resemble the observations the most. The CSR solution shows a slightly higher correlation to the *in-situ* gradients than the JPL solution in some cases, whereas the GFZ solution features the lowest agreement with the *in-situ* data.

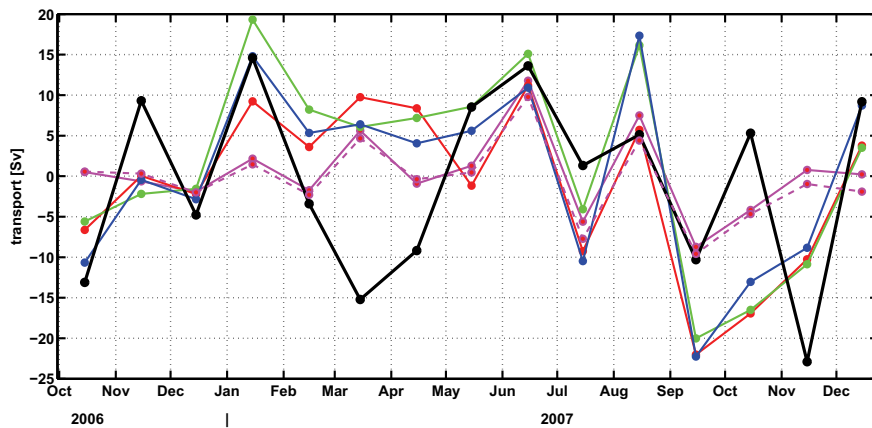


Figure 6.8: Transport variations derived from GRACE, FESOM and *in-situ* OBP. GRACE-derived variations are shown in red (GFZ), green (CSR), and blue (JPL), *In-situ* variations in black. FESOM OBP-estimated transport variations indicated by solid and exactly integrated total transport variations indicated by dashed magenta line.

Combining the gradients between the stations to a section-integrated time series of transport variability by using Eqn. (6.1) gives an estimate of the total anomalies in the array. The standard deviation from *in-situ* gradients is estimated to be 11.5 Sv. All of the three GRACE solutions, from CSR, GFZ, and JPL, feature a similar range of variability which is of about 11 Sv, whereas the GFZ product shows the smallest variability with about 9.8 Sv (CSR: 11.4 Sv, JPL: 11.0 Sv). The model underestimates this variability and reaches a range of 4.9 Sv (Fig. 6.8).

Month-to-month variations of all the time series are similar; the correlation between GRACE/FESOM and *in-situ* data is around 0.6 at a significance level of 99 %.

According to results from FESOM simulations, the transport fluctuations related to OBP as derived from Eqn. (6.1) explain about 95% of the variance

of the volume transport variations (Fig. 6.8). Although this relation may be weaker in reality, this finding indicates that these fluctuations resemble the total variations to a considerable extent.

6.3 The Southern Annular Mode and its connection to ACC transport fluctuations

6.3.1 SAM index, sea level pressure patterns and wind anomalies

A large part of the variance in the Southern Hemisphere wind field can be explained by a dominant atmospheric mode. Known as the Antarctic Oscillation (AAO) or the Southern Hemisphere Annular Mode (SAM), it consists of an oscillation of sea level atmospheric pressure between polar and subtropical latitudes, associated with oscillations in circumpolar winds in the troposphere and stratosphere, including at the sea surface.

The SAM can be defined as the leading principal component of the 850-hPa geopotential height anomaly south of 20° S (or of the sea level pressure; the corresponding time series displaying a correlation of 0.99 (Lefebvre et al. (2004)). A positive (negative) SAM is associated with lower (higher) than normal sea level pressure (SLP) at high latitudes and higher (lower) than normal SLP at low latitudes. As a consequence, during years with a positive SAM index, the westerlies are intensified in the region of the ACC.

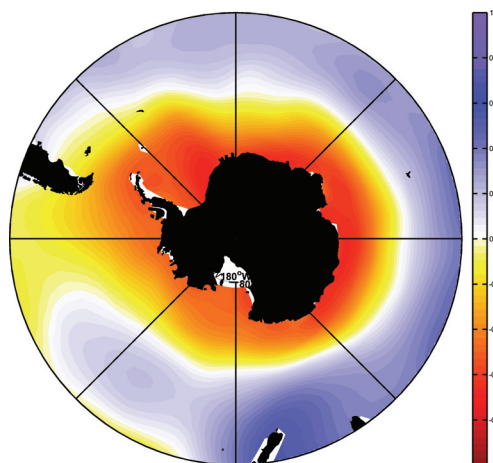


Figure 6.9: Correlation for 2002-2007 between SLP derived from NCEP/N-CAR reanalysis and the SAM index of Marshall (2003).

The SAM index used in this study was provided by Marshall (2003). Sea level pressure data from 12 pressure gauges on the 40° S and 60° S circle has been collected in the period from 1957 to 2007.

The correlation of the SAM index to the NCEP reanalysis SLP is shown in figure 6.9. An annular band of coherent signals around Antarctica can be detected. As SAM describes anomalies of the gradient in sea level pressure anomalies between 40° S and 60° S, a positive SAM index indicates higher than normal pressure at 40° S and lower than normal pressure at 60° S (vice versa for a negative SAM index). Therefore, SAM has a positive correlation to SLP in the region of 40° S and a negative correlation around 60° S.

6.3.2 The connection between SAM and the ACC transport

Various studies (e.g. Meredith et al. (2004)) found transport of the ACC through Drake Passage related to SAM and indicate a possible use of SAM index as a proxy for ACC transport variability. A connection between fluctuations in the Southern Ocean wind field and transport variations was found on scales of 10-220 days (Hughes et al. (1999)). On longer time scales the growing influence of baroclinicity weakens the relation between atmospheric and oceanic variability (Olbers and Lettmann (2007)). SAM as a measure for atmospheric variations can be expected to be related to transport anomalies on similar time scales.

However, recent comparisons of the SAM-related fluctuations and fluctuations derived from *in-situ* measurements of Drake Passage transport indicate only a weak relation between the SAM index and transport fluctuations. In a comprehensive study by Cunningham and Pavic (2007) who used current meter as well as satellite and hydrographic measurements to determine transport variability over the period 1992-2004 only a weak correlation of transport variations and SAM was found. They concluded that SAM is not likely to yield a good proxy for ACC transport variability.

Being aware of these contradicting results, we revisit the relation of SAM to the variability of mass redistribution derived from GRACE gravity solutions. We also compare SAM to transport and OBP anomalies derived from the model to get additional support to the existence of correlation.

Findings of Zlotnicki et al. (2006) have already indicated a relation between GRACE-derived OBP anomalies averaged along the southern ACC boundary and the atmospheric variability as seen in the QuikSCAT wind stress measurements. Our study here is complementary to this earlier study by using newly available GRACE solutions and simulations performed with

FESOM. Changes in large scale atmospheric variability are represented by the SAM index. Those variations are found to be related to the GRACE-derived OBP anomalies. Extremes on a seasonal or even shorter time scale in SAM are captured by GRACE. As OBP is connected to transport, this relation supports the assumption of a connection between SAM and transport variability. However, on longer (larger than annual) time scales a weakening of this relation is expected and is confirmed by the GRACE solutions (Fig. 6.10).

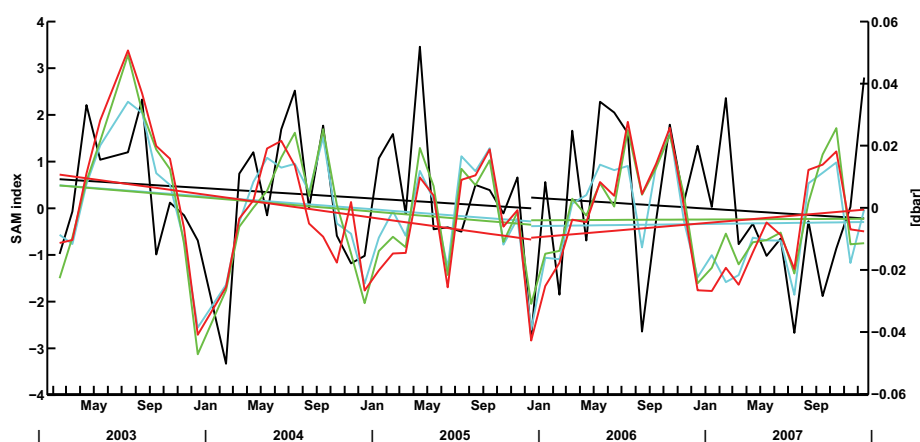


Figure 6.10: Time series of SAM index (black) and GRACE OBP anomalies averaged along the southern ACC boundary (ORSI et al. (1995)) (JPL: blue, GFZ: red, CSR: green).

The three-year decreasing trend found by Zlotnicki et al. (2006) in the QuikSCAT wind stress measurements as well as in the OBP anomalies derived from JPL GRACE RL02 along the southern ACC boundary can also be detected in the SAM index (Fig. 6.10) and the recent de-striped GRACE products. However, Zlotnicki et al. (2006) indicated a decrease of about 1.2 cm/yr equivalent water column height, whereas the newer GRACE retrievals show a trend of a few millimeters with a considerably large range of variability between the products from the three processing centers (GFZ: 7 mm/yr, CSR: 4.2 mm/yr, JPL: 3.9 mm/yr). In the following two years, GRACE OBP anomalies indicate a two-year increase and the SAM index still decreases slightly.

Comparing SAM index and FESOM Drake Passage volume transport variations, we find a correlation coefficient of only 0.4 between both but at a high significance level of 99 %. As can be seen in Figure 6.11, showing the time derivatives as monthly changes in SAM and FESOM volume transport

anomalies, a change in SAM from high to low, or vice versa, indicates a similar change in the transport. This indicates a connection between both quantities on a monthly time scale.

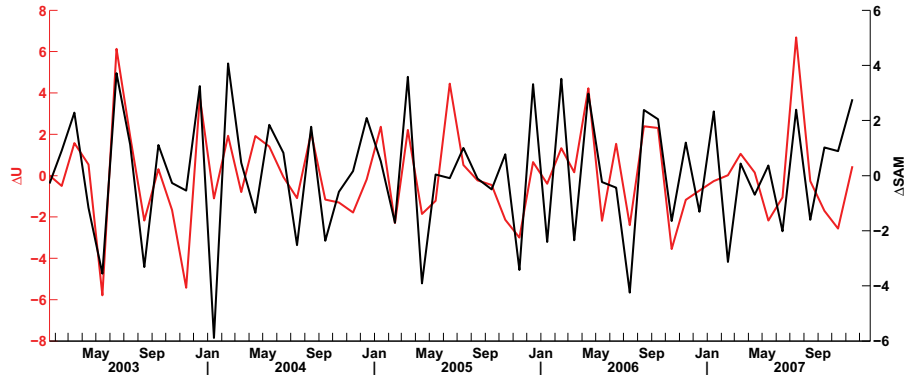


Figure 6.11: Monthly changes of SAM index (black) and FESOM volume transport anomalies through Drake Passage (red).

A model study by Lettmann and Olbers (2005) indicates that Drake Passage transport variations are related to OBP in the Southern Ocean with correlation patterns connected to f/H contours. Variations in transport are connected to OBP anomalies around Antarctica over a highly (negative) correlation. Measurements of OBP support the model results. OBP anomalies in the South of Drake Passage were found to be negatively correlated to the ACC transport derived from the OCCAM ocean model (Hughes et al. (2003)).

FESOM simulations yield similar results. We obtained spatial patterns of coherence between OBP and Drake Passage transport (Fig. 6.12). As SAM is connected to the volume transport in Drake Passage in FESOM simulations, we find the same patterns when correlating SAM and OBP. The patterns follow f/H contours and show high negative correlation around Antarctica.

These findings are not confined to only model simulations. The connection between SAM and OBP can also be detected in GRACE solutions (Fig. 6.13). Plotting f/H contours on the patterns of correlation between SAM and OBP derived from the three de-striped and the pattern-filtered solutions shows that we can find the same f/H -related patterns in GRACE retrievals as well.

Apparently, the 300 km de-striped solution is still influenced by the aliasing effects in the GRACE data. The correlation between the 300 km solution and SAM (Fig. 6.13, top left panel) shows circle-like small-scale patterns

with alternating high and low correlation. However, the mode of variability following the f/H contours as seen in FESOM can be clearly identified.

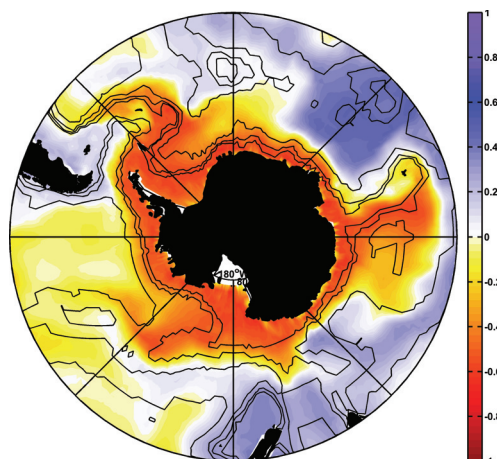


Figure 6.12: Correlation between the SAM index and FESOM OBP anomalies (color coded). Isolines denote f/H contours.

In the 500 km de-striped solution (Fig. 6.13, top right panel) the noise is highly reduced and the spatial shape of the correlation with SAM is more pronounced. A higher smoothing radius as seen in the 750 km de-striped solution (Fig. 6.13, bottom left panel) causes a weakening in the relationship between the SAM/GRACE-OBP correlation and the f/H contours.

Using information on the circulation by applying the pattern filter to the 300 km de-striped GRACE solution (Fig. 6.13, bottom right panel) reduces striping artifacts and additionally induces a more spatially refined SAM/GRACE-relation.

An EOF analysis indicates that GRACE OBP anomalies from the 300 km and 500 km de-striped solutions are dominated by striping artifacts (Fig. 6.14). The first EOF of the 300 km de-striped solution, showing small circle-like spatial patterns, explains 62 % of the variance. In the 500 km de-striped solution those patterns can still be identified to be dominant, but the explained variance is reduced to 23 %. The 750 km de-striped and the pattern-filtered solution show a mode that encircles Antarctica which resembles the correlation patterns shown previously. The explained variance is 22 % in case of the 750 km and 25 % for the pattern-filtered solution. Comparing this mode to the correlation found with SAM (Fig. 6.13) which features similar spatial patterns indicates that a considerable part of the GRACE-OBP signals are connected to the atmospheric variability described by SAM.

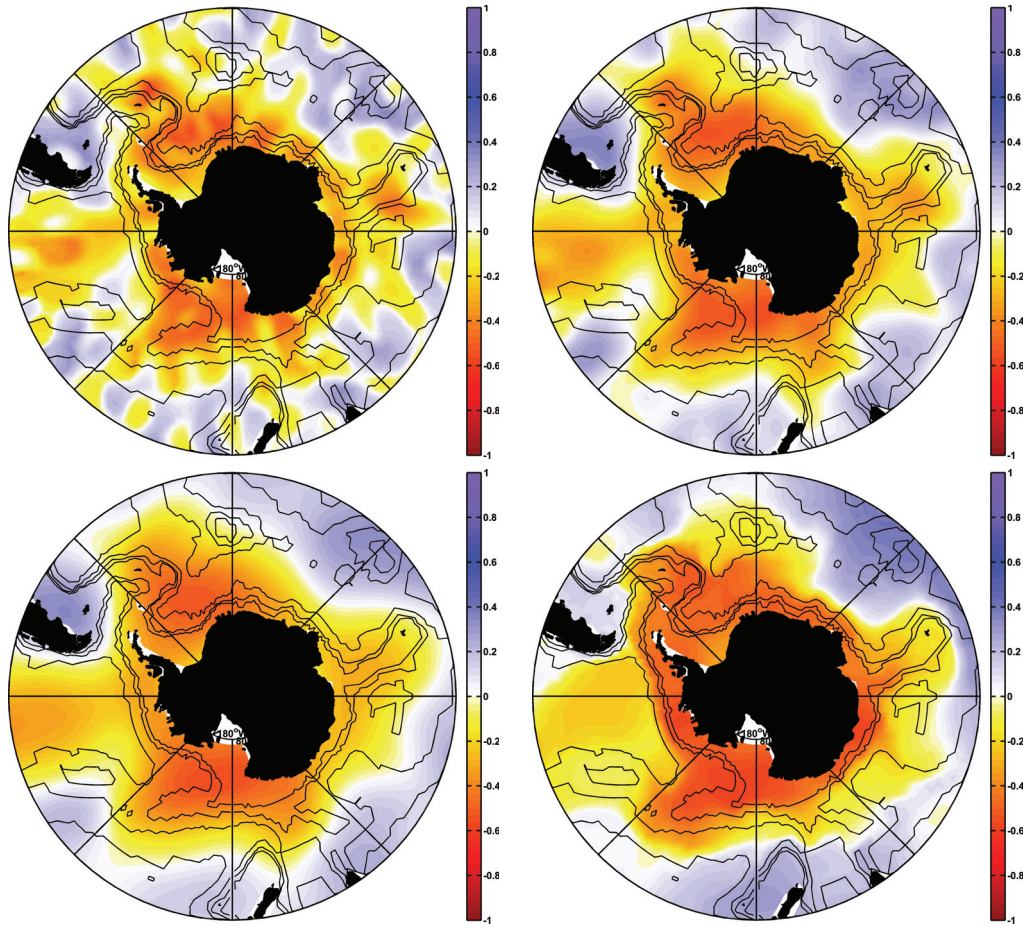


Figure 6.13: Correlation between the SAM index and GRACE-derived (GFZ RL04, de-striped) OBP (color coded). Top panel: 300 km de-striped (left), 500 km de-striped (right). Bottom panel: 750 km de-striped (left), pattern-filtered (right). Isolines denote f/H contours.

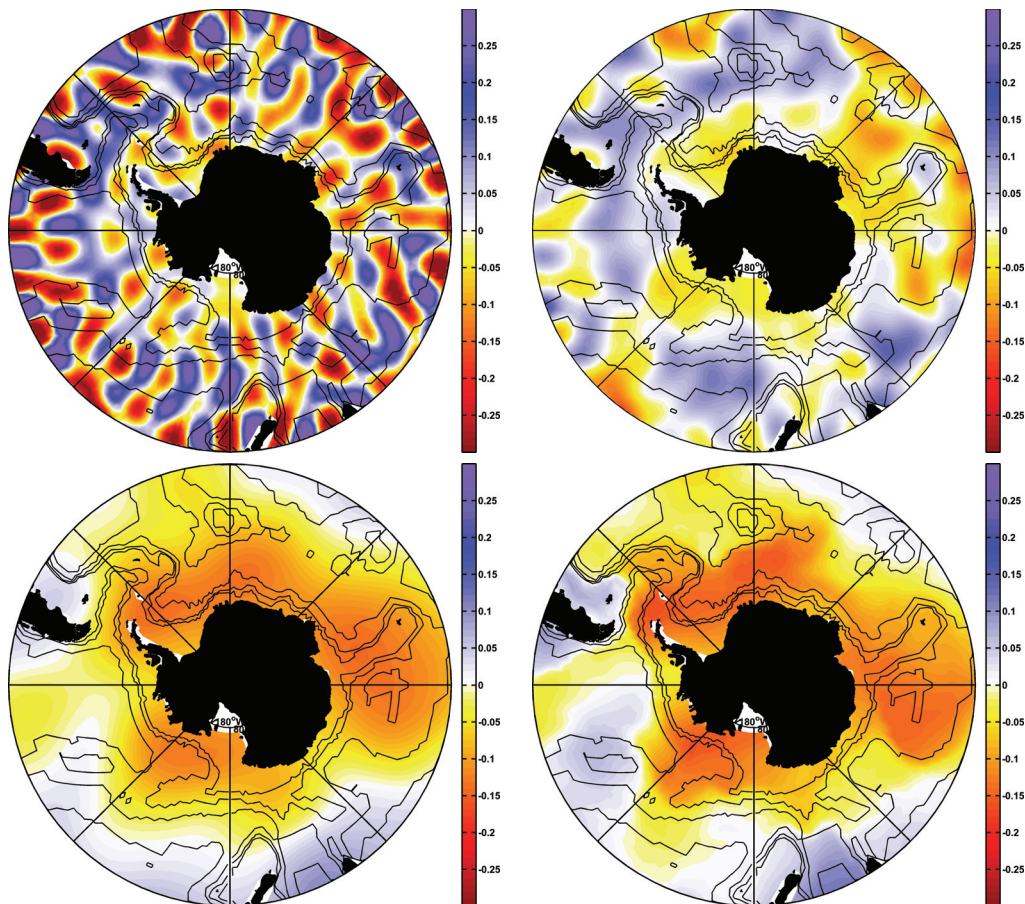


Figure 6.14: First EOF of GRACE-derived (GFZ RL04, de-striped) OBP anomalies in the Southern Ocean. Top panel: 300 km de-striped (left), 500 km de-striped (right). Bottom panel: 750 km de-striped (left), pattern-filtered (right). Isolines denote f/H contours.

6.4 Discussion

Estimates of transport through Drake Passage, derived from FESOM simulations, agree well with the observed ACC transport (Cunningham et al. (2003)). We confirmed a similar range of simulated transport in the region south of Africa. However, deriving the transport through a section defined by an BPR array covering the ACC yields a much smaller transport. This was found to be due to the broader representation of the current in FESOM.

Evaluation of transport variability in the AWI ACC array utilizing the relationship between OBP anomaly gradients and transport fluctuations according to Hughes et al. (2003) indicates, that, based on model results, total transport fluctuations and OBP-related fluctuations in this region mainly coincide. Deriving transport variability from OBP measurements thus may provide a good estimate. The GRACE-derived fluctuations resemble the range of variability of the *in-situ* data and reproduce the month-to-month variability to a considerable extent. However, on spatial scales <700 km GRACE may fail to reproduce the variations.

The short-term trend indicated by findings of Zlotnicki et al. (2006), is confirmed in the recent GRACE releases as well as in the SAM index. However, the sharpness of the decrease is found to be much smaller. In the following two years of GRACE observations the trend is even reversed. The difference to previous findings may be related to general improvement and different post-processing of the GRACE data. For example in the de-striped products the PGR is taken into account which likely affects long-term variations.

Hughes et al. (1999) described wind-related fluctuations of the flow following f/H contours encircling Antarctica. We were able to reproduce these findings by correlating the atmospheric mode SAM with FESOM model simulations and confirmed that this pattern of variability is also present in the data derived from GRACE.

The pattern-filtered solution shows the clearest signal of the southern mode of oceanic variability related to atmospheric fluctuations. This connection can also be detected in the three Gauss filtered de-striped GRACE solutions and thus is not confined to the pattern filtering (which introduces information on the geostrophic contours to the GRACE products). However, aliasing artifacts dominate the spatial distribution in the 300 km and 500 km de-striped solutions and weaken the relation of the patterns to f/H contours.

In general, we found that GRACE-derived ACC transport fluctuations agree with the simulated transport showing correlations around 0.7. Although the atmospheric variability as expressed by SAM is related to simulated and GRACE-derived fluctuations, only weak correlation was found.

Thus, most likely SAM cannot be used as a proxy for the ACC transport variability. However, the high correlation between model transport and GRACE-derived OBP indicates that GRACE is able to reproduce a large part of the ACC variability.

Chapter 7

Conclusions and Outlook

This study presents the validation of mass variations obtained from the Gravity Recovery and Climate Experiment (GRACE) over the ocean. One major goal of the GRACE mission is to provide an unprecedented view on the global ocean mass redistribution. After de-aliasing for atmospheric and tidal effects, GRACE gravity field anomalies on monthly time scales are assumed to be mainly caused by fluctuations in the Earth's surface mass. Over the ocean the monthly solutions of the gravity potential can be interpreted as variations in ocean mass, commonly expressed as ocean bottom pressure (OBP) anomalies. However, before using these data for oceanic research, a validation against ground-truth data is essential. This study provides a comprehensive comparison of GRACE-derived against *in-situ* OBP anomalies available from a global ocean data base compiled at the AWI. Simulations with the Finite Element Sea Ice–Ocean Model (FESOM; Timmermann et al. (2009)) complement the *in-situ* data with respect to the validation on regional and global scales and provide a base for identifying oceanic processes in the GRACE data.

For the validation of GRACE the *in-situ* observations and the ocean model first have to be prepared to give a realistic estimate of ocean mass variability. As the temporal signal of OBP measurements is dominated by tides, the *in-situ* data have to be corrected for tidal variability to provide a representation of the mass fluctuations induced by non-tidal oceanic currents. The ocean model FESOM as a Boussinesq and thus non-mass-conserving model, has to be modified with respect to mass conservation in order to give a more realistic representation of the ocean mass proxy OBP. Both issues have been solved and the realization has been presented in this thesis.

In order to correct the *in-situ* data for tidal variability, tidal corrections have been derived from a global tidal chart, the FES2004 (Lyard et al. (2006)), which provides estimates of the main tidal constituents. Since the

GRACE data is de-aliased using the same tidal chart, this approach yields a consistency of both data sets.

However, due to inaccuracies in tidal models a correction of OBP measurements using model data may leave part of the tidal variability in the time series. For the GRACE data processing this means that these unresolved tidal fluctuations may alias to low frequencies and thus affect the monthly solutions (Seo et al. (2008)). In order to evaluate tidal variability remaining in the time series when corrected by the FES2004, this study comprises an investigation of tidal variability derived from *in-situ* OBP measurements in an exemplary bottom pressure recorder (BPR) array in the South Atlantic (AWI ACC array) in comparison to the tidal chart FES2004. Tides have been derived from *in-situ* measurements using the IES Data Processing tool developed at the University of Rhode Island (Kennelly et al. (2007)). This tool gives an estimate of the principal tidal constituents as found in the OBP data.

Analysis of the *in-situ* measurements indicates that tidal variability increases from North to South for the diurnal tides, whereas amplitudes of the semi-diurnal tides decrease. These North-South structures can also be detected in the time series derived from the FES2004. Maps of the amplitudes of the principal diurnal and semi-diurnal constituents show spatial patterns indicating a North-South increase of the diurnal and decrease of the semi-diurnal tides in the entire South Atlantic region south-west of Africa.

The tidal model captures the phase of the tidal signals well whereas the amplitude especially of the short-period tidal constituents differs from the observed tides. For a correction it should be therefore kept in mind that tidal variability on short time scales is better described by using the empirical method based on the measurements than by the FES2004 model. The remaining energy induced by the diurnal and semi-diurnal tidal constituents is about an order of magnitude lower. Differences between the empirically- and model-derived tides feature a standard deviation of approximately 2 cm at a temporal resolution of 0.5 hours.

In order to make the non-mass-conserving FESOM applicable for the purpose of GRACE validation, two corrections enter the model simulations: a modification of the model implementation to consider mass and volume fluxes and a correction of the atmospheric forcing fields driving the ocean model.

The Boussinesq approximation used in the standard FESOM model leads to volume conservation rather than mass. Changes of the sea surface height due to steric effects are not considered in the continuity equation. As OBP is the integral over density (times gravitational acceleration) from ocean bottom to the sea surface, these changes would result in an unrealistic change in

OBP if not corrected. Therefore a correction of the sea surface height for consideration of steric effects following the note of Greatbatch (1994) has been applied.

Surface freshwater fluxes, i.e. precipitation, evaporation and runoff, contribute to the oceanic mass and have to be considered in the computation of OBP. For this purpose the contributions of these fluxes are added to the model sea surface height. The forcing fields, net precipitation and runoff, originate from different data sources (i.e. the NCEP/NCAR reanalysis and the HDM forced by ECMWF data respectively) and are not bound to be balanced. Therefore, a correction of the fields is necessary to enable the model to capture the mass budget in a realistic way. The assumption that globally averaged runoff balances the globally averaged net precipitation on time scales of a few years gives a correction of the freshwater fluxes and leads to a reduction of unrealistic features (i.e. large trends) in the global mass budget.

In Timmermann et al. (2009) FESOM has been successfully validated against hydrographic atlas data sets. In this study, the modified FESOM was additionally validated against *in-situ* OBP data on daily and monthly time scales. FESOM was found to agree well with the observations. In general, OBP anomalies simulated by FESOM are smaller in amplitude than the observations. However, the phase of the *in-situ* data is well captured. Especially at high latitudes we arrive at correlations larger than 0.7 at a high significance level of 95 %. Part of the subgrid variability as for example in the AWI ACC PIES array, where the Agulhas influences the BPR measurements in the Cape basin, cannot be explained by the model at 1.5° horizontal resolution.

As GRACE constitutes a completely new type of gravity measurements due to the unprecedented mission setup, the interpretation of the received data requires a careful and thorough post-processing. A common issue with the GRACE monthly solutions provided by the three processing centers GFZ, CSR, and JPL, is the effect of aliasing. During the data processing, "known" contributions (the so-called background models consisting of data from previous gravity missions, ocean and atmospheric models etc.) to the Earth's gravity field have been removed. Errors in the models used for the de-aliasing of GRACE data are transferred to the monthly gravity field solutions. According to the orbit configuration of GRACE, errors are amplified in spatial north-south elongated patterns of opposite sign amplitude.

In order to separate geophysical signals from the noise denoted as striping, filter algorithms have to be applied on the data. In this study, three kinds of filtering are discussed: Gaussian filtering, a filtering algorithm introduced by Swenson and Wahr (2006) and the filter approach which was developed

in the framework of this work (Böning et al. (2008)).

The three filtering algorithms were especially tested for their suitability to derive oceanic signals from GRACE gravity field solutions. The signals obtained over the ocean are found to be much smaller than the signals over land. Isotropic filters, like the Gauss filter, do not distinguish between land and ocean signals and therefore introduce an error known as land leakage to the oceanic data. This effect is mostly pronounced in the vicinity of river basins or ice sheets, where the hydrological cycle is large.

The pattern filter is based on the spatial coherence of ocean bottom pressure on monthly time scales derived from our ocean model FESOM. Ocean bottom pressure was found to be highly auto-correlated over regions with a diameter of approximately 1000 km. The correlations are used as weights to derive gridded ocean bottom pressure data from the spherical harmonic GRACE solutions.

A comparison of Gauss filtered and pattern filtered GRACE solutions to *in-situ* OBP data shows that using the pattern filter increases the correlations to the measurements. Maps of GRACE-derived RMS monthly variability indicate a reduction of the land leakage effects close to the coasts when the pattern filter is used. The structures of the oceanic currents are more clearly visible.

The third method used to reduce errors in the GRACE solutions is the de-stripping developed by Swenson and Wahr (2006) and specialised for using GRACE data for oceanic purposes by Chambers (2006). This filtering mechanism is based on correlated errors in the spherical harmonics. The errors due to aliasing manifested as elongated north-south pattern are found to be correlated for higher degree and order spherical harmonics. Subtraction of a polynomial fit representing the error reduces the noise in the data.

This empirical approach can lead to an attenuation of signals. However, a comparison of the de-striped data sets, which are available at different spatial resolution (the data sets are additionally filtered with a 300 km, 500 km, or 750 km Gaussian filter) based on data from the three processing centers GFZ, CSR, and JPL with the *in-situ* data, shows high correlations of mostly larger than 0.5 significant at a 95 % level. A combination of the highest resolution de-striped data set (300 km Gauss) and the pattern filter leads to even higher correlations.

The validation against *in-situ* data quantifies the ability of GRACE to capture ocean bottom pressure variability. The GRACE data shows high agreement with the measurements especially at high latitudes. At low latitudes where the signal to noise ratio is low this connection weakens. However, most of the low latitude measurements are situated in the tropical Atlantic where the GRACE measurements were found to suffer from an additional

issue. GRACE signals are dominated by a large annual cycle which is absent in the *in-situ* data. Although the bottom pressure recorder array is approximately 1000 km away from the Amazon and Orinoco basin, this signal could be induced by land hydrology.

On a basin-scale this deficiency in the GRACE data dominates the OBP average in the Atlantic sector of the ocean. A comparison to results from FESOM simulations shows that GRACE-derived OBP anomalies feature a different phase and a much larger amplitude than the model. As we saw from the model validation against *in-situ* data, FESOM gives a more realistic representation of the *in-situ* anomalies, at least of the annual cycle. Therefore, we conclude that the basin-wide average of the GRACE data suffers from the errors in the Tropics and does not capture the oceanic variability in the Atlantic.

In most of the other ocean basins FESOM and GRACE agree well in phase and amplitude. Signals averaged over the Arctic ocean however feature differences between simulations and GRACE. The GRACE products show large amplitudes and high month-to-month variability which is not captured by the ocean model. This difference may be due to signals induced by effects not represented in the model, like the fluctuations of the Greenland ice mass budget, which influence the GRACE data in this region. Parts of the signals in the GRACE solutions in this region can likely be attributed to land leakage, however a larger part is probably due to real oceanic mass variability since OBP anomalies derived from GRACE are highly correlated to *in-situ* data in the Arctic.

Intercomparison of the data products provided by the three processing centers indicates that the CSR and GFZ solutions feature very similar OBP variations whereas the JPL solutions differs from both in some regions. In the tropical Atlantic for example the anomalies derived from the JPL product show a large annual cycle which is less pronounced in the CSR and GFZ products. Differences also occur in the Arctic where the JPL solution correlates less than the CSR and GFZ solution to the *in-situ* data. In general, the regional comparison indicates that the CSR Release 04 shows highest correlation to the *in-situ* measurements in most regions, followed by the GFZ solution with similar correlations.

In order to assess the ability of GRACE to capture oceanic mass variability induced by atmospheric forcing, this study also comprises an investigation of the volume transport of the Antarctic Circumpolar Current (ACC) and its relation to atmospheric variability as induced by the Southern Annular Mode (SAM). For this purpose we evaluated oceanic transport variations from the ocean model FESOM, and the related variability derived from *in-situ* measurements and compared the results to GRACE derived variations.

The total transport of the ACC through Drake Passage simulated by the ocean model FESOM was found to agree with previous findings based on current measurements within the estimated error bounds (FESOM: 127 Sv, Cunningham et al. (2003): 134 Sv with an error of 15 to 27 Sv). A comparison of the Drake Passage transport to the transport through a section south of Africa given by a BPR array covering the main branches of the ACC shows that the total model transport through this section is lower than in Drake Passage, which can be explained by the fact the model ACC spreads more north- and southward than in reality.

We used the de-tided OBP measurements in the AWI ACC array to determine the ACC variability in the region south of Africa. For the observation period a standard deviation of about 11.5 Sv for the flow across the BPR array was observed. GRACE data derived from the data products from the three processing centers show transport fluctuations with a similar variability (GFZ: 9.8 Sv, CSR: 11.4 Sv, JPL: 11.0 Sv). The FESOM model underestimates the amplitude of the variations with a variability of about 4.9 Sv. However, both FESOM and GRACE show correlations (around 0.6-0.7 at a 95 % significance level) to the observations which indicates that the month-to-month fluctuations are well captured.

Furthermore, an investigation on the influence of the Southern Annular Mode (SAM) on the Southern Ocean circulation has been performed (see also Böning et al. (2009)). Data from FESOM simulations and GRACE gravity field solutions have been analysed for the representation of atmospheric fluctuations in ocean bottom pressure and model transport. Previous theoretical and measurement based studies have indicated a connection between anomalies in SAM index and in ACC transport. This relation is restricted to relatively short time scales of about 10-220 days, because SAM is primarily connected to barotropic fluctuations in the flow. On longer time scales, where baroclinicity dominates the oceanic variability of the ACC, the relation between SAM and transport weakens.

In this study, this relation was quantified by a comparison of the SAM index to model transport, and FESOM and GRACE-derived OBP anomalies. A connection on time scales up to annual could be confirmed. Approximately 30 % of the transport variance could be explained by the atmospheric fluctuations induced by SAM. Spatially, the relation of SAM and OBP is found to be connected to barotropic fluctuations of the flow around Antarctica. Correlations between SAM and FESOM/GRACE OBP show a spatial structure following f/H contours. An EOF analysis of the de-stripped GRACE solutions indicates that this mode is dominant in GRACE-derived OBP. However, a second result of this analysis is that the de-stripped GRACE solutions at high resolution (i.e. after filtering with a 300 km or 500 km Gaussian) is

still contaminated with striping artefacts, whereas the barotropic mode is dominant only in the 750 km and pattern filtered de-striped products.

Outlook

The presented study constitutes a basis for a future evaluation of oceanic mass variability from the three kinds of OBP data: *in-situ*, GRACE-derived and simulated OBP. We evaluated the temporal and spatial behavior of OBP fluctuations provided by the different data sources.

The modification of the model implementation as presented here yields a more realistic approach of the ocean mass budget. Future studies on changes of the ocean mass can utilize this approach to simulate for example the influence of an increased water flux into the ocean. This comprises investigations on the current sea level change due to ice sheet melting. Ongoing studies like the investigation of "Fingerprints of ice melting in geodetic GRACE and ocean models" (FIGO), a project in the framework of the DFG Schwerpunktprogramm "Massentransporte und Massenverteilungen im System Erde", are dealing with effects of ice sheet melting on the sea level. Considering the estimated inflow due to melting by using the forcing adjustment presented in this study is essential to simulate the local and global effects on the sea surface height.

In future studies, a grid refinement will be an important step to obtain an even more realistic representation of oceanic currents. The Finite Element method provides the possibility for definition of a spatially specified grid refinement. This allows for a representation of the global ocean circulation with resolved small scale features like narrow straits, steep continental slopes, or islands.

The assessment of the ability of GRACE to measure oceanic variability gives an insight in the capabilities and deficiencies in these unprecedented data sets. The striping artifacts in the current GRACE solutions are the major issue when using the data for oceanic research. Upcoming GRACE solutions based on regional estimates, like the JPL mascon (mass concentration) solutions or the localizing approach of the ITG Bonn, yield promising first results in this respect. The new products should be less affected by aliasing and therefore are likely to give an even better representation of the mass distributions measured by GRACE. Complementary measurements from satellite missions, e.g. QuikSCAT wind measurements, JASON or TOPEX/POSEIDON altimetry, can be used to further investigate the different contributions to the ocean circulation.

The evaluation indicates that GRACE captures ocean bottom pressure

well especially in the high latitude BPR arrays, whereas some issues were found in the data sets in the tropical Atlantic. In order to improve the existing GRACE products from the processing centers, those spurious signals have to be further investigated and, if possible, to be removed. Studies concerning the connection between the unrealistic annual cycle in the tropical Atlantic and land hydrology (or tidal aliasing) can help to understand this anomalous signal. An approved relationship between land hydrology and the unrealistic oceanic signals measured by GRACE could be used to extract real oceanic variability by removing the estimated hydrological cycle from the GRACE data over the ocean in this region.

Semi-diurnal and diurnal tides play an important role in the GRACE de-aliasing. As pointed out by Ray et al. (2003), errors in K_1 , K_2 , S_1 , S_2 , and P_1 constituents alias to periods of 7.48 years, 3.74 years, 322 days, 161 days, and 171 days, respectively. Given that tides at short time scales can be estimated more precisely by ocean bottom pressure measurements as shown in chapter 4, the information on tides provided by the global *in-situ* data base can be used to complement and improve tide models. This improvement would also yield an improvement of the GRACE solutions due to a better accuracy of the background models.

Extension of the global data base would provide the possibility to supplement this GRACE validation study. *In-situ* OBP observations in regions not yet covered by the currently available data sets may be used to obtain valuable information on the ability of GRACE to capture oceanic variability in these parts of the global ocean. Longer time series of *in-situ* and GRACE data would allow for a more detailed analysis of the data. A spectral analysis for example, which is barely feasible with time series comprising only a few data points, would yield further information on phenomena on different time scales.

Important for the future evaluation of trends in the sea level utilizing gravity field observations will be a validation against trends in *in-situ* ocean bottom pressure. Although, today's pressure measurements are already highly accurate in determination of subannual variability, long-term trends can hardly be provided, since the adjustment of the pressure sensors to the ambient pressure induces a sensor-dependent trend which is difficult to evaluate. Overcoming this issue would yield a valuable step in the direction of a future validation of sea level trends.

In general, future gravity missions, like a GRACE-follow-on mission or the planned GRACE-II mission (to be launched in 2018), can benefit from the results from this study: deficiencies in the gravity field solutions have been localized and possible error sources identified. This information yields a base for improvements in the future gravity field processing.

Appendix A

The *in-situ* OBP data base

Site-ID	Latitude	Longitude	Start	End	Institution	Project/Contact
ANT5-1	41° 8.04' S	9° 56.63' E	27-Jan-05	12-Feb-08	AWI	GRACE/O. Boebel
ANT7-1	44° 39.75' S	7° 5.03' E	28-Nov-02	27-Jan-05	AWI	GRACE/O. Boebel
ANT7-2	44° 39.84' S	7° 4.93' E	28-Jan-05	15-Feb-08	AWI	GRACE/O. Boebel
ANT9-1	47° 39.36' S	4° 15.70' E	30-Jan-05	17-Feb-08	AWI	GRACE/O. Boebel
ANT11-1	50° 15.01' S	1° 25.00' E	30-Nov-02	30-Jan-05	AWI	GRACE/O. Boebel
ANT11-2	50° 15.73' S	1° 25.95' E	26-Oct-06	22-Apr-07	AWI	GRACE/O. Boebel
ANT13-1	52° 30.42' S	1° 24.04' W	24-Oct-06	20-Feb-08	AWI	GRACE/O. Boebel
F2_2004	78° 50.03' N	8° 19.91' E	2-Sep-04	15-Aug-05	AWI	Framstrait/A. Beszcynska-Mller
F2_2005	78° 50.36' N	8° 19.63' E	17-Aug-05	16-Aug-06	AWI	Framstrait/A. Beszcynska-Mller
F6_2003	78° 49.93' N	5° 0.87' E	27-Sep-03	21-Jul-04	AWI	Framstrait/A. Beszcynska-Mller
F6_2004	78° 49.87' N	5° 0.93' E	2-Sep-04	16-Aug-05	AWI	Framstrait/A. Beszcynska-Mller
F6_2005	78° 50.04' N	4° 54.70' E	26-Aug-05	16-Aug-06	AWI	Framstrait/A. Beszcynska-Mller
F8_2003	78° 49.87' N	2° 47.59' E	28-Sep-03	20-Jul-04	AWI	Framstrait/A. Beszcynska-Mller
F8_2004	78° 50.25' N	2° 48.20' E	2-Sep-04	3-Aug-05	AWI	Framstrait/A. Beszcynska-Mller
F8_2005	78° 49.96' N	2° 50.87' E	31-Aug-05	16-Aug-06	AWI	Framstrait/A. Beszcynska-Mller
AMS-03	37° 54.20' S	77° 34.80' E	15-Jan-03	22-Dec-03	CNES	L. Testut
AMS-04	37° 53.90' S	77° 33.40' E	22-Dec-03	22-Dec-04	CNES	L. Testut
CRO-02	46° 33.10' S	51° 47.20' E	23-Jan-02	09-Dec-03	CNES	L. Testut
CRO-04	46° 32.80' S	51° 47.30' E	10-Dec-03	10-Dec-04	CNES	L. Testut
v404_3	15° 27.00' N	51° 31.50' W	4-Feb-02	19-Jun-03	IFM- GEOMAR	MOVE/J. Karstensen
v404_4	15° 27.00' N	51° 31.50' W	22-Jun-03	19-Feb-04	IFM- GEOMAR	MOVE/J. Karstensen
M1	15° 27.01' N	51° 31.59' W	23-Feb-04	3-Jul-04	IFM- GEOMAR	MOVE/J. Karstensen
M1	15° 27.01' N	51° 31.59' W	3-Jul-04	17-Mar-06	IFM- GEOMAR	MOVE/J. Karstensen
M1.5	15° 43.10' N	54° 13.50' W	25-Feb-04	13-Dec-06	IFM- GEOMAR	MOVE/J. Karstensen
M2	15° 59.20' N	56° 57.00' W	17-Feb-04	5-Jul-04	IFM- GEOMAR	MOVE/J. Karstensen
M2	15° 59.20' N	56° 57.00' W	26-Jul-04	12-Oct-06	IFM- GEOMAR	MOVE/J. Karstensen
M2.5	16° 10.00' N	58° 43.00' W	25-Jul-04	23-Apr-06	IFM- GEOMAR	MOVE/J. Karstensen
M3	16° 21.30' N	60° 29.27' W	21-Feb-04	4-Jul-04	IFM- GEOMAR	MOVE/J. Karstensen
M3	16° 21.30' N	60° 29.27' W	7-Jul-04	17-Feb-06	IFM- GEOMAR	MOVE/J. Karstensen
M6	20° 35.51' N	56° 40.78' W	26-Feb-04	20-Nov-05	IFM- GEOMAR	MOVE/J. Karstensen

46402	51° 4.14' N	164° 0.60' W	1-Jan-03	31-Dec-03	NOAA	DART/C. Meinig
46402	51° 4.14' N	164° 0.60' W	1-Jan-04	30-Nov-04	NOAA	DART/C. Meinig
46402	51° 4.14' N	164° 0.60' W	01-May-05	31-Dec-05	NOAA	DART/C. Meinig
46403	52° 39.00' N	156° 56.40' W	1-Jan-03	31-Dec-03	NOAA	DART/C. Meinig
46403	52° 39.00' N	156° 56.40' W	1-Jan-04	31-Dec-04	NOAA	DART/C. Meinig
46403	52° 39.00' N	156° 56.40' W	1-Jan-05	31-Dec-05	NOAA	DART/C. Meinig
46404	45° 51.54' N	128° 46.68' W	11-Jan-03	22-Oct-03	NOAA	DART/C. Meinig
46404	45° 51.54' N	128° 46.68' W	16-Jan-05	5-Nov-05	NOAA	DART/C. Meinig
46405	42° 54.18' N	130° 54.54' W	1-Jan-03	31-Dec-03	NOAA	DART/C. Meinig
46405	42° 54.18' N	130° 54.54' W	1-Jan-04	31-Dec-04	NOAA	DART/C. Meinig
46405	42° 54.18' N	130° 54.54' W	1-Jan-05	31-Dec-05	NOAA	DART/C. Meinig
46409	55° 18.00' N	148° 30.00' W	28-Sep-05	31-Dec-05	NOAA	DART/C. Meinig
46411	39° 20.40' N	127° 0.42' W	27-Sep-05	31-Dec-05	NOAA	DART/C. Meinig
46412	32° 14.76' N	120° 41.88' W	29-Sep-05	31-Dec-05	NOAA	DART/C. Meinig
51407	19° 38.04' N	156° 30.42' W	28-Jun-05	31-Dec-05	NOAA	DART/C. Meinig
d125_2002	8° 29.32' S	125° 0.84' W	15-Jan-02	27-Jan-03	NOAA	DART/C. Meinig
d125_2003	8° 29.22' S	125° 1.07' W	29-Jan-03	11-May-04	NOAA	DART/C. Meinig
d157_2002	52° 39.02' N	156° 56.43' W	16-Jun-02	31-May-03	NOAA	DART/C. Meinig
d157_2003	52° 39.02' N	156° 56.43' W	01-May-03	04-May-04	NOAA	DART/C. Meinig
d171_2002	46° 38.21' N	170° 47.86' W	21-Jun-02	30-Jun-03	NOAA	DART/C. Meinig
d171_2003	42° 38.21' N	170° 47.86' W	01-May-03	07-May-04	NOAA	DART/C. Meinig
IO1	47° 7.00' S	54° 54.05' E	23-Jan-04	17-Feb-05	POL	ACCLAIM /C. Hughes
IO2	48° 49.90' S	61° 16.78' E	24-Jan-04	31-Jan-05	POL	ACCLAIM /C. Hughes
ND2	54° 56.59' S	58° 21.41' W	31-Oct-03	03-Dec-04	POL	ACCLAIM /C. Hughes
ND2	54° 56.59' S	58° 21.41' W	18-Dec-04	07-Dec-05	POL	ACCLAIM /C. Hughes
SD2	60° 51.03' S	54° 42.80' W	28-Nov-00	15-Nov-02	POL	ACCLAIM /C. Hughes
SD2	60° 51.00' S	54° 42.77' W	27-Dec-02	07-Dec-04	POL	ACCLAIM /C. Hughes
SD2	60° 51.03' S	54° 42.80' W	07-Dec-04	11-Dec-05	POL	ACCLAIM /C. Hughes
GRACE-2	44° 25.20' S	40° 22.19' W	16-May-02	16-May-03	POL	ACCLAIM /C. Hughes
GRACE-3	43° 11.90' S	45° 18.10' W	17-May-02	17-May-03	POL	ACCLAIM /C. Hughes
MOVE-A	16° 20.85' N	60° 29.78' W	24-Jan-02	26-Jun-03	POL	ACCLAIM /C. Hughes
MOVE-B	16° 22.29' N	60° 30.32' W	29-Jun-03	01-Mar-04	POL	ACCLAIM /C. Hughes
MYRTLE	60° 2.98' S	47° 10.20' W	26-Oct-99	3-Nov-03	POL	ACCLAIM /C. Hughes
SHAGEX1	53° 4.86' S	47° 6.12' W	05-May-03	17-Nov-04	POL	ACCLAIM /C. Hughes
SHAGEX2	53° 23.21' S	49° 31.82' W	08-May-03	28-Nov-04	POL	ACCLAIM /C. Hughes

Table A.1: Listing of BPR deployments.

Appendix B

Auxiliary material for FESOM validation

In the AWI ACC array, the observed variability features large signals at northern locations, especially for long periodic signals with periods longer than 30 days (Fig. B.1). The variability decreases in the OBP signals observed at southern locations. The FESOM model reproduces mainly the low variability in the South, whereas the high variability in the North is not well captured. On short time scales, shorter than 4 days, the model shows a low variability compared to the PIES OBP anomalies.

Coherence between the model and the observations significantly increases from North to South (Fig. B.2). Phases are similar for time series at ANT-7 and southward.

In the MOVE array a similar range of variability is found in the *in-situ* and FESOM OBP anomalies (Fig. B.3). The spectral density of the time series at all 6 positions is at a low level and similar for all frequencies. The FESOM model slightly underestimates the variability.

A good agreement between observations and simulated OBP can be detected for periods from 3-10 days (Fig. B.4). For periods up to 100 days and shorter than 3 days the coherence between FESOM and the PIES measurements weakens.

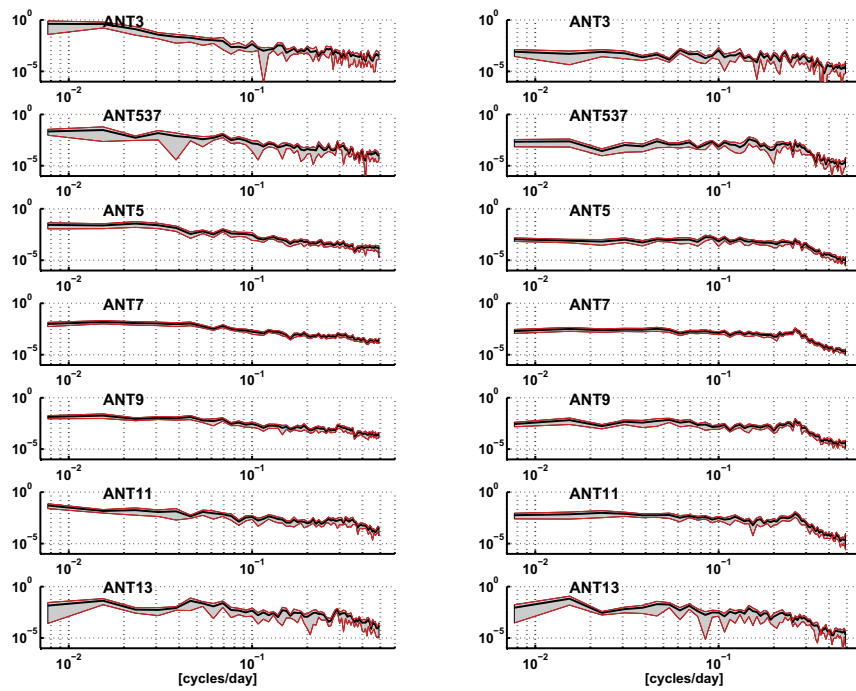


Figure B.1: Spectral density in the AWI ACC array derived from *in-situ* (left) and FESOM (right) OBP anomalies.

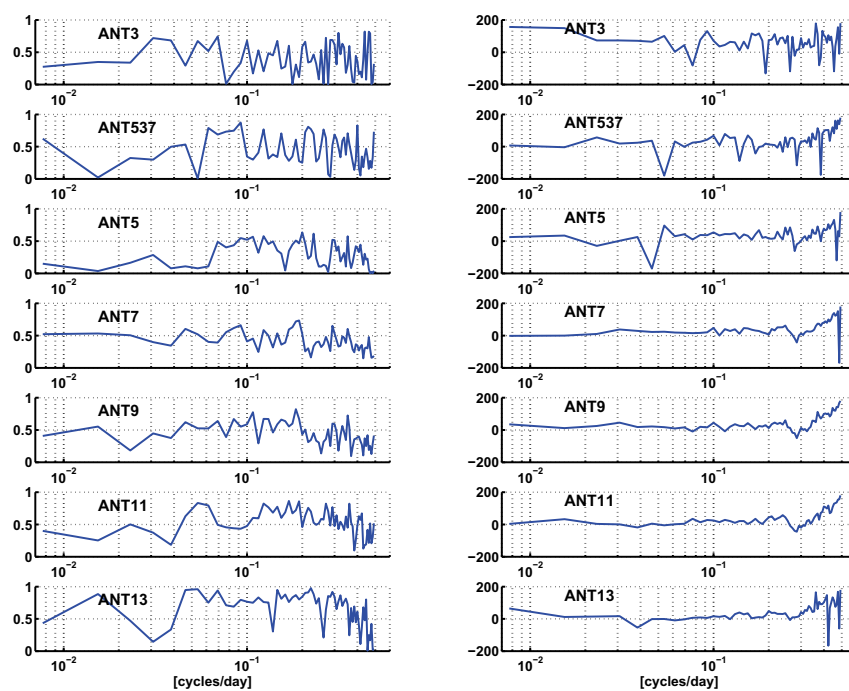


Figure B.2: Coherence (left) and phase (right) between observations and model in the AWI ACC array.

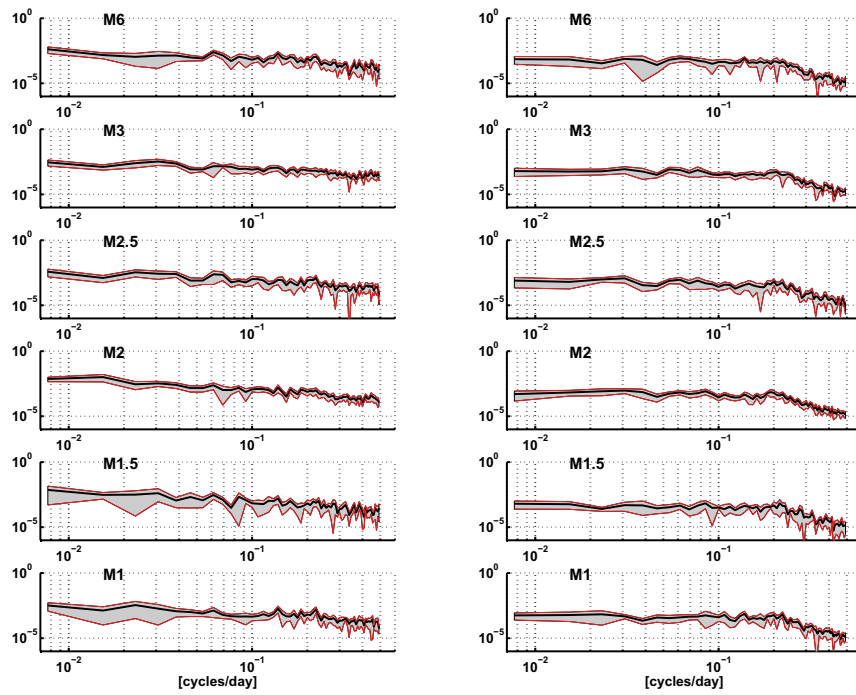


Figure B.3: Spectral density in the MOVE array derived from *in-situ* (left) and FESOM (right) OBP anomalies.

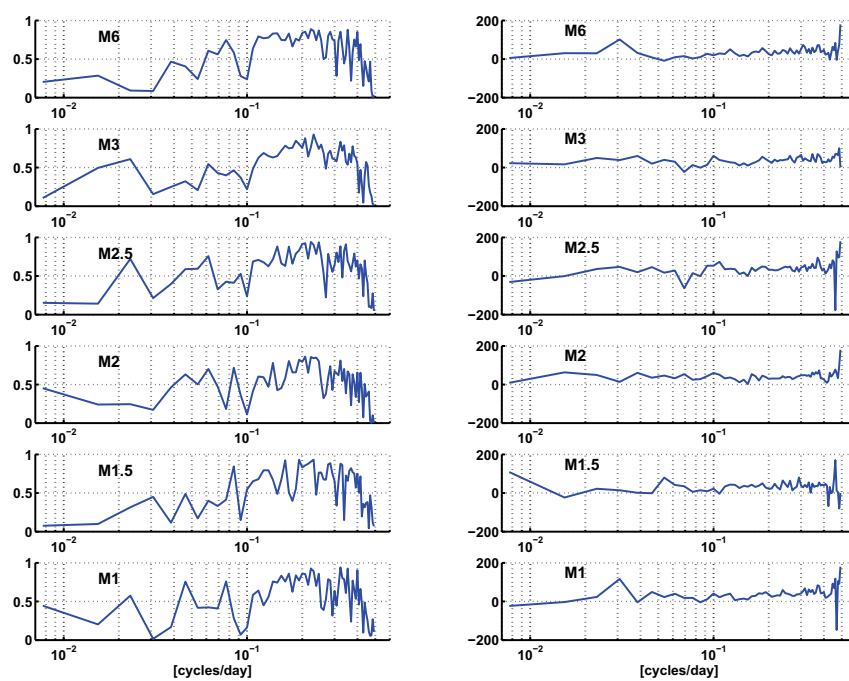


Figure B.4: Coherence (left) and phase (right) between observations and model in the MOVE array.

List of Acronyms

ACC	Antarctic Circumpolar Current
ACCLAIM	Antarctic Circumpolar Current Levels by Altimetry and Island Measurements
BPR	Bottom Pressure Recorder
CNES	Centre National d'Etudes Spatiales
CSR	Center for Space Research
DART	Deep-ocean Assessment and Reporting of Tsunamis
DORIS	Doppler Orbitography and Radiopositioning Integrated by Satellite
ECCO	Estimating the Circulation and Climate of the Ocean
ECMWF	European Centre for Medium Range Weather Forecasts
ERS	European Remote Sensing satellite
FEOM	Finite Element Ocean Modell
FES	Finite Element Solution
FESOM	Finite Element Sea Ice–Ocean Modell
GFZ	GeoForschungsZentrum Potsdam
GPS	Global Positioning System
GRACE	Gravity Recovery And Climate Experiment
HDM	Hydrological Discharge Model
JPL	Jet Propulsion Laboratory

LAGEOS	Laser Geodynamics Satellite
LEO	Low Earth Orbit
MOC	Meridional Overturning Circulation
MOVE	Meridional Overturning Variability Experiment
NCAR	National Center for Atmospheric Research
NCEP	National Centers for Environmental Prediction
OBP	Ocean Bottom Pressure
OCCAM	Ocean Circulation and Climate Advanced Modelling Project
OGCM	Ocean General Circulation Model
PIES	Pressure sensor equipped Inverted Echo Sounder
POCM	Parallel Ocean Climate Model
POL	Proudman Oceanographic Laboratory
QuikSCAT	Quick Scatterometer
SLP	Sea Level Pressure
SLR	Satellite Laser Ranging
WECCON	Weddell Sea Convection Control

List of Figures

3.1	Time series of globally averaged fresh water flux.	32
3.2	Time series of global mean ocean mass anomalies without flux correction.	32
3.3	Time series of adjusted sum of runoff and net precipitation. . .	33
3.4	Time series of global mean ocean mass anomalies with flux correction.	34
4.1	Positions of the BPRs.	36
4.2	Time series of <i>in-situ</i> OBP at 47° S, 4° E.	37
4.3	Time series of <i>in-situ</i> OBP at 47° S, 4° E.	38
4.4	Map of locations of the BPRs.	42
4.5	Power spectrum of OBP measurements (left panel) and FES2004 tides (right panel).	43
4.6	Amplitude of the M2/S2 tide derived from FES2004.	44
4.7	Amplitude of the K1/O1 tide derived from FES2004.	44
4.8	Lagged correlation of empirically determined and simulated tide at PIES position ANT-7.	45
4.9	Power spectrum of the corrected time series.	47
4.10	Modeled and empirically determined tidal variability.	48
4.11	Variance of monthly mean OBP anomalies derived from FESOM simulations. Contour lines indicate f/H contours.	49
4.12	Variance of FESOM OBP in the AWI ACC array.	50
4.13	OBP variability derived from FESOM and <i>in-situ</i> data	51
4.14	OBP variability derived from FESOM and <i>in-situ</i> data	52
4.15	Variance of FESOM OBP in the MOVE array.	53
4.18	Correlation between FESOM OBP anomalies and <i>in-situ</i> data on a monthly time scale. Large circles indicate a correlation at a significance level of 95 %	54
4.16	OBP variability derived from FESOM and <i>in-situ</i> data	55
4.17	OBP variability derived from FESOM and <i>in-situ</i> data	56

4.19	Ratio of standard deviation of FESOM OBP anomalies and <i>in-situ</i> data on a monthly time scale.	57
5.1	Typical GRACE-derived monthly OBP anomaly.	65
5.2	RMS monthly variability of OBP derived from a GRACE solution filtered with a 750 km Gauss filter (GFZ RL04, GSM+GAD, d/o 1-50).	66
5.3	Two examples of model-derived patterns of high spatial coherency ("coherence patterns").	68
5.4	Time series of OBP anomalies at $77.58^{\circ}E$, $37.9^{\circ}S$ (CNES, Amsterdam Island) and $164^{\circ}W$, $51.07^{\circ}N$ (NOAA DART Array).	70
5.5	Correlations between <i>in-situ</i> and GRACE-derived OBP anomalies.	70
5.6	RMS monthly variability of GRACE GFZ RL04.	71
5.7	Global mean OBP anomalies derived from GFZ RL04 solutions with a 750 km Gauss filter and the coherence-pattern filter.	72
5.8	Correlation between <i>in-situ</i> OBP and de-stripped GRACE solutions.	74
5.9	Standard deviation of <i>in-situ</i> OBP compared to de-stripped GRACE OBP anomalies.	75
5.10	Correlation between <i>in-situ</i> and de-stripped/pattern-filtered GRACE solutions.	77
5.11	Standard deviation of <i>in-situ</i> compared to de-stripped, pattern-filtered GRACE OBP anomalies.	78
5.12	Positions of the BPRs and definition of arrays.	79
5.13	Map of subdivision of the global ocean into basins.	81
5.14	Basin-averaged time series of OBP anomalies.	82
5.15	Time series of OBP anomalies in the MOVE array (tropical Atlantic)	83
5.16	Variance of OBP anomalies derived from the de-stripped GRACE solutions and FESOM simulations.	84
6.1	Bathymetry of the Southern Ocean.	88
6.2	Map of PIES positions in the AWI ACC array.	91
6.3	Simulated transport through Drake Passage derived from a 10 yr FESOM simulation with a 40 yr spin-up.	92
6.4	Simulated transport through section defined by ACC PIES array.	93
6.5	Southern Ocean stream function derived from FESOM simulation.	93

6.6	Transport through section south of Africa covering the entire model ACC.	94
6.7	Correlation between OBP gradients derived from GRACE, FESOM and <i>in-situ</i> OBP.	95
6.8	Transport variations derived from GRACE, FESOM and <i>in-situ</i> OBP.	96
6.9	Correlation for 2002-2007 between SLP derived from NCEP/N-CAR reanalysis and the SAM index of Marshall (2003).	97
6.10	SAM index and GRACE OBP anomalies.	99
6.11	Monthly changes of SAM index (black) and FESOM volume transport anomalies through Drake Passage (red).	100
6.12	Correlation between the SAM index and FESOM OBP anomalies.	101
6.13	Correlation between the SAM index and GRACE-derived OBP anomalies.	102
6.14	First EOF of GRACE-derived OBP anomalies in the Southern Ocean.	103
B.1	Spectral density in the AWI ACC array.	118
B.2	Coherence and phase between observations and model in the AWI ACC array.	119
B.3	Spectral density in the MOVE array.	120
B.4	Coherence and phase between observations and model in the MOVE array.	121

List of Tables

4.1	Fundamental Tidal Frequencies	39
4.2	Equilibrium amplitude and period of the main tidal constituents.	39
5.1	Abbreviations for GRACE products.	62
5.2	Amplitude (in mm) and phase (day of maximum signal) of the estimated annual geocenter motion based on Cretaux et al. (2002).	64
5.3	Skill calculated for the BPR arrays.	80
A.1	Listing of BPR deployments.	116

Bibliography

- Belkin, I., Gordon, A. (1996). Southern Ocean fronts from the Greenwich meridian to Tasmania. *J. Geophys. Res.* **101(C2)**, 3675–3696.
- Boebel, O., Rossby, T., Lutjeharms, J., Zenk, W., Barron, C. (2003). Path and variability of the Agulhas Return Current. *DEEP-SEA RESEARCH PART II-TOPICAL STUDIES IN OCEANOGRAPHY* **50(1)**, 35–56.
- Böning, C., Timmermann, R., Danilov, S., Schröter, J. (2009). *On the representation of transport variability of the Antarctic Circumpolar Current in GRACE gravity solutions and numerical ocean model simulations.*
- Böning, C., Timmermann, R., Macrander, A., Schröter, J. (2008). A pattern-filtering method for the determination of ocean bottom pressure anomalies from GRACE solutions. *Geophys. Res. Lett.* **35**, L18611.
- Chambers, D. (2006). Evaluation of new GRACE time-variable gravity data over the ocean. *Geophys. Res. Lett.* **33**, L17603.
- Chen, J. L., Wilson, C. R., Tapley, B. D., Chambers, D. P., Pekker, T. (2001). Hydrological impacts on seasonal sea level change. *Global and Planetary Change* **32(1)**, 25 – 32.
URL: <http://www.sciencedirect.com/science/article/B6VF0-448RDMF-1/2/f6d6bef953c1cd0e80ba2392e295c26a>
- Connolley, W., Gregory, J., Hunke, E., McLaren, A. (2004). On the consistent scaling of terms in the sea-ice dynamics equation. *J. Phys. Ocean.* **34 (7)**, 17761780.
- Cretaux, J.-F., Soudarin, L., Davidson, F. J. M., Gennero, M.-C., Berge-Nguyen, M., Cazenave, A. (2002). Seasonal and interannual geocenter motion from SLR and DORIS measurements: Comparison with surface loading data. *J. Geophys. Res.* **107((B12))**, 2374.

- Cunningham, S. A., Alderson, S. G., King, B. A., Brandon, M. A. (2003). Transport and variability of the Antarctic Circumpolar Current in Drake Passage. *J. Geophys. Res.* **108**, 8084.
- Cunningham, S. A., Pavic, M. (2007). Surface geostrophic currents across the Antarctic circumpolar current in Drake Passage from 1992 to 2004. *Progress in Oceanography* **73**, 296–310.
- Danilov, S., Kivman, G., Schröter, J. (2004). A finite element ocean model: principles and evaluation. *Ocean Modelling* **6**, 125–150.
- Danilov, S., Yakovlev, N. (2003). A Finite Element Ice Model.
- Doodson, A. T. (1922). Harmonic development of the tide-generating potential. *Proceedings of the Royal Society of London A* **100**, 305329.
- Douglas, B. C., Peltier, W. R. (2002). The puzzle of global sea-level rise. *Phys. Today* **55(3)**, 3540.
- Eicken, H., Lange, M., Hubberten, H., Wadhams, P. (1994). Characteristics and distribution patterns of snow and meteoric ice in the Weddel Sea and their contribution to the mass-balance of sea-ice. *Annales Geophysicae-Atmospheres Hydrospheres and Space Sciences* **12(1)**, 80–93.
- Fischer, H. (1995). Vergleichende Untersuchungen eines optimierten dynamisch-thermodynamischen Meereismodells mit Beobachtungen im Weddellmeer. *Berichte zur Polarforschung, Alfred-Wegener-Institut (AWI), Bremerhaven* **166**.
- Frappart, F., Ramillien, G., Biancamaria, S., Mognard, N. M., Cazenave, A. (2006). Evolution of highlatitude snow mass derived from the GRACE gravimetry mission (20022004). *Geophys. Res. Lett.* **33**, L02501.
- Gent, P., McWilliams, J. (1990). Isopycnal mixing in ocean circulation models. *J. Phys. Ocean.* **20**, 150155.
- Gent, P., Willebrand, J., McDougall, T., McWilliams, J. (1995). Parameterizing eddy-induced tracer transports in ocean circulation models. *J. Phys. Ocean.* **25 (6)**, 1365.
- Greatbatch, R. (1994). A note on the representation of steric sea level in models that conserve volume rather than mass. *J. Geophys. Res.* **99**, 767–771.

- Griffies, S. (2004). *Fundamentals of Ocean Climate Models*. Princeton University Press, Princeton, USA.
- Hibler III, W. (1979). A dynamic thermodynamic sea ice model. *J. Phys. Ocean.* **9**(4), 815–846.
- Hughes, C., Meredith, M., Heywood, K. J. (1999). Wind-Driven Transport Fluctuations through Drake Passage: A Southern Mode. *J. Phys. Oceanogr.* **29**, 1971–1992.
- Hughes, C., Woodworth, P., Meredith, M., Stepanov, V., Whitworth, T., Pyne, A. (2003). Coherence of Antarctic sea levels, Southern Hemisphere Annular Mode, and flow through Drake Passage. *Geophys. Res. Lett.* **30**(9), 1464.
- Hunke, E., Dukowicz, J. (1997). An elastic-viscous-plastic model for sea ice dynamics. *J. Phys. Ocean.* **27**, 1849–1868.
- Hunke, E., Lipscomb, W. (2001). CICE: The Los Alamos Sea Ice Model, Documentation and Software Users Manual. *LACC-98-16 v.3. Los Alamos National Laboratory, Los Alamos, USA* .
- IPCC (2007). Climate Change 2007: The Physical Science Basis. Contribution of Working Group I to the Fourth Assessment Report of the Intergovernmental Panel on Climate Change. *Cambridge University Press, Cambridge, United Kingdom and New York, NY, USA*, .
- Jackett, D. R., McDougall, T. J. (1995). Stabilization of hydrographic data. *J. Atmos. Oceanic Technol.* **12**, 381–389.
- Kalnay, E., Kanamitsu, M., Kistler, R., Collins, W., Deaven, D., Gandin, L., Iredell, M., Saha, S., White, G., Woollen, J., Zhu, Y., Chelliah, M., Ebisuzaki, W., Higgins, W., Janowiak, J., Mo, K., Ropelewski, C., Wang, J., Leetmaa, A., Reynolds, R., Jenne, R., Joseph, D. (1996). The NCEP/NCAR 40-year reanalysis project. *Bulletin of the American Meteorological Society* **77**, 437–471.
- Kanzow, T., Flechtner, F., Chave, A., Schmidt, R., Schwintzer, P., Send, U. (2005). Seasonal variation of ocean bottom pressure derived from Gravity Recovery and Climate Experiment (GRACE): Local validation and global patterns. *J. Geophys. Res.* **110**(C09001).
- Kennelly, M., Tracey, K., Watts, D. (2007). Inverted Echo Sounder Data Processing Manual. Technical Report GSO Technical Report No. 2007-

- 02, Graduate School of Oceanography, University of Rhode Island, Narragansett, Rhode Island.
- König-Langlo, G., Augstein, E. (1994). Parameterization of the downward long-wave radiation at the Earths surface in polar regions. *Meteorologische Zeitschrift* **3** .
- Laevastu, T. (1960). Factors affecting the temperature of the surface layer of the sea. *Commentationes Physico-Mathematicae* **25** (1).
- Lefebvre, W., Goosse, H., Timmermann, R., Fichefet, T. (2004). Influence of the Southern Annular Mode on the sea iceocean system. *J. Geophys. Res.* **109**, C09005.
- Leppäranta, M. (1983). A growth model for black ice, snow ice, and snow thickness in subarctic basins. *Nordic Hydrology* **14**, 5970.
- Lettmann, K., Olbers, D. (2005). Investigation of ACC transport and variability through Drake Passage using the simple ocean model BARBI. *CLIVAR Exchanges* **10**(4), 30–32.
- Lombard, A., Garcia, D., Ramillien, G., Cazenave, A., Biancale, R., Lemoine, J., Flechtner, F., Schmidt, R., Ishii, M. (2007). Estimation of steric sea level variations from combined GRACE and Jason-1 data. *Earth and Planetary Science Letters* **254**(1-2), 194–202.
- Lyard, F., Lefevre, F., Letellier, T., Francis, O. (2006). Modelling the global ocean tides: modern insights from FES2004. *Ocean Dynamics* **56**, 394–415.
- Macrander, A., Böning, C., Boebel, O., Schröter, J. (2009). *GRACE Validation by in-situ data of Ocean Bottom Pressure*.
- Marshall, G. J. (2003). Trends in the Southern Annular Mode from observations and reanalyses. *J. Clim.* **16**, 4134–4143.
- Meredith, M., Woodworth, P., Hughes, C., Stepanov, V. (2004). Changes in the ocean transport through Drake Passage during the 1980s and 1990s, forced by changes in the Southern Annular Mode. *Geophys. Res. Lett.* **31**.
- Munk, W. H., Cartwright, D. E. (1966). Tidal spectroscopy and prediction. *Phil. Trans. R. Soc.* **259**, 533–81.

- Nooner, S. L., Akhter, S. H., Chowdhury, S., Steckler, M. S., Bettadpur, S. (2008). Modeling Earth Deformation from Monsoonal Flooding in Bangladesh using Hydrographic, GPS and GRACE Data. *AGU Fall Meeting Abstracts* B1958+.
- Olbers, D., Borowski, D., Völker, C., Wolff, J.-O. (2004). The dynamical balance, transport and circulation of the Antarctic Circumpolar Current. *Antarctic science* **16**(4), 439–470.
- Olbers, D., Lettmann, K. (2007). Barotropic and baroclinic processes in the transport variability of the Antarctic Circumpolar Current. *Ocean Dynamics* **57**(6), 559–578.
- ORSI, A., WHITWORTH III, T., NOWLIN, W. (1995). On the meridional extent and fronts of the Antarctic Circumpolar Current. *Deep-Sea Research* **42**, 641673.
- Owens, W., Lemke, P. (1990). Sensitivity studies with a sea ice-mixed layer-pycnocline model in the Weddell Sea. *J. Geophys. Res.* **95** (C6), 95279538.
- Pacanowski, R., Philander, S. (1981). Parameterization of Vertical Mixing in Numerical Models of Tropical Oceans. *J. Phys. Ocean.* **11**, 1443–1451.
- Parkinson, C., Washington, W. (1979). A large-scale numerical model of sea ice. *J. Geophys. Res.* **84** (C1), 311337.
- Ponte, R. M., Quinn, K. J., Wunsch, C., Heimbach, P. (2007). A comparison of model and GRACE estimates of the large-scale seasonal cycle in ocean bottom pressure. *Geophysical Research Letters* **34**, L09603.
- Ramillien, G., Cazenave, A., Brunau, O. (2004). Global time variations of hydrological signals from GRACE satellite gravimetry. *Geophys. J. Int.* **158**, 813–826.
- Ray, R., Rowlands, D., Egbert, G. (2003). Tidal models in a new era of satellite gravimetry. *Space Sci. Res.* **108**, 271–282.
- Redi, M. H. (1982). Oceanic isopycnal mixing by coordinate rotation. *J. Phys. Ocean.* **12**, 11541158.
- Rietbroek, R., LeGrand, P., Wouters, B., Lemoine, J.-M., Ramilien, G., Hughes, C. W. (2006). Comparison of in situ bottom pressure data with GRACE gravimetry in the Crozet-Kerguelen region. *Geophys. Res. Lett.* **33**.

- Schmidt, R., Schwintzer, P., Flechtner, F., Reigber, C., Güntner, A., Döll, P., Ramillien, G., Cazenave, A., Petrovic, S., Jochmann, H., Wunsch, J. (2006). GRACE observations of changes in continental water storage. *Global and Planetary Change* **50**(1-2), 112 – 126.
URL: <http://www.sciencedirect.com/science/article/B6VF0-4JCCCYT-1/2/16f9505ea6b16c537d325423508107cb>
- Semtner Jr., A. (1976). A model for the thermodynamic growth of sea ice in numerical investigations of climate. *J. Phys. Ocean.* **6** (3), 379389.
- Seo, K.-W., Wilson, C. R., Chen, J., Waliser, D. E. (2008). GRACE's spatial aliasing error. *Geophys. J. Int.* **172**, 41–48.
- Swenson, S., Wahr, J. (2006). Post-processing removal of correlated errors in GRACE data. *Geophys. Res. Lett.* **33**, L08402.
- Thompson, D. W. J., Solomon, S. (2002). Interpretation of Recent Southern Hemisphere Climate Change. *Science* **296**, 895–899.
- Timmermann, R., Beckmann, A. (2004). Parameterization of vertical mixing in the Weddell Sea. *Ocean Modelling* **6**(1), 83100.
- Timmermann, R., Beckmann, A., Hellmer, H. (2002). Simulation of ice-ocean dynamics in the Weddell Sea. Part I: model configuration validation. *J. Geophys. Res.* **107** (C3).
- Timmermann, R., Danilov, S., Schröter, J., Böning, C., Sidorenko, D., Rolenhagen, K. (2009). Ocean circulation and sea ice distribution in a finite element global sea ice-ocean model. *Ocean Modelling* **27**, 114–129.
- University of Rhode Island (2006). Inverted Echo Sounder User's Manual .
- Vallis, G. K. (2006). *Atmospheric and Oceanic Fluid Dynamics*. Cambridge University Press, Cambridge, U.K.
- Velicogna, I., Wahr, J. (2006). Measurements of Time-Variable Gravity Show Mass Loss in Antarctica. *Science* **311**(5768), 1754–1756.
URL: <http://www.sciencemag.org/cgi/content/abstract/311/5768/1754>
- Wahr, J., Molenaar, M., Bryan, F. (1998). Time variability of Earth's gravity field: Hydrological and oceanic effects and their possible detection using GRACE. *J. Geophys. Res.* **30**, 205–229.

- Walter, C. (2007). Simulations of hydrological mass variations and their influence on the Earth's rotation .
URL: <http://nbn-resolving.de/urn:nbn:de:bsz:14-ds-1205946097808-36130>
- Zillman, J. (1972). A study of some aspects of the radiation and heat budgets of the southern hemisphere oceans. *Meteorological Study* **26**.
- Zlotnicki, V., Wahr, J., Fukumori, I., Song, Y. T. (2006). Antarctic Circumpolar Current Transport Variability during 2003-05 from GRACE. *J. Phys. Ocean.* **37**, 230–244.

Acknowledgments

This work was written at the Alfred Wegener Institute for Polar and Marine Research and supported by the German Ministry of Education and Research (BMBF) in the framework of the GRACE project within the GEOTECHNOLOGIEN geoscientific R&D programme under grant 03F0423E.

I would like to thank Prof. Dr. Dirk Olbers and Prof. Dr. Peter Lemke, who reviewed this thesis and have always been inspiring examples for me.

My advisor, Dr. Jens Schröter, I thank for giving me the opportunity to start a career as an oceanographer and to attend various national and international conferences and for always supporting me with scientific advice.

I would like to thank Dr. Sergey Danilov and Dr. Olaf Boebel, who always took their time to answer my questions and to discuss any issues regarding ocean modelling or observations.

Big thanks go to Stefan Hendricks for providing his apartment in Bremerhaven during the busiest period of writing and Olaf Klatt for the rides back home to Bremen. Thank you for your friendship and helping me to successfully complete this thesis.

I would like to thank Dr. Eberhard Fahrback for giving me the opportunity to participate in the ANT-XXIV/3 cruise to Antarctica and especially for giving us hope and strength in times of deepest sorrow.

Special thanks go to Dr. Ralph Timmermann who introduced me to the world of physical oceanography and helped me finding my way in climate research. I am very grateful for the huge amount of time you spent supporting me and my work during the last three years. Thank you very much for always believing in me and my capabilities.

All colleagues at AWI I would like to thank for the fruitful scientific discussions and the enjoyable time in a fantastic working atmosphere.

Finally, I would like to thank my family, my brothers, Andre and Clemens, my sister in law, Insa, my neece, Nina, and my parents, Wilhelm and Jenny Böning. Your faith in me and your unconditional support always helped me to accomplish what I began.